Investigation of the Impact and Melting Process of Ice Particles

"Untersuchung des Aufschlags- und Schmelzprozesses von Eispartikeln"

Vom Fachbereich Maschinenbau
an der Technischen Universität Darmstadt
zur
Erlangung des akademischen Grades eines
Doktor-Ingenieurs (Dr.-Ing.)
genehmigte
Dissertation
vorgelegt von
Dipl.-Ing. Tobias Hauk
aus Heidelberg, Deutschland.

Berichterstatter:	Prof. Dr.-Ing. Cameron Tropea
Mitberichterstatter:	PD Dr. habil. Ilia V. Roisman
Zweiter Mitberichterstatter:	Prof. Dr. Philippe Villedieu

Institut für Strömungslehre und Aerodynamik (SLA)

Tag der Einreichung:	30. November 2015
Tag der mündlichen Prüfung:	26. Januar 2016

Darmstadt 2016
D17

Abstract

Since 2006, it is known that ice particles at high altitudes in the vicinity of deep convective clouds can pose a threat to aviation safety. When flying through regions containing ice particles, ice particles can fragment upon impact onto the aircraft's engine and probe surfaces. These fragments can (partially) melt in the warm environment within the engine's compressor or heated probe and can stick to warm surfaces (partially) covered with a water film. In such conditions, more incoming ice particles can cool down the surfaces and can cause significant ice accretion. Engine core or aircraft probe icing potentially leads to performance loss and false air data indications.

Icing due to ice particles is a complex problem which includes ice particle impact onto dry and wet surfaces, particle melting, and ice accretion. Fundamental knowledge of the physical mechanisms governing these processes is limited. The physics are not yet fully understood and adequate models are very scarce. To advance the understanding and prediction of icing due to ice particles, several experimental and theoretical investigations were conducted in this work.

To understand the physics of ice particle impact onto a dry surface better, impact experiments were conducted within an icing wind tunnel. Four different ice particle fragmentation modes were defined. Velocity scales and probability distributions for different fragmentation modes were successfully derived based on a model for the impact of semi-brittle spherical impactors onto a flat, rigid target. The restitution coefficients and post-impact angles of the fragments were observed to decrease with increasing particle diameter and impact velocity. The derived scaling laws agreed well with the restitution coefficients and post-impact angles of the fragments of large hail particles.

To predict the melting process of ice particles with higher accuracy, melting experiments of suspended ice particles were conducted in a controlled airflow using an acoustic levitator. The melting processes of individual spherical and non-spherical ice particles were observed. A melting model for ice particles was introduced and adapted using two different approaches to approximate the particle surface area (i.e. the sphericity) of non-spherical ice particles. The model was successfully validated with spherical ice particles. The predicted melting times of non-spherical ice particles agreed very well with the experimental data.

To expand the knowledge of ice particle impacts onto wetted surfaces, an experimental test apparatus was built which allowed the investigation of ice particle impacts onto a thin, controlled water film. The film thickness was between 130 and 600 µm. Sticking, bouncing, and fragmentation impacts of spherical ice particles were observed. It was determined that ice

particles can impact a thin water film with nearly double velocity – compared to a dry wall – before fragmentation occurs.

The mechanisms initiating ice accretion on a surface in a stream of fully frozen ice particles were experimentally observed on a microscale level. It was determined that target surface temperatures above freezing generated meltwater droplets by melting tiny ice fragments which deposited on the warm surface. These droplets allowed larger ice particles to stick to the surface due to capillary forces, potentially resulting in macroscopic ice accretion. It was also observed that meltwater covering partially melted ice particles can deposit on the target surface upon impact and initiate ice accretion as well.

The investigations conducted in this thesis allow a better prediction of the fragmentation modes of ice particles upon impact onto dry and wet surfaces. The knowledge of the initial post-impact trajectories of the fragments allows a better prediction of particles' and fragments' trajectories and so of potential ice accretion locations within aircraft engines and probes. Applying the melting model for ice particles, the melt ratios of the ice particles upon impact - which determine icing severity - can be calculated more accurately. The main mechanisms which initiate ice accretion were identified, allowing for an efficient search for adequate countermeasures, like using superhydrophic, smooth surfaces, to reduce or delay ice accretion in future engines or probes.

Kurzfassung

Seit 2006 ist bekannt, dass Eispartikel in großen Höhen, die in der Nähe von Gewitterwolken vorkommen, eine Gefahr für die Sicherheit des Luftverkehrs darstellen können. Während des Fluges durch solche Eispartikelregionen können die Eispartikel durch den Aufprall auf Oberflächen der Triebwerke oder Messsonden fragmentieren. Diese Fragmente können in der warmen Umgebung des Verdichters oder der beheizten Messsonden (partiell) schmelzen und können an warmen Oberflächen, die (partiell) von einem Wasserfilm bedeckt sind, anhaften. Unter diesen Bedingungen können weitere ankommende Eispartikel die Oberflächen abkühlen, was zu signifikanten Eisanlagerungen führen kann. Vereisungen im Kern des Triebwerks bzw. der Messsonden kann zu Leistungseinbußen sowie zur falschen Anzeige von Flugdaten führen.

Die Vereisung aufgrund von Eispartikeln ist ein komplexes Problem, welches den Aufschlagsprozess von Eispartikeln auf trockenen und mit Wasser benetzten Oberflächen, den Schmelzprozess von Eispartikeln sowie das Zustandekommen des Eisansatzes beinhaltet. Das Grundlagenwissen zu den physikalischen Mechanismen, die diese Prozesse beherrschen, ist sehr limitiert. Die relevante Physik ist noch nicht vollständig verstanden und geeignete Modelle sind kaum vorhanden. Um das Verständnis sowie die Vorhersage der Vereisung aufgrund von Eispartikeln zu verbessern, wurden mehrere experimentelle und theoretische Untersuchungen in dieser Arbeit durchgeführt.

Um die Physik des Aufpralls von Eispartikeln auf trockenen Oberflächen besser verstehen zu können, wurden Aufprallexperimente mit Hilfe eines Eiswindkanals durchgeführt. Vier verschiedene Fragmentierungsmodi wurden definiert. Eine Skalierung für die Geschwindigkeit sowie Wahrscheinlichkeitsverteilungen für verschiedene Fragmentierungsmodi wurden erfolgreich hergeleitet. Dafür wurde ein Modell verwendet, das den Aufschlag eines halbspröden, kugelförmigen Stoßkörpers auf eine ebene, starre Wand beschreibt. Die Stoßzahlen sowie die Winkel der Fragmente nach dem Aufprall wurden mit zunehmendem Partikeldurchmesser und zunehmender Aufprallgeschwindigkeit kleiner. Die hergeleiteten Skalierungsgesetze stimmten gut mit den Stoßzahlen und den Winkeln der Fragmente nach dem Aufprall von großen Hagelpartikeln überein.

Um den Schmelzprozess von Eispartikeln mit höherer Genauigkeit vorhersagen zu können, wurden Schmelzexperimente mit freischwebenden Eispartikeln in einer kontrollierten Luftströmung durchgeführt. Dazu wurde ein akustischer Levitator verwendet. Das Schmelzen einzelner kugelförmiger und nicht-kugelförmiger Eispartikel wurde beobachtet. Ein Modell,

welches den Schmelzvorgang von Eispartikeln beschreibt, wurde vorgestellt. Dieses wurde auf zwei verschiedene Arten angepasst um die Partikeloberfläche (d.h. die Sphärizität) eines nicht-kugelförmigen Eispartikels zu approximieren. Das Modell wurde mit Hilfe von kugelförmigen Eispartikeln erfolgreiche validiert. Die vorhergesagten Schmelzzeiten der nicht-kugelförmigen Eispartikel stimmten sehr gut mit den experimentell gewonnenen Schmelzzeiten überein.

Um das Wissen bezüglich des Aufpralls von Eispartikeln auf benetzten Oberflächen zu erweitern, wurde ein experimenteller Versuchsaufbau geschaffen, der die Untersuchung von Eispartikelaufprallprozessen auf einem dünnen, kontrollierten Wasserfilm erlaubt. Die Dicke des Films lag zwischen 130 und 600 µm. Aufprallprozesse von kugelförmigen Eispartikeln wurden beobachtet, die ein Anhaften, Abspringen oder Fragmentieren des Eispartikels zeigten. Es wurde festgestellt, dass Eispartikel mit der doppelten Geschwindigkeit auf einem dünnen Wasserfilm aufprallen können - im Vergleich zum Aufprall auf einer trockenen Wand -, ohne dass diese fragmentieren.

Die Mechanismen, die Eiswachstum auf einer Oberfläche, die einem Strom von gänzlich gefrorenen Eispartikeln ausgesetzt ist, initiieren, wurden experimentell mit einer hohen Auflösung von wenigen Mikrometern pro Pixel beobachtet. Es wurde festgestellt, dass sich auf einer warmen Wand, die Temperaturen über 0 °C aufwies, kleine Schmelzwassertröpfchen bildeten, die durch das Schmelzen winziger abgelagerter Eisfragmente zustande kamen. Diese Tröpfchen erlaubten größeren Eispartikeln das Anhaften an der Oberfläche durch Kapillarkräfte, was potentiell zu einem makroskopischen Eisansatz führen kann. Es wurde auch beobachtet, dass sich Schmelzwasser, welches partiell geschmolzene Eispartikel umgibt, beim Aufprall auf Oberflächen ablagern kann und ebenso Eiswachstum initiieren kann.

Die in dieser Arbeit unternommenen Untersuchungen erlauben eine bessere Vorhersage der Fragmentierungsmodi von Eispartikeln beim Aufprall auf trockene und benetzte Oberflächen. Die Kenntnis der anfänglichen Trajektorien der Fragmente nach dem Aufprall erlauben eine bessere Vorhersage der Partikel- und Fragmenttrajektorien und damit eine bessere Vorhersage der Orte innerhalb von Flugzeugtriebwerken und –sonden, wo Eiswachstum stattfinden kann. Durch die Anwendung des Schmelzmodells für Eispartikel kann das Schmelzverhältnis der Eispartikel zum Zeitpunkt des Aufpralls genauer berechnet werden. Dies ermöglicht eine bessere Einschätzung des Schweregrads der Vereisung. Die hauptsächlichen Mechanismen, die Eiswachstum initiieren, wurden identifiziert. Dies erlaubt eine effiziente Suche nach adäquaten Gegenmaßnahmen, wie die Anwendung von superhydrophoben, glatten

Oberflächen um das Eiswachstum in zukünftigen Triebwerken und Sonden zu reduzieren oder hinauszuzögern.

Table of Contents

List of Figures

List of Tables

List of Symbols

Roman Symbols

a	Impression radius [m]
A	Surface area [m²]
AR	Area ratio [-]
c_p	Specific heat capacity [J/(kg K)]
C	ISO circularity [-]
C_d	Drag coefficient [-]
d	Volume-equivalent sphere diameter [m]
D	Diameter [m] or: diffusivity [m²/s]
e	Restitution coefficient [-]
h	Convective heat transfer coefficient [W/(m² K)]
H	Enthalpy [J] or: film height [m]
IWC	Ice water content [kg/m³]
k	Thermal conductivity [W/(m K)]
k_c	Mass transfer coefficient [m/s]
K_c	Fracture toughness [MPa $m^{1/2}$]
l	Characteristic length [m]
l_{cr}	Crack length [m]
L	Length [m] or: latent heat [J/kg] or: ratio of kinetic to surface energy [-]
LWC	Liquid water content [kg/m³]
m	Mass [kg]
$\dot{m}_{ev}$	Evaporation (condensation) rate [kg/s]
$\dot{m}_f$	Melting (freezing) rate [kg/s]
$\dot{m}_{sub}$	Sublimation (deposition) rate [kg/s]
M	Molar mass [kg/mol] or: Mach number [-]

MMD	Median mass diameter [m]
MVD	Median volume diameter [m]
Nu	Nusselt number [-]
n_{total}	Total number of melting processes [-]
p	Pressure [kg/(m s²)]
P	Load [kg m/s²] or: perimeter [m]
Pr	Prandtl number [-]
$\dot{Q}_{latent}$	Latent heat transfer rate [J/s]
$\dot{Q}_{con}$	Convective heat transfer rate [J/s]
$\dot{Q}_{rad}$	Radiative heat transfer rate [J/s]
R	Radius [m]
Re	Reynolds number [-]
RH	Relative humidity [%]
Sc	Schmidt number [-]
Sh	Sherwood number [-]
Stk	Stokes number [-]
t	Time [s]
T	Temperature [K]
TWC	Total water content [kg/m³]
U	Velocity [m/s]
U_0	Impact velocity [m/s]
v	Velocity [m/s]
$\boldsymbol{v}$	Velocity vector [m/s]
V	Volume [m³]
y	Mass fraction [-]
Y	Yield strength [MPa]

Greek Symbols

α	Thermal diffusivity [m^2/s] or: post-impact angle [°]
δ	Dimensionless length of the crushed region [-]
$\bar{\Delta}_{rel}$	Mean value of the relative differences of the theoretical and experimental melting times [-]
ε	Emissivity [-]
η	Dynamic viscosity [kg/(s m)] or: dimensionless attrition propensity parameter [-]
ν	Kinematic viscosity [m^2/s]
ξ	Dimensionless variable [-]
ρ	Density [kg/m^3]
σ	Stefan-Boltzmann constant ($\sigma \approx$ 5.67 E-8 W m^{-2} K^{-4})
Φ	Sphericity [-]

Subscripts

$\perp$	Crosswise
0	Initial
a	Air
c	Critical
cr	Crack
d	Drag
em	End of melting
env	Environment
exper	Experimental
f	Fragment or: fusion
i	Ice
m	Mean

max	Maximum
melt	Melting
mix	Mixture
n	Normal
p	Particle
proj	Projected
R	Rebound
s	Surface
sat	Saturation
t	Tangential
theo	Theoretical
v	Vapour
w	Water
wb	Wet bulb

List of Abbreviations

AAIB	Air Accidents Investigations Branch
AF447	Air France Flight 447
AGARD	Advisory Group for Aerospace Research and Development
AMC	Acceptable Means of Compliance
ATR	Avions de Transport Régional
CPI	Cloud Particle Imager
CRYSTAL FACE	Cirrus Regional Study of Tropical Anvils and Cirrus Layers – Florida Area Cirrus Experiment
EASA	European Aviation Safety Agency
EHWG	Engine Harmonization Working Group
EIWG	Engine Icing Working Group
FAA	Federal Aviation Administration
FAR	Federal Aviation Regulation
HAIC	High Altitude Ice Crystals
HIWC	High Ice Water Content
ICAO	International Civil Aviation Organization
ICC	Ice Crystal Consortium
ICI	Ice Crystal Icing
iCORE	Icing and Contamination Research Facility
ISO	International Organization for Standardization
KWAJEX	Kwajalein Experiment
LBA	Large Scale Biosphere-Atmosphere Experiment
MT	Megha-Tropiques
NACA	National Advisory Committee for Aeronautics
NASA	National Aeronautics and Space Administration

NRC	National Research Council Canada
RATFac	Research Altitude Test Facility
SLD	Supercooled Large Droplet

1 Introduction and Motivation

Since the early days of aviation, flight in atmospheric icing conditions has been a serious threat to aircraft safety. In-flight icing can occur on aircraft probes, engines, and structures such as wings, fuselage, or horizontal/vertical stabilizers. In general, ice on aircraft structures leads to an increase of drag and, hence, increased fuel consumption to compensate for the higher drag. Occurrence of ice on the wings can additionally lead to a reduction of lift.

In-flight icing can originate from *small supercooled droplets* (liquid droplets whose temperature is below freezing) with median volume diameters (MVD) smaller than 50 µm, from *supercooled large droplets* (SLDs) with MVDs larger than 50 µm, and from *ice particles*.

In-flight icing caused by *small supercooled droplets* which freeze upon impingement onto a solid surface is the most commonly encountered form of in-flight icing. It has been known for a long time and has been investigated in detail in the past[1–3]. As a result, the Acceptable Means of Compliance (AMC)[*] are well defined[4] and represented by, e.g. the FAR Part 25 Appendix C icing envelopes[5], partly illustrated in Figure 1-1. These envelopes define the icing conditions taking into account cloud liquid water content, droplet diameter, ambient temperature, altitude, and the horizontal extent of the icing area. Based on these AMC, aircraft can be certified for flight into clouds consisting of small supercooled droplets. When flying in these icing conditions, detection and awareness systems as well as countermeasures such as de-icing and anti-icing systems are successfully applied[6,7].

Supercooled large droplets were long thought to not pose a threat to aircraft safety. However, when an ATR-72 (American Eagle Flight 4184) crashed near Roselawn, Indiana, in 1994, SLDs came into focus. SLDs, which do not freeze completely upon impact due to their large size, show significant splashing and re-impingement and water may run back along aircraft surfaces. Thus, SLDs can lead to ice accretion at areas not protected by de- and anti-icing systems which are based on Appendix C. In the case of American Eagle Flight 4184, ice accreted in front of the ailerons which disturbed the flow over them and led to uncontrolled aileron deflections. As a result of subsequent investigations and flight test programmes, the FAR Part 25 Appendix O was developed to guarantee safe flight in SLD icing conditions.

[*] Before new aircraft types enter into operation or as soon as new safety-relevant phenomena are discovered, aircraft manufacturers and aviation regulatory authorities (e.g. EASA or FAA) must jointly define the AMC. Safety requirements must be met in different fields such as structure, engine, and flight performance to obtain a type-certificate (https://easa.europa.eu/easa-and-you/aircraft-products/aircraft-certification (accessed: 13th November 2015)). For example, safe operation in in-flight icing conditions must be demonstrated.

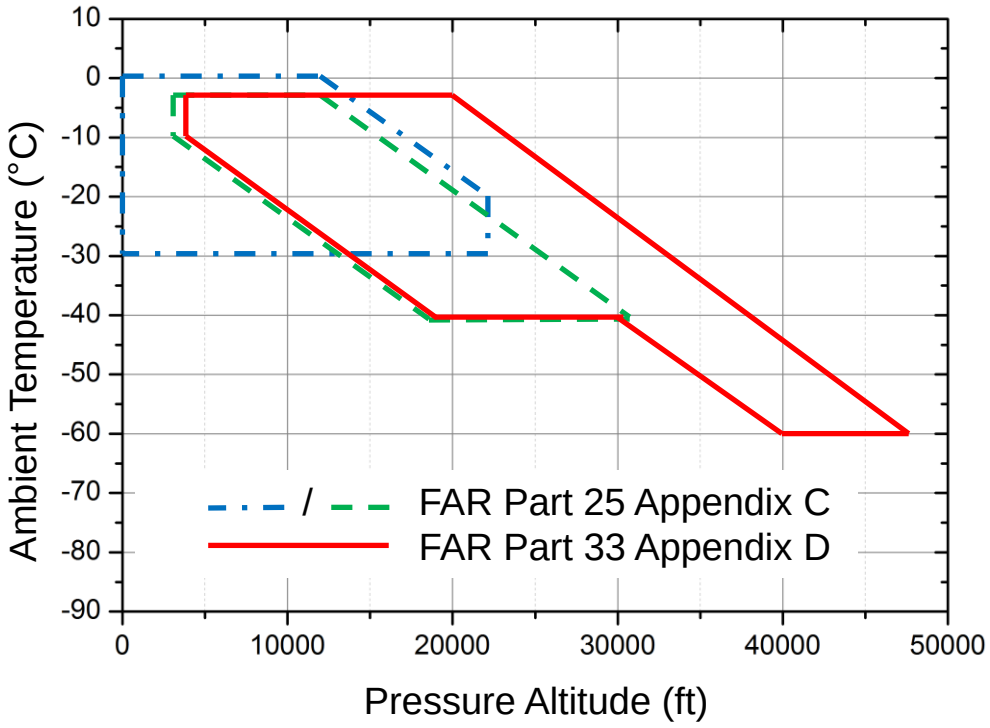

Figure 1-1. Illustration of Appendix C icing envelopes valid for icing due to small supercooled droplets. Envelope surrounded by blue dash dot line represents continuous maximum icing conditions. Envelope surrounded by green dash line represents intermittent maximum icing conditions. Proposed Appendix D envelope for glaciated icing conditions is also shown. Pressure altitude describes the altitude in the frame of the ICAO standard atmosphere taking into account the actual pressure. On a standard day, pressure altitude and actual altitude are the same.

In-flight encounters with *ice particles* at high altitudes were originally considered to not pose a threat to aviation safety: ice particles were believed to simply bounce off exposed, cold engine and airframe surfaces. Hence, ice accretion would not occur on any parts of the aircraft. However, since the 1990s, according to a database from Boeing[8], more than 160 engine icing events of commercial aircraft have been reported in the vicinity of deep convective clouds (e.g. anvils of thunderstorms (Figure 1-2) or tropical storms). These events happened mostly outside of the Appendix C envelopes at higher temperatures than on a standard day[†] (according to the International Civil Aviation Organization (ICAO) Standard Atmosphere) and mostly above 22,000 ft, where supercooled liquid water in clouds was thought to be unlikely to occur.

[†] 15 °C at sea level and constant gradient of -1.98 °C/1000 ft up to 36,089 ft

Figure 1-2. Anvil of a thunderstorm consisting of ice particles.

The Engine Harmonization Working Group (EHWG) concluded in 2006[9] that these engine events were most likely the result of the ingestion of a high mass concentration of ice particles. These atmospheric conditions, where a high concentration of ice particles and no liquid water are present, are called *glaciated icing conditions*. In these conditions, a previously unrecognized form of icing called *ice crystal icing* (ICI) can occur. A preliminary icing envelope has been defined in FAR Part 33 Appendix D[10] to account for mixed-phase and glaciated icing conditions (Figure 1-1). In *mixed-phase conditions*, both ice particles and supercooled droplets are present.

Bravin et al.[8] analysed the Boeing database in detail and found that 92 % of the engine events occurred in the tropics and subtropics between the 38th parallels of each hemisphere. The highest number of events was found in Southeast Asia and Japan. The majority of the events (>80 %) took place in the local spring and summer months (i.e. April-September in the northern hemisphere and October-March in the southern hemisphere) when atmospheric convection is stronger in comparison to autumn and winter due to increased solar heat flux. Clouds with high mass concentrations of ice particles can originate from continental or oceanic deep convection. Their detailed characteristics are still under investigation[11,12]. Within these deep convective clouds relatively humid air, initially located close to the earth's surface, is heated and rises high into the troposphere, sometimes even penetrating the stratosphere[13]. Depending on ambient temperature, supersaturation relative to ice, and vapour diffusivity, different shapes of ice particles can be generated[14–16].

During several measurement campaigns in the last 20 years, e.g. the Large Scale Biosphere-Atmosphere Experiment (LBA) in Brazil[17], the Cirrus Regional Study of Tropical Anvils and Cirrus Layers - Florida Area Cirrus Experiment (CRYSTAL FACE) project in the US[18], the Kwajalein Experiment (KWAJEX) on the Marshall Islands[19] and the Megha-Tropiques (MT) project over West Africa and the Indian Ocean[20], data about ice particles in deep convective clouds have been collected.

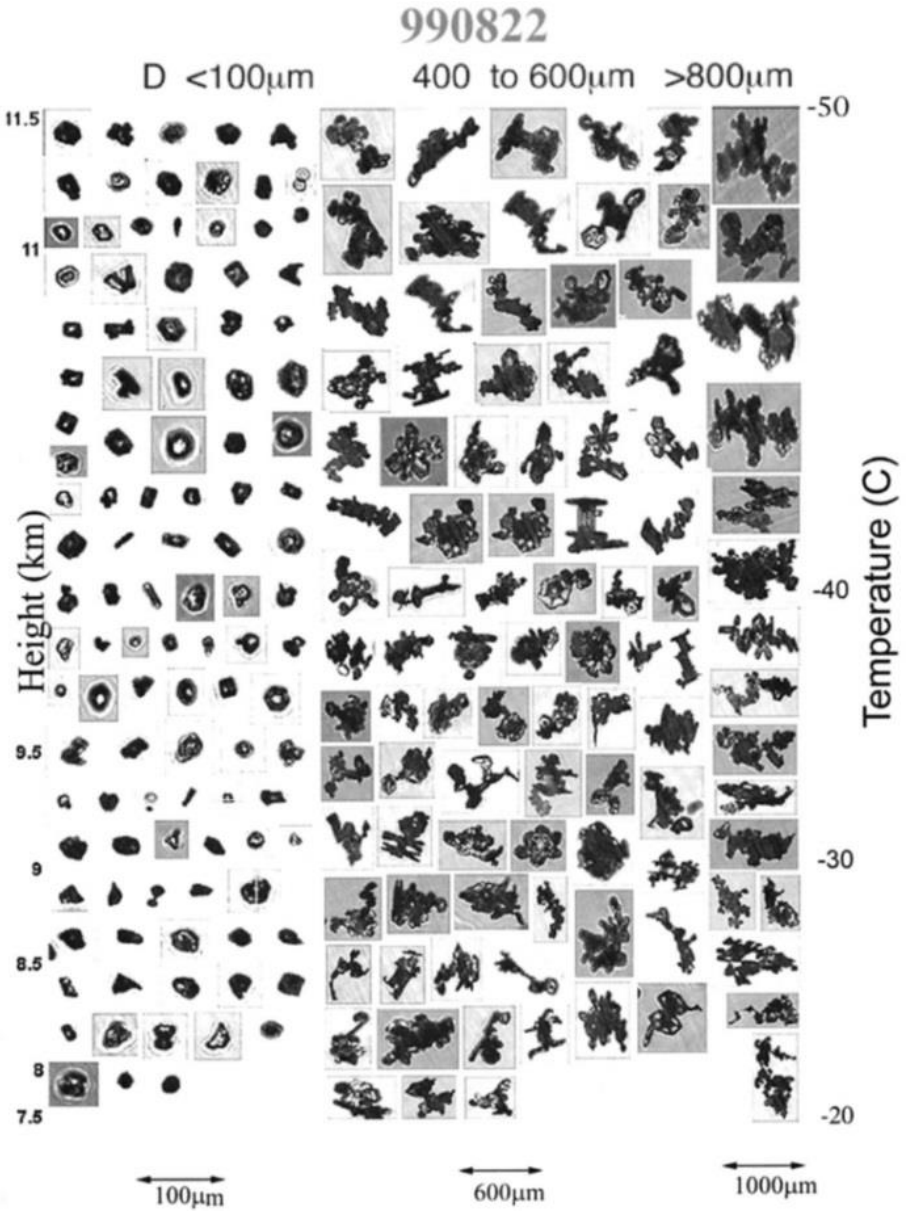

Figure 1-3. Examples of ice particles vs. altitude (km) and temperature (°C) imaged in three size ranges ($< 100, 400–600, > 800$ µm) by CPI probe on August 22nd, 1999. Magnification between different size ranges varies.[21] ©American Meteorological Society. Used with permission.

The data show that ice particles may occur in the form of non-spherical shapes, aggregates, and more pristine crystals (e.g. plates and columns). Moreover, the maximum dimension of different ice particles varies between several microns and a few millimetres. In Figure 1-3, typical ice particles are grouped in three size ranges, which were recorded by the Cloud Particle Imager (CPI) probe on August 22nd, 1999 during KWAJEX. The samples were taken in close proximity to deep updrafts on heights between 7.5 and 11.5 km[‡]. Single rimed ice particles with non-spherical shapes, generated by the collision of original ice particles with supercooled droplets, and some aggregates of rimed ice particles can be seen in the intermediate and large size ranges. In the smallest size range, these particles are closer to a spherical shape.

ICI events are based on engine core icing and ice shedding in the compressor stages, where the local air temperature is higher than 0 °C. In glaciated icing conditions, ice particles hit cold surfaces in the front of the engine first, e.g. inlet, spinner, or fan (Figure 1-4). A share of the ice particles may be deflected into the cold bypass airflow where they do not represent a threat. The other share of particles enters the engine core further downstream, where the air temperature rises due to adiabatic compression. The smaller ice particles may totally or partially melt due to the warm engine airflow leading to mixed-phase conditions[22]. First, the mixture of solid and liquid particles may form a thin liquid film or droplets on internal engine flow-path surfaces which are initially above freezing temperature. Second, as a result of the presence of water on the surfaces (or on partially melted ice particles), more and more particles may stick to the engine flow-path surfaces generating *slushy layers* consisting of meltwater and ice. Third, further impacting ice particles, which were initially well below freezing temperature, are captured by the slushy layers and may cool down these layers and the surfaces to freezing temperature. Refreezing and significant ice accretion may then occur. With increasing size of the accreted ice, the aerodynamic forces on the accreted ice increase and may eventually result in ice shedding.

[‡] 1 km ≈ 3,281 ft

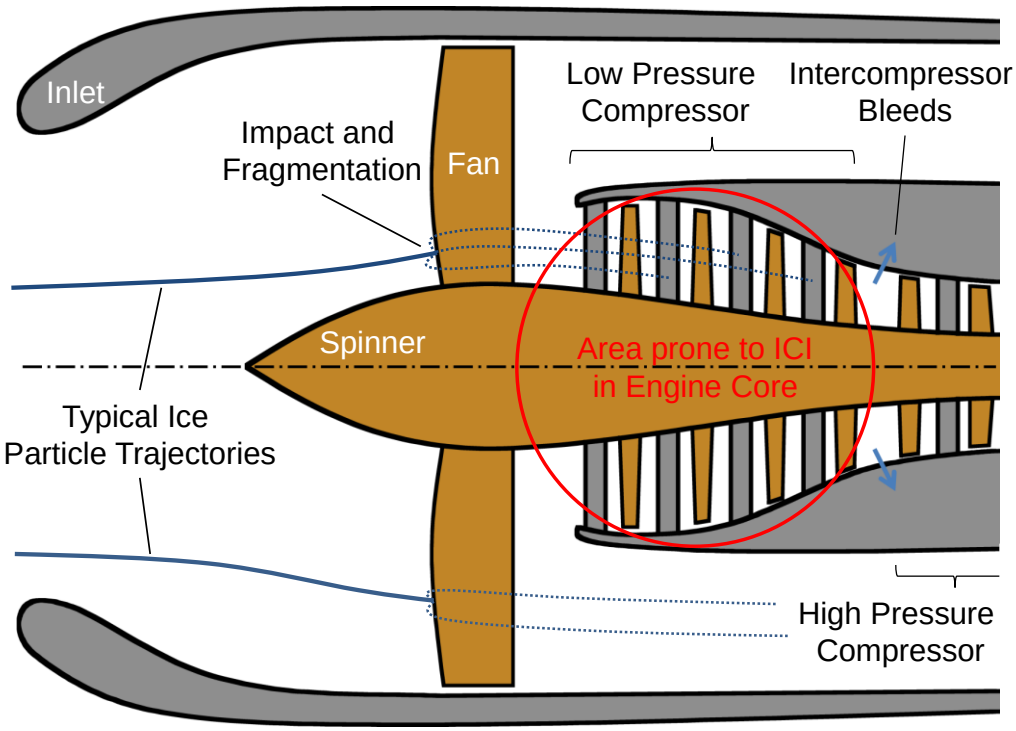

Figure 1-4. Sketch of typical turbofan engine. Typical trajectories of ice particles are shown. Inlet, fan, and spinner are illustrated where fully frozen ice particles may impact and fragment. Ice particles entering the engine core may melt and accrete on surfaces of the low pressure compressor, whereas ice particles in the bypass airflow are not a threat. The intercompressor bleeds between the low and high pressure compressors may remove shed ice into the bypass airflow if open.

As discussed by Mason et al.[9], in ICI conditions compressor stall and surge, engine flameout, and damage to compressor blades and vanes can occur depending on the engine type. *Compressor stall* is a relatively minor disruption of the airflow in a jet engine compressor originating from local airfoil stalls and resulting in a reduction of the compressor's efficiency. The breakdown of the whole compression is called *compressor surge* which results in a flow reversal and may seriously damage compressor blades and vanes. *Engine flameout* is the extinction of the flame in the combustion chamber leading to engine run-down and the subsequent performance of relight attempts.

Glaciated icing conditions have caused several serious incidents in the past. In at least 14 cases, ICI led to multi-engine flameouts[23,§] with subsequent partial or full recovery of thrust in lower altitudes. In one case, a dual engine flameout occurred on a twin engine aircraft and engine power could not be recovered resulting in a forced landing without propulsive power ("dead stick landing")[24]. Ice crystals cannot only cause engine events. They can also accrete on surfaces of aircraft probes. For example, the obstruction of the Pitot probes by ice particles

§ http://aviationweek.com/bca/high-altitude-ice-crystal-icing (accessed: 13th November 2015)

of Air France Flight 447 (AF447) in cruise altitude resulted in the temporary failure of the airspeed indicators and was a contributing factor to its crash on 1st June 2009[25]. In another incident, which happened in 2010, significant vibrations in the engines occurred during a prolonged flight in glaciated icing conditions. In this case, investigators of the Air Accidents Investigations Branch (AAIB) came to the following conclusions (amongst others) in 2011[26]:

- Glaciated icing conditions are not yet well understood
- Further data about glaciated icing conditions should be gathered
- Based on this data new certification requirements for engines should be developed
- Glaciated icing conditions are not yet detectable by existing on-board weather radars
- *"The knowledge of these conditions, and their effect upon various aircraft systems, is at present limited"*

EASA also stated in 2011[27,28]: *"It has been evidenced that the icing environment used for certification of large aeroplanes and turbine engines needs to be expanded in order to improve the level of safety when operating in icing conditions."* And: *"These particular severe icing conditions* (remark from author: glaciated and SLD icing conditions) *are not included in the current certification icing environment for aircraft and engines.""*

Currently, there are recommendations to avoid deep convective clouds by at least 50 NM and to avoid the downwind regions where ice particle anvils could be located. Some airlines have imposed costly flight route restrictions to avoid glaciated icing conditions. Engine manufacturers aim at maintaining an acceptable surge margin (i.e. the margin between operating point and compressor surge) by using the intercompressor bleeds (Figure 1-4), normally used to remove excess air into the environment, to remove shed ice from the engine core. As a result, less ice may enter the high pressure compressor and combustion chamber[**]. However, opening the intercompressor bleed valves in cruise flight may reduce engine efficiency.

To increase the understanding of ICI and to optimise aircraft safety in glaciated icing conditions, several projects and working groups focus on ice crystal icing research. Examples

[**] http://www.flightglobal.com/news/articles/genx-icing-issue-prompts-747-8-787-restriction-route-393439 (accessed: 13th November 2015)

are the High Ice Water Content (HIWC) and High Altitude Ice Crystals (HAIC) projects as well as the Ice Crystal Icing Consortium (ICC) and the Engine Icing Working Group (EIWG).

The work performed during this PhD thesis was part of the European HAIC project, partially funded by the European Commission. HAIC comprises more than 30 partners, was started in August 2012, and has a duration of 4.5 years. The main goal of the HAIC project is the provision of the Acceptable Means of Compliance including numerical and experimental test capabilities to demonstrate safe flight in glaciated icing conditions.

This PhD thesis focuses on the investigation of the melting process of ice particles, ice particle impact onto dry and wet surfaces, and ice accretion due to ice particles. Experimental data and adequate models in these research fields are very scarce. To be able to simulate ICI phenomena and to contribute to the AMC with the ultimate goal of increasing aircraft safety in glaciated icing conditions, further experimental data is collected and adequate models are developed in this thesis.

1.1 Goals of the Presented Work

Cost-efficient simulation tools for the prediction of ice accretion in glaciated icing conditions are crucial for the certification of current and future aircraft probes and engines. However, there is a significant lack of fundamental knowledge, experimental data, and adequate models. For this reason, the goals of the presented work are:

- Expansion of the limited phenomenological knowledge of how ice crystal ice accretion starts on a microscale level. Exploratory experimental investigations allowing detailed observations of the initial mechanisms of ice accretion on cold and warm surfaces were conducted.
- Investigation of the impact process of ice particles onto a dry, cold surface. Development of impact models describing the thresholds between and the probabilities of different fragmentation modes for ice particles. Analysis of the post-impact velocities and angles of the fragments for inferring the starting conditions of the post-impact trajectories.
- Investigation of the melting process of individual spherical and non-spherical ice particles. Adaption of an adequate thermodynamic melting model capable of taking into account also the sphericity of particles to accurately predict melting times.
- Investigation of impacts of spherical ice particles onto a thin water film in a subfreezing environment. Validation of the design of the test apparatus and collection of an experimental database for supporting future model development.

1.2 Outline

In chapter 2, the fundamentals and state-of-the art of four issues relevant for the prediction of ice crystal icing (ICI) are presented: (i) ice particle impact onto a dry, cold surface, (ii) ice particle melting in forced convection, (iii) (ice) particle impact onto a liquid film, and (iv) ice accretion in mixed-phase and glaciated icing conditions. Relevant studies from literature are introduced and crucial topics within these subjects are identified, which need further investigations to improve the prediction of ICI.

In chapter 3, the initial mechanisms which lead to ICI on a microscale level are investigated experimentally. The influence of a warm surface temperature - instead of a subfreezing surface temperature - on ice accretion in glaciated icing conditions is discussed.

Chapter 4 describes the experimental and theoretical investigations of ice particle impact onto a dry, cold surface. Definitions and observations of four different particle fragmentation modes are presented. Velocity scales for spherical ice particles impacting onto a flat, rigid surface as well as probability distributions for different fragmentation modes are derived. The post-impact behaviour of the fragments is analysed.

In chapter 5, the melting of spherical and non-spherical ice particles in forced convection is investigated. The test apparatus and a typical melting process are presented. A melting model for ice particles is introduced and extended to non-spherical ice particles. Experimental and theoretical melting times are compared and the results are discussed.

In chapter 6, a test apparatus for the experimental investigation of ice particle impact onto a thin water film is introduced. Typical impact outcomes are presented and the occurrence and influence of capillary bridges is discussed.

Chapter 7 comprises a summary with conclusions and outlook.

2 Fundamentals and State-of-the-Art

Ice crystal icing in an aircraft engine is a complex process which can be divided into several sub-processes:

- Ice particle impact onto a dry, cold surface in the front of the engine (e.g. inlet, spinner, or fan),
- (partial) ice particle melting in the warm compressor airflow in the engine core,
- ice particle impact onto a (warm) surface covered with a liquid film, which may finally promote
- ice accretion due to the sticking of further incoming ice particles.

To better understand the fundamental physics of ICI, these sub-processes can be investigated individually - rather than as a whole - since their time and length scales are different. For example, ice particle impact onto a cold surface is a process normally lasting only few milliseconds, and needs to be observed on a microscale level because of the small size of the ice particles. In contrast to ice particle impact, ice accretion is a longer process - typically lasting several minutes - and can be well observed on a macroscale level (e.g., ice accretion may extend along a stator blade).

Relevant investigations and basic knowledge focusing on these four sub-processes are described in the following sections.

2.1 Ice Particle Impact onto a Dry, Cold Surface

Research on fundamental physics of ice particle impact is of interest in many disciplines, e.g. in planetary science, in atmospheric science, and, recently, in aeronautical science. Experimental and theoretical studies typically focus on the better prediction of the impact and post-impact behaviour of the ice particles and fragments. That includes the threshold velocity which separates no fragmentation from fragmentation, and the post-impact velocities, angles, and size distributions of the generated ice particles. The impact process is typically determined by the ice particle's size, velocity, temperature, impact angle, and the target's properties.

In planetary science the understanding of the mutual impact of ice particles is of importance, e.g., to improve the simulation of Saturn's ring system. Higa et al.[29,30] investigated the normal

impact of spherical ice particles onto ice blocks with sphere diameters ranging from 2.8 to 72 mm and impact velocities between 0.01 and 10 m/s. The ambient temperature was varied between 113 and 269 K. The authors defined a *critical velocity* v_c, which divided the quasi-elastic region (restitution coefficient e = constant and close to 1) from the elastoplastic region (e decreased with increasing impact velocity). The restitution coefficient e is an important parameter for the characterization of the collision of two bodies. In general, it is defined as the ratio of the rebound velocity U_R to the impact velocity U_0:

$$e = \frac{U_R}{U_0}. \tag{2-1}$$

A perfectly elastic impact is characterized by $e = 1$ (total conservation of kinetic energy during impact and rebound), whereas a fully plastic impact is characterized by $e = 0$ (total dissipation of kinetic energy during impact). For $0 < e < 1$, the impact is elastoplastic. The critical velocity v_c represented also the onset velocity of *crack-type* impacts (except in the case of $D = 2.8$ mm), where tiny cracks as well as small fragments occurred. The critical velocities decreased with increasing particle diameter and increased with decreasing temperature. They ranged from 0.23 m/s ($D = 72$ mm) to 1.24 m/s ($D = 2.8$ mm) at a temperature $T = 261$ K. In Figure 2-1, the restitution coefficient versus impact velocity is shown for the smallest ice spheres investigated by Higa et al., which are closest to the relevant size range of high altitude ice crystals ($D = 2.8$ mm, $T = 261$ K). The critical velocity v_c is also shown. The hollow symbols represent *no-crack type* impacts, where no macroscopic fragmentation or deformation was observed. The filled symbols represent *crack-type* impacts. In the case of *crack-type* impacts with spherical ice particles of $D = 2.8$ mm, Higa et al. noted that the generated single fragments were too small to be observed although ice particle mass was lost. Impacts of ice spheres ($D = 2.8$ mm) with velocities between 2 and 3 m/s were not investigated by Higa et al. For this reason, the onset velocity of *crack-type* impacts is estimated and illustrated with the red vertical line ($v \approx 2.5$ m/s).

In atmospheric sciences, a profound understanding of the impact process of ice particles is crucial, e.g., to accurately detect natural ice particles with airborne instruments. For example, probe-induced fragmentation prior to the measurement of the particle mass can lead to an artificial decrease of the measured median mass diameter (MMD). Ice particle impact onto aircraft probes with diameters ranging from several microns to 2.5 mm have been analysed by Vidaurre & Hallett[31].

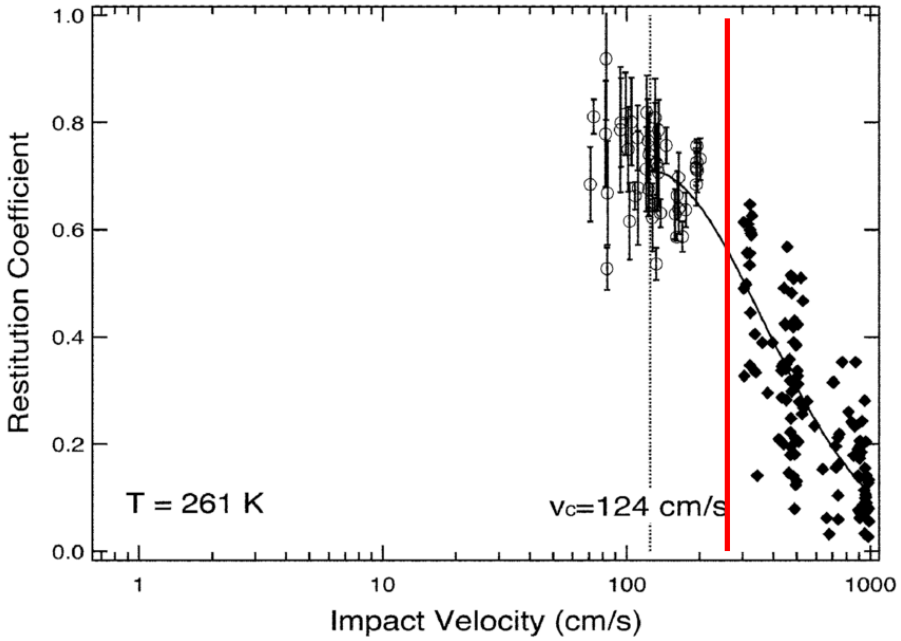

Figure 2-1. Restitution coefficient versus impact velocity for normal impacts of spherical ice particles onto an ice block. The diameter of the spheres was 2.8 mm. *No-crack type* (hollow symbols) and *crack type* impacts (filled symbols) were observed. The critical velocity v_c, the estimated onset velocity of *crack-type* impacts (vertical red line; $v \approx 250$ cm/s), and a best fit to the measured restitution coefficient (black line) are illustrated. Reprinted from Higa et al.[30] with permission from Elsevier.

The authors applied the ratio of particle kinetic energy to surface energy L to characterize the onset of ice particle fragmentation - a simplified approach which is commonly applied to droplet splashing:

$$L = \frac{D\rho_i U_0^2}{12\sigma_i} \qquad \text{for } 0.005 \leq D \leq 2.5 \text{ mm}, \tag{2-2}$$

where ρ_i is the density of ice ($\rho_i = 920$ kg/m^3 at T = -20 °C) and σ_i is the surface energy of ice ($\sigma_i = 0.12$ J/m^2 at T = -20 °C).
They concluded that the criterion used for the droplet splashing regime ($L > 7$) can also be applied to describe fragmentation of ice particles.

Particle bouncing and fragmentation onto several probes for measuring the liquid water content (LWC) and the total water content (TWC) were investigated by Emery et al.[32] and Isaac et al.[33] to allow for a more accurate interpretation of the measured ice water content (IWC) and TWC values. The authors concluded that the actual IWC and TWC are

underestimated due to neglect of some small particles or fragments generated during ice particle impact. The investigation of the influence of ice particle bouncing and fragmentation on measured IWC and TWC values as well as the optimization of current probes to minimize bouncing and fragmentation is ongoing.

In aeronautical sciences, the impact of hail particles, which have diameters between several millimetres up to a few centimetres, can lead to serious damage of aircraft structures and jet engines. Moreover, the ingestion of hail particles can cause engine power loss and flame outs. In the case of engine ingestion, hail particles impact onto cold engine parts, e.g. the spinner, inlet, or fan, before entering the engine core. For this reason, hail particle impact has been investigated in several studies. Guégan et al.[34] used a drop weight technique to determine the critical impact velocity for the fragmentation of spherical hail particles. The post-impact state of the particle was divided into a *non-altered* and an *altered* state. The *altered* state was characterized by the existence of cracks, fragments, or both, whereas the *non-altered* state was characterized by no apparent modifications of the shape of the spherical ice particles. The particle diameters were 12.9, 27.5, 37.4, and 42.0 mm. The impact velocity was varied between 1 and 5 m/s and three different impact angles were considered (45°, 70°, and 90°). Their model assumes that the *altered state* is observed if the kinetic energy is higher than a certain value of the deformation energy, which is proportional to the particle's surface area. The following function divides the non-altered from the altered state:

$$U_0{}^2 D = 0.135 \frac{\mathrm{m}^3}{\mathrm{s}^2} \qquad \text{for } 12.9 \leq D \leq 42.0 \text{ mm}, \tag{2-3}$$

where U_0 is the impact velocity and D is the particle's diameter. The model from Guégan et al. is similar to the AGARD model[35] which was also developed earlier to investigate hail impact. The function:

$$U_0{}^2 D = 0.463 \frac{\mathrm{m}^3}{\mathrm{s}^2} \qquad \text{for } 12.7 \leq D \leq 50.8 \text{ mm} \tag{2-4}$$

from the AGARD 332 report[35] separates the *bouncing* (*no fragmentation*) from the *shattering* (*fragmentation*) regime of spherical hail particles. Investigated particle diameters were 12.7, 25.4, and 50.8 mm.

The three presented threshold relations (Eqs. (2-2), (2-3), (2-4)) and a fit to the results from Higa et al. are shown in Figure 2-2 for the investigated diameter ranges, respectively.

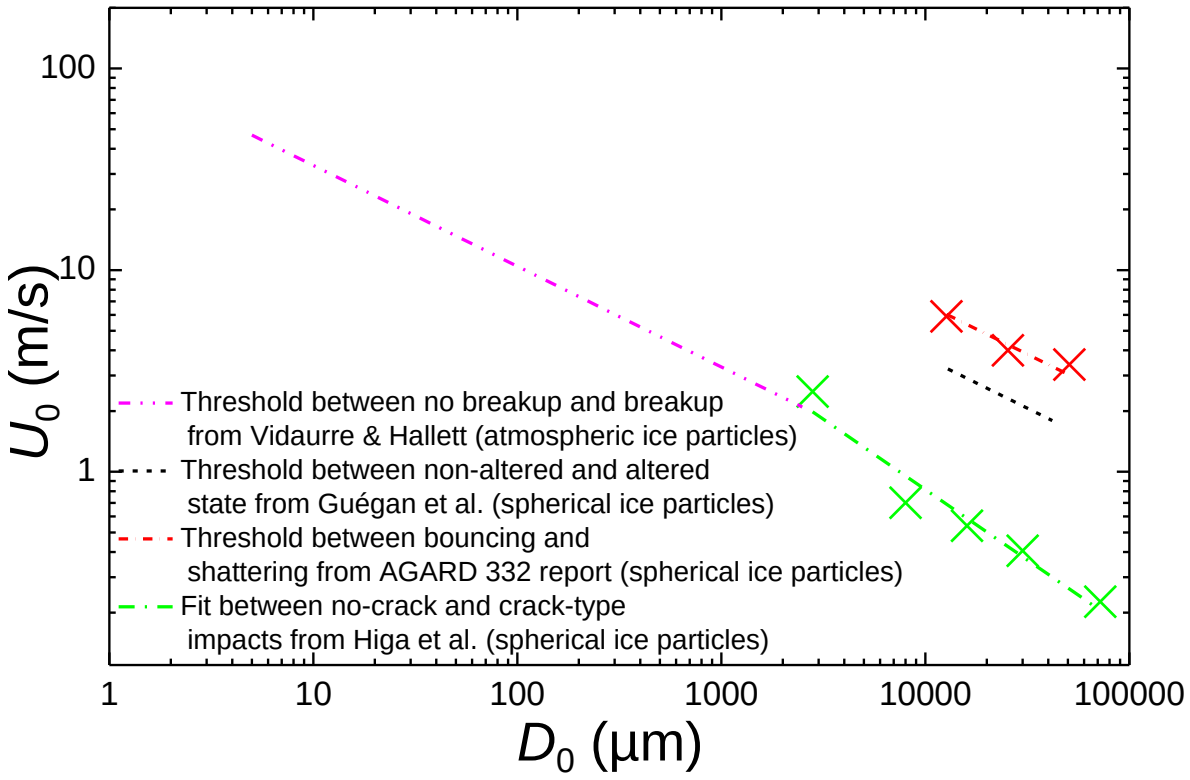

Figure 2-2. Thresholds are shown defined in Vidaurre & Hallett[31], Guégan et al.[34], and in the AGARD 332 report[35]. In the case of Higa et al.[30] and the AGARD 332 report, the experimental data on which the thresholds are based is shown (crosses). In the case of Higa et al., a fit has been added since the authors did not define a threshold formula. Thresholds and fit are shown for the investigated diameter ranges, respectively.

In Figure 2-2, the threshold from Guégan et al. is shifted towards smaller impact velocities in comparison to the threshold from the AGARD 332 report. This might be explained with the different definitions of the thresholds: Guégan et al. considered a spherical ice particle *altered* as soon as cracks could be observed (fragments were not required for this classification), whereas in the AGARD 332 report spherical ice particles were classified as *shattered* only if fragments were observed. Since upon impact, first, cracks are formed and, second, if the kinetic (impact) energy is sufficient, fragments are formed, the shift of the curve seems reasonable. The major difference between the threshold from Vidaurre & Hallett and the thresholds from Guégan et al. and from the AGARD 332 report might be explained with different optical resolutions. Since Vidaurre & Hallett observed much smaller (natural) ice particles than in the other two studies, the optical resolution was most likely higher in the case of Vidaurre & Hallett's investigations. The resolution in the study of Vidaurre & Hallett was ~1 µm/pixel. The resolutions were not mentioned in the other two studies. However, in a

comparable impact study[36] with similar diameters of the spherical ice particles the resolution was > 250 µm/pixel. For this reason, tiny fragments of up to ~250 µm could have remained undetected in studies where only the impacts of relatively large spherical ice particles were investigated, leading to higher threshold velocities. In contrast to the three aforementioned studies, where ice particles/spheres impacted onto rigid surfaces (glass or metal), Higa et al. investigated the impact of spherical ice particles onto ice blocks. Elastoplastic deformation and fragmentation of both the spherical ice particle and the ice block were observed. Assuming that Higa et al. would have used a rigid surface instead of an ice block, a shift of the threshold velocity towards lower velocities would have been expected, since only the spherical ice particles could have been subject to deformation and fragmentation absorbing (part of) the impact energy. The relatively low threshold in the case of Higa et al. is hard to explain. Again, a better optical resolution could be a reason for this shift since they (also) investigated spherical ice particles which had one fifth of the diameter of the spherical ice particles investigated by Guégan et al. and in the AGARD 332 report. Moreover, the ice particle generation technique and the resulting inner structure/shape of the particle could influence the thresholds. For example, Vidaurre & Hallett investigated natural ice particles, whereas in the three other studies different molding techniques or liquid nitrogen were used for generation of the spherical ice particles. In another study of Guégan et al.[37] spherical ice particles were shot onto a glass plate with a gas gun to investigate the kinematics of post-impact ice fragments. The diameters of the spherical ice particles ranged from 6.2 to 27.5 mm. The impact velocities varied between 60 and 200 m/s, a range in which the spherical ice particles always split into hundreds of fragments upon impact. Four different impact angles were chosen (20°, 45°, 67°, 90°). It was observed that the angle between the fragments' velocity vectors and the surface was smaller than 2° at all impact conditions. Furthermore, the velocity of the centre of the fragment cloud was as large as the tangential velocity of the spherical ice particle before the impact. Pan & Render[36,38,39] performed several studies on hail impact onto flat plates, rotating spinners, and fans. Spherical ice particles with diameters of 12.7 and 19 mm, impact velocities between 102 and 175 m/s, and several impact angles (e.g. 30°, 45°, 60°, and 90° in the case of a flat plate target) were considered. Pan & Render concluded that the Rosin-Rammler distribution, which is commonly used for representing particle size distributions generated by grinding, milling, and crushing processes, can be applied as well to describe the post-impact particle size and velocity distributions of hail particles impacting onto flat plates. The post-impact mass distributions were obtained with a "patternator" which consisted of several square steel tubes. The patternator collected

the ice fragments behind the target and allowed the measurement of their mass at different locations. In the case of the stationary and rotating spinner, post-impact mass distributions were not influenced by the rotation. In the case of the rotating fan, blade shape, angular speed, and impact angle varied with the impact position. For this reason, the particle mass distribution behind the fan depended significantly on the impact position. Tippmann et al.[40] developed a strain rate sensitive ice material model for hail impact simulation. In their experiments, spherical ice particles with diameters from 39.1 mm to 61.0 mm were accelerated with a gas gun and hit an aluminium target normally. Impact velocities varied between 45 and 189 m/s. Upon impact, particle crushing close to the contact point resulting in the ejection of a cloud of tiny fragments and the subsequent formation of cracks parallel to the direction of travel in the rear part, breaking it into small fragments, were observed. The experimentally measured and simulated forces during impact acting on the target agreed well.

Studies dealing with the impact process of small non-spherical and spherical ice particles ($D < \sim 3$ mm) - in the frame of ice crystal icing in aircraft engines and probes - were literally non-existent till 2006. However, since the work of Mason et al.[9], the icing community has focused on the threat of ice particles to safe aircraft operation and a few studies have been conducted. A better understanding of the (post-) impact dynamics and properties of small ice particles or fragments within an engine or probe is crucial to predict potential ice accretion locations. In 2014, Vargas et al.[41] investigated the impact of ice particles onto a moving wedge. The diameter of the spherical ice particles varied from 1.5 to 3.0 mm. Impact velocities were between 7 and 120 m/s. The impact angle was set to 30°, 45°, 60°, or 90°. The authors showed that upon impact the fragments, which form the edge of the fragment cloud, initially have a higher velocity than the impact velocity of the original spherical ice particle. Moreover, at an impact velocity of 120 m/s the fragments left the impact spot under a shallow angle. These observations are in line with the observations made in the aforementioned hail impact investigations. In a more recent study from 2015, Vargas et al.[42] investigated the impact of spherical ice particles, whose diameters ranged from 2.0 to 4.6 mm, onto a glass plate. The impact angle was 45° and the velocity was varied from 20 to 130 m/s. The authors observed that fragment size decreased with increasing velocity. They obtained histograms showing the size distributions of the fragments. Most of the fragments were found near the resolution limits which ranged from 22.4 to 100 µm/pixel. Recently, Roisman & Tropea[43] developed ice particle impact models for spherical and cylindrical shapes which predict the impact duration, the generated peak force onto the target, and the residual height of the ice particle after impact.

The aforementioned studies dealt with fully frozen ice particles. In an aircraft engine, partially melted ice particles can be generated by the warm compressor airflow. It was not known to what extent the impact dynamics might be influenced, e.g. in dependence of the liquid to ice ratio of a particle. In 2014, Palacios et al.[44] investigated the impact process of fully frozen and partially melted spherical ice particles with diameters between 0.4 and 0.9 mm. The impact velocities varied between 140 and 309 m/s, and the impact angle was set to 30°, 45°, or 60°. To generate partially melted ice particles, an oxygen/acetylene flame was positioned along the ice particle trajectory. The residual on the target was quantified using the ratio of the residual's area and the projected area of the initial spherical ice particle. The authors concluded that the smaller the impact angle was, the larger the residual became. Moreover, at impact angles of 30° and 45°, the size of the residual increased with increasing impact velocity. More systematic studies are required, however, for future development of physical models.

To date, it is also not known if available hail impact models can be applied to the impact process of small ice particles, e.g. models for threshold velocities and post-impact particle size and velocity distributions. The influence on the fracture mechanics of the structure of small (natural) ice particles, which consist of few or even single crystals in contrast to the structure of hail particles, which have a polycrystalline structure, is not known and the factors controlling bouncing and fragmentation are not necessarily the same or have the same magnitude. For this reason, there is a need for experimental data from small ice particle impacts to allow the development of adequate (semi-empirical) impact models which describe the aforementioned aspects.

2.2 Ice Particle Melting in Forced Convection

The melting of an ice particle in an airflow is a multiphase flow problem. It is mainly determined by the flow temperature, velocity, and relative humidity as well as the particle's shape and mass. For example, a low relative humidity of the flow leads to strong evaporative cooling which increases the melting time. The particle's shape determines the surface area which is subject to heat transfer by convection. In terms of ice crystal icing, the particles' melt ratios and sizes upon impact are relevant factors which determine ice accretion.

In the past decades, only a few studies were carried out to improve the understanding of the melting process of individual ice particles in an airflow. Rasmussen et al.[45,46,47] investigated the melting process and meltwater shedding of spherical ice particles with diameters less than

1 mm and larger than 3 mm in a vertical wind tunnel at terminal fall velocity. For the smaller particles, the temperature of the airflow was increased at constant warming rates (between 2 and 5 °C/min) starting from approx. -10 °C. The relative humidity RH was between 25 % and 95 %. Rasmussen et al. concluded that - compared to calculations accounting for concentric melting and pure diffusive heat transfer - the melting time of small spherical ice particles with diameters less than 1 mm was approx. 10 % shorter due to internal re-circulation in the meltwater around the particle and the observed eccentric location of the ice core within the meltwater. The eccentric location was caused by the different bulk densities of ice and water. Possible random sailing motions of the free-falling small spherical ice particles resulted in increased unsteady heat transfer. An increased surface area due to surface irregularities further reduced the melting time. In their investigations, the experimental error accounted for a maximum of 15 % difference between experimental and calculated melting times. For the larger spherical ice particles (diameter > 3 mm), the air temperature was constant at approx. 20 °C and RH = 40 %. Tumbling motions of the particles were suppressed and other movements (spinning, etc.) were restricted by suspending and fixing the spherical ice particles with a nylon fibre. The measured melting rates agreed with calculations assuming the meltwater was at 0 °C.

The typical modelling of the heat and mass transfer taking place at a particle's outer boundary in forced convection is shown in the following. The modelling equations can be used for different materials and flows by adapting the thermodynamic properties. Below, the case of an ice particle in an airflow is described.

The heat transfer equation for an ice particle in forced convection is:

$$\frac{\partial H_P}{\partial t} = \dot{Q}_{con} + \dot{Q}_{rad} + \dot{Q}_{latent}, \tag{2-5}$$

where $\frac{\partial H_P}{\partial t}$ is the change of the ice particle's enthalpy with respect to time t, $\dot{Q}_{con}$ is the rate of convective heat transfer, $\dot{Q}_{rad}$ is the rate of radiative heat transfer, and $\dot{Q}_{latent}$ is the rate of latent heat transfer due to phase change.

Equation (2-5) is a balance between the change of the internal energy of the ice particle and the heat transfer rates across its boundary and due to phase change. The terms in Eq. (2-5) can be substituted as follows:

$$\frac{\partial H_P}{\partial t} = m_p \, c_p \, \frac{dT_{p,m}}{dt}, \tag{2-6}$$

where m_p is the ice particle mass, c_p is the specific heat capacity of the ice particle, and $T_{p,m}$ is the mean ice particle temperature.

$$\dot{Q}_{con} = A_p \, h_m \, (T_a - T_{p,s}), \tag{2-7}$$

where A_p is the surface area of the ice particle, h_m is the mean convective heat transfer coefficient, T_a is the air temperature, and $T_{p,s}$ is the mean surface temperature of the ice particle.

$$\dot{Q}_{rad} = A_p \sigma \varepsilon_p (T_{env}^4 - T_{p,s}^4), \tag{2-8}$$

where σ is the Stefan-Boltzmann constant ($\sigma \approx 5.67$ E-8 $\mathrm{Wm^{-2}\,K^{-4}}$), ε_p is the emissivity of the particle ($\varepsilon_p \approx 1$ for ice and water) and T_{env} is the temperature of the environment.

$$\dot{Q}_{latent} = \dot{m}_p L, \tag{2-9}$$

where $\dot{m}_p$ is the change of the ice particle mass due to phase change and L is the latent heat. The rate of radiative heat transfer is significant only for very high temperatures or large temperature differences between the particle and the environment. For this reason, the term $\dot{Q}_{rad}$ can be neglected for melting experiments with ice particle and environment temperatures close to 0 °C.

The mean convective heat transfer coefficient h_m is derived from the definition of the Nusselt number:

$$\mathrm{Nu}_p = \frac{h_m \, l_p}{k_a}, \tag{2-10}$$

where Nu_p is the ice particle's Nusselt number, l_p is the characteristic length of the ice particle, and k_a is the thermal conductivity of air.

Typical Nusselt correlations for objects (e.g. spheres, cubes etc.) under forced convection have the following form:

$$\mathrm{Nu}_p = \mathrm{Nu}_0 + a_1 \mathrm{Re}_p^{a_2} \mathrm{Pr}^{a_3}, \tag{2-11}$$

where Nu_0 is the lower asymptotic value of the Nusselt number for natural convection only, a_1, a_2, and a_3 are constants, Re_p is the ice particle's Reynolds number, and Pr is the Prandtl number of air. Nusselt correlations for non-spherical particles are rarely found in literature[48,49]. In 2012, Richter & Nikrityuk[50] numerically derived a Nusselt correlation for cubes and ellipsoids for $10 < \mathrm{Re} < 250$ which depends on the sphericity Φ and crosswise sphericity $\Phi_\perp$ of the particle:

$$\mathrm{Nu}_p = 1.76 + 0.55\Phi \mathrm{Re}_p^{1/2} \mathrm{Pr}^{1/3} \Phi_\perp^{0.075} + 0.014 \mathrm{Re}_p^{2/3} \mathrm{Pr}^{1/3} \left(\frac{\Phi}{\Phi_\perp}\right)^{7.2}. \tag{2-12}$$

The sphericity Φ of a particle is defined as the ratio of the surface area of a sphere (with equivalent volume as the particle) to the actual surface area of the particle:

$$\Phi = \frac{\pi^{\frac{1}{3}} (6V)^{\frac{2}{3}}}{A_p}, \tag{2-13}$$

where $0 < \Phi \leq 1$ and V is the particle volume. For $\Phi = 1$, the particle is a sphere.

The crosswise sphericity $\Phi_\perp$ is derived from the particle's projected area $A_\perp$:

$$\Phi_\perp = \frac{\pi d_p^2}{4A_\perp}, \tag{2-14}$$

where d_p is the volume-equivalent sphere diameter. d_p of a non-spherical particle is the diameter of a sphere which has the same volume as the particle:

$$d_p = \left(\frac{6}{\pi} V\right)^{1/3}. \tag{2-15}$$

The Reynolds number of a particle is the ratio of momentum forces to viscous forces and is defined as:

$$\mathrm{Re}_p = \frac{v_a\, l_p}{\nu_a}, \tag{2-16}$$

where v_a is the airflow velocity and ν_a is the kinematic viscosity of air. The Reynolds number is important for the characterization of the different flow regimes (e.g. laminar and turbulent regimes).

The Prandtl number is the ratio of momentum diffusivity (kinematic viscosity) to thermal diffusivity. It is also a measure for the thickness ratio of the velocity boundary layer to the thermal boundary layer. For air, it is defined as:

$$\mathrm{Pr}_a = \frac{\nu_a}{\alpha_a}, \tag{2-17}$$

where α_a is the thermal diffusivity of air defined as:

$$\alpha_a = \frac{k_a}{\rho_a c_{p,a}}, \tag{2-18}$$

where ρ_a is the air density and $c_{p,a}$ is the heat capacity of air.

Assuming that mass transfer into or from the airflow (e.g. sublimation or deposition) occurs at the ice particle's surface, the mass transfer rate is:

$$\dot{m}_{sub} = A_p\, k_c\, \rho_{mix}\left[y_{v,s}\left(T_{p,s}, p_{a,s}\right) - y_{v,a}(T_a, p_a)\right], \tag{2-19}$$

where $\dot{m}_{sub}$ is the sublimation (or deposition) rate, k_c is the mass transfer coefficient, ρ_{mix} is the density of the vapour-air mixture ($\rho_{mix} \approx \rho_a$ for small mass transfer rates), $y_{v,s}$ is the vapour mass fraction at the ice particle surface, and $y_{v,a}$ is the airflow's vapour mass fraction. If $y_{v,s} > y_{v,a}$, sublimation occurs. The mass transfer coefficient is derived from the definition of the Sherwood number:

$$\mathrm{Sh}_p = \frac{k_c\, l_p}{D_{v,a}}, \tag{2-20}$$

where Sh_p is the ice particle's Sherwood number and $D_{v,a}$ is the water vapour diffusivity in air. Due to the analogy between heat and mass transfer, Sherwood correlations for forced convection can be derived from the corresponding Nusselt correlations substituting the Prandtl number with the Schmidt number:

$$\mathrm{Sh}_p = \mathrm{Sh}_0 + a_1 \mathrm{Re}_p^{a_2} \mathrm{Sc}^{a_3}, \tag{2-21}$$

where Sh_0 is the lower asymptotic value of the Sherwood number for natural convection only, a_1, a_2, and a_3 are constants, and Sc is the Schmidt number.

The Schmidt number is the ratio of momentum diffusivity (kinematic viscosity) and mass diffusivity:

$$\mathrm{Sc} = \frac{\nu_a}{D_{v,a}}. \tag{2-22}$$

It describes the ratio of the velocity boundary layer thickness to the mass-transfer boundary layer thickness.

The vapour mass fraction at the ice particle surface is calculated as follows:

$$y_{v,s} = \frac{m_{v,s}}{m_{a,s} + m_{v,s}} \approx \frac{m_{v,s}}{m_{a,s}} = \frac{M_v n_{v,s}}{M_a n_{a,s}} = \frac{M_v p_{v,s}}{M_a p_{a,s}}, \tag{2-23}$$

where $m_{v,s}$ is the mass of the vapour at the surface, $m_{a,s}$ is the mass of air at the surface, M_v is the molar mass of water vapour ($M_v \approx 18\,\mathrm{g/mol}$), M_a is the molar mass of air ($M_a \approx 29\,\mathrm{g/mol}$), $n_{v,s}$ and $n_{a,s}$ are the molar amounts of vapour and air at the surface, respectively, and $p_{v,s}$ and $p_{a,s}$ are the partial pressures of vapour and air at the surface, respectively. If $m_{v,s} \ll m_{a,s} \rightarrow m_{a,s} + m_{v,s} \approx m_{a,s}$. At the surface, $p_{v,s}$ is equal to the saturation vapour pressure $p_{v,s}^{sat}$ which depends on the state of the surface (water or ice), and on airflow temperature. Several correlations for the calculation of the saturation vapour pressure exist, e.g. the one from Buck[51].

The calculation of the vapour mass fraction of the airflow is analogous:

$$y_{v,a} \approx \frac{M_v p_{v,a}}{M_a p_{a,a}}, \tag{2-24}$$

where $p_{v,a}$ and $p_{a,a}$ are the partial pressures of vapour and air in the airflow.

The partial pressure of vapour in the airflow can be calculated with:

$$p_{v,a} = \mathrm{RH}\, p_{v,a}^{sat}, \tag{2-25}$$

where RH is the relative humidity and $p_{v,a}^{sat}$ is the saturation vapour pressure of the airflow.

Theoretical models considering heat transfer between the ice particle and the airflow (and within the melting ice particle) as well as changes of the solid, liquid, and gas phase during melting of spherical ice particles were developed by Mason[52] and Wright et al.[53]. In 1956, Mason investigated the melting of spherical hailstones falling in the atmosphere. He assumed that for hailstones with diameters smaller than 3 mm no shedding of the meltwater, which was uniformly distributed around the ice core, occurred. Mason also assumed a uniform temperature (0 °C) of the ice core and the presence of evaporation and condensation during melting. The meltwater temperature could differ from the ice core temperature. The heat transfer through the liquid layer was purely conductive (i.e. no circulation of the meltwater). His theoretical investigations allowed - for the first time - the prediction of the state of falling hailstones at certain altitudes below the freezing level. Wright et al. published a theoretical model for mixed-phase icing in a jet engine (including a melting model being very similar to Mason's model) which was implemented in the software GlennICE in 2011. The authors assumed the film temperature to be equal to the melting temperature throughout melting. No validation was shown in their paper. Recently, in 2015, Currie et al.[54] expanded a melting model for spherical ice particles to non-spherical ice particles by introducing a correction based on experimental results from Hauk et al.[55]. The correction accounts for the increased surface area of non-spherical particles in comparison to spherical particles with the same volume-equivalent sphere diameter and allows for a more precise calculation of the melting time. Kintea et al.[56] developed a theoretical model which accounts for the main physical phenomena associated with melting of a non-spherical particle (i.e. collection of liquid at the particle midsection, appearance of sharp cusps at the particle tips, and smoothing of the particle surface). The theoretical predictions agreed well with the experimental data for melting ice particles.

In several studies, the melting of non-spherical *snowflakes* was investigated under various conditions. Matsuo and Sasyo[57] studied the melting of fresh snowflakes with maximum diameters ranging from 3.8 to 8.6 mm which were fixed at a nylon fibre. The airstream had a constant velocity of 1 m/s, a constant temperature of 5.5 °C and RH = 65 %. The authors

observed that capillary action led to significant collection of meltwater in the core part of the snowflake instead of the accumulation of meltwater on the branches' surfaces. Moreover, Matsuo and Sasyo[58] developed a microphysical model for spherical snowflakes and showed that the RH of the flow had a significant effect on the melting rate. They showed that freely falling snowflakes in the atmosphere in sub-saturated air first experienced melting well below the freezing altitude due to the effect of evaporative cooling. Fukuta et al.[59] investigated the melting process of freely suspended natural snowflakes in a vertical wind tunnel at terminal velocity (typically several m/s) and at fixed temperatures of 2, 3, and 4 °C. The maximum diameter ranged from hundreds of microns up to several millimetres and RH was either 90 or 100 %. The authors introduced a model for the melting of snowflakes, where a snowflake was represented by several small spherical ice particles arranged in fixed positions. They assumed that no mass transfer took place between snowflake and environment (i.e. a saturated atmospheric environment was assumed). Melting could occur at all small spherical ice particles and the outer spheres were allowed to fully melt leading to meltwater collection around the remaining (inner) spheres. Thus, it was possible to account for mixed-phase snowflakes which led to a better understanding of the level of radar reflectivity of melting snowflakes. Mitra et al.[60] investigated the melting of natural and laboratory made snowflakes under free fall conditions at RH = 90 %. The flow temperature was raised during the melting process at a rate of 1.5 °C/min, which is similar to the one experienced by snowflakes freely falling in the atmosphere. The flakes had diameters of approx. 10 mm and melted before the air temperature reached 5 °C. The authors developed a theoretical heat transfer model for snowflakes made of dendritic snow crystals by approximating the particle's shape with an oblate spheroid. They assumed that during the melting process the temperature of the melting particle remained at 0 °C. The calculated fall distances needed for complete melting agreed well with radar observations of the atmosphere. Due to differences in the assumed particle shape, ventilation coefficient, and drag coefficient, the fall distances were about 100 m longer than predicted by Matsuo and Sasyo[58].

Theoretical and experimental investigations of the melting process of individual non-spherical ice particles, whose shapes are similar to the ones which can be found in the vicinity of deep convective clouds (Figure 1-3), are scarce. Nusselt correlations which can be (easily) applied to particles with arbitrary shapes are rare and often not validated experimentally. Moreover, melting of ice particles in a jet engine compressor may occur at airflow temperatures higher than the ones experienced by snowflakes and ice particles falling in the atmosphere (close to 0 °C). For this reason, the melting process of ice particles was further investigated in this work

at different flow velocities ($v \leq 1.75$ m/s), flow temperatures ($T \leq 30$ °C) and RH ranging from ~4 to ~74 % (at 1 bar and 20 °C). To calculate the theoretical melting times, heat and mass transfer correlations which take the non-spherical particle shape into account were validated and applied.

2.3 (Ice) Particle Impact onto a Liquid Film

The collision of particles onto wetted surfaces or of wetted particles onto each other has been and is still investigated. A better understanding of these processes is necessary for the modelling of particle granulation in fluidized beds, material deposition on walls during spray drying, or deposition of ice particles on surfaces covered with a water film. The influence of the thin liquid film on particle dynamics needs to be taken into account, particularly, if the particle's inertia force is comparable to or smaller than the capillary or viscous forces. This tends to be the case for low particle density, mass, and velocity as well as for relatively high viscosity and surface tension of the thin liquid film. Particle impact onto a thin liquid film normally has three possible outcomes: *sticking*, *bouncing*, or *fragmentation* with (partial) sticking of the fragments. Choosing a specific particle-film-wall combination, these outcomes are typically determined by the impact velocity, particle size, and film thickness. Up to date, universal models which predict the impact of particles onto a liquid film and which can be applied to arbitrary particle-film-wall combinations do not exist. In such a universal model, e.g. the effect of surface roughness on wettability would need to be taken into account which is currently under investigation[61]. Current models usually have several limitations (i.e. simplifying assumptions) due to the high complexity of the problem. For this reason, most studies in the past focused on specific particle-film-wall combinations to derive typical scaling relations.

Antonyuk et al.[62,63] conducted free-fall normal impact experiments with different particles on wetted walls. They studied the influence of viscosity, impact velocity, and liquid film height on energy dissipation. Glass spheres ($2.5 < D < 2.8$ mm), Al_2O_3 granules (median diameter of 1.75 mm), and agglomerates of maltodextrin ($2.0 < D < 3.0$ mm) were used. Moreover, the viscosity of the liquid was varied between 1 and 300 mPa·s and the thickness of the liquid film was in the range from 40 to 1000 µm. Impact velocities were 1.0 and 2.36 m/s. The target materials were steel or glass. Main conclusions were that the restitution coefficient of Al_2O_3 granules and glass spheres impacting onto a thin liquid film decreased with decreasing impact velocity. Moreover, with increasing viscosity and film thickness, energy dissipation increased.

Antonyuk et al. also developed a comprehensive model to predict the impact process. The theoretical calculations were in good agreement with the experiments.

The conclusions from Antonyuk et al. were in agreement with the findings of Gollwitzer et al.[64] who used glass spheres ($2.8 < D < 10.0$ mm) and a glass target with a thin liquid film ($75\ \mu m < H < 1$ mm). Viscosity and impact velocity ranged from 1 to 48 mPa·s and from 0.3 to 1.7 m/s, respectively. They concluded that the impact velocity dependence of the restitution coefficient could be characterized by two parameters e_{inf} and E_c, where e_{inf} is the saturated value of the restitution coefficient and E_c is the critical kinetic energy below which no rebound is possible. They successfully scaled the collected experimental data using the Stokes number:

$$\mathrm{Stk} = \frac{\rho_P D U_0}{9\eta} \tag{2-26}$$

and Reynolds number:

$$\mathrm{Re} = \frac{\rho_l H U_0}{\eta}, \tag{2-27}$$

where ρ_P and ρ_l are the densities of the particle and liquid, and η is the dynamic viscosity of the liquid.

Kantak et al.[65] investigated dry and wet collisions of stainless steel and Teflon spheres (D = 6.4 and 9.5 mm) onto a quartz plate. In the case of wet impacts, the plate was covered with a liquid layer of thickness 30 µm and viscosity 0.05 Pa·s. A pendulum and a special apparatus for low-gravity environments were used to achieve low impact velocities ranging from 0.02 to 0.3 m/s. Data from both experiments agreed well with each other. They observed that with increasing impact velocity the dry restitution coefficient decreased. For higher impact velocities up to 3 m/s, a free-fall technique was used. In this case, the layer thickness varied between 80 and 150 µm and two viscosity values, 0.975 and 12.4 Pa·s, were chosen. The spheres were the same as in the low-velocity case. The authors showed that the equation:

$$\frac{e_{wet}}{e_{dry}} = 1 - \frac{\mathrm{Stk}_c}{\mathrm{Stk}} \tag{2-28}$$

can be used to describe the low and high-velocity impacts investigated in their study. In Eq. (2-28), e_{wet} and e_{dry} are the wet and dry restitution coefficients, and Stk_c is the critical Stokes number below which sticking of the particle occurs.

Equation (2-28) was already applied in earlier investigations[66,67] on normal and oblique impacts of spheres onto wetted walls. It was shown that this equation also holds for the description of the restitution coefficient of the normal component of the impact velocity in the case of oblique impacts.

A typical normal impact of a hydrophilic stainless steel sphere onto a water film is shown[68] in Figure 2-3. Water film thickness and temperature, sphere diameter, and initial velocity were 5 mm and 20 °C, 20 mm, and 3.1 m/s, respectively.

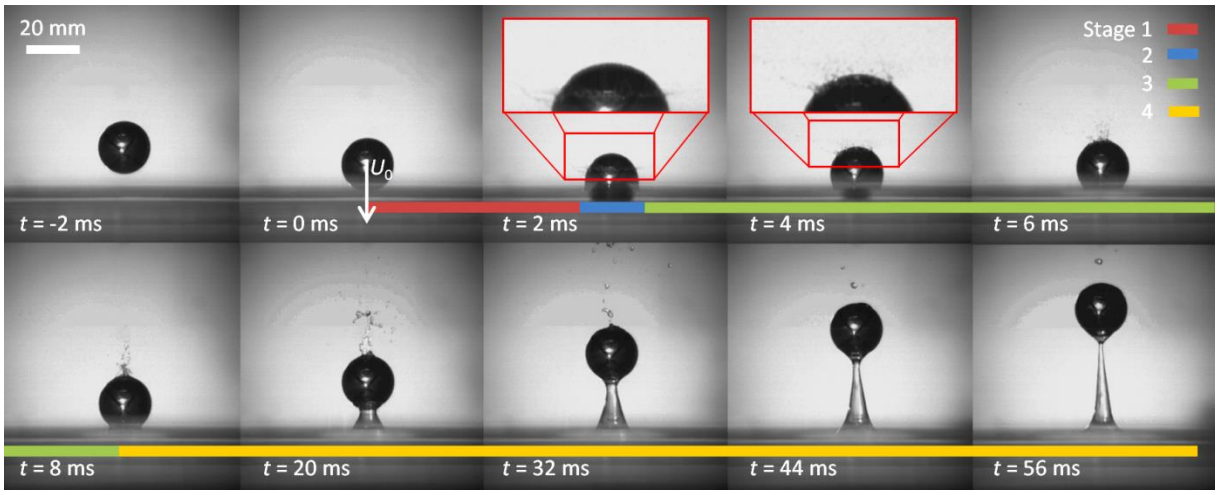

Figure 2-3. Normal impact of a stainless steel sphere onto a water film with thickness 5 mm and temperature 20 °C. Sphere diameter and initial velocity were 20 mm and 3.1 m/s, respectively. The 4 different stages are marked.

According to Antonyuk et al.[62], the impact can be divided into 4 stages, shown in Figure 2-3. At the beginning of Stage 1 ($t \approx 0$ ms), the particle established first contact with the water film. The velocity at that particular moment is defined as impact velocity U_0. During Stage 1, kinetic energy of the particle was partially absorbed by the film and dissipated as viscous and capillary forces. A thin water film wetted the surface of the sphere moving upwards along the surface starting at the sphere's bottom. During its rise, small droplets were released at the position of the moving three-phase line. In Stage 2 ($t \approx 2$ ms), which lasted only fractions of a millisecond, the particle-wall interaction took place and part of the kinetic energy was dissipated due to elastoplastic deformations of the particle and the wall. The rebound of the particle occurred in Stage 3 ($2 \lesssim t \lesssim 8$ ms), where again viscous and capillary forces mainly

contributed to energy dissipation. The film wrapping the sphere met at the top of the sphere and formed a small jet, breaking up into several droplets after few ms. This small jet was first observed by Worthington [69] and was also described by Duez et al. [70] and McKown [71], who investigated, amongst others, the impact of solid spheres onto deep water pools. In Stage 4 ($8 \lesssim t \lesssim 56$ ms), a liquid bridge formed between the bottom of the sphere and the liquid film, which was elongated by the upward moving sphere. At the moment of breakup of the liquid bridge, the sphere was fully covered with a thin liquid water film. The breakup of the liquid bridge marks the end of Stage 4. Energy dissipation due to the buoyancy force and an increased mass of the sphere due to wetting with water during impact are often neglected[72]. The different sources of energy dissipation were described in detail by Antonyuk et al.[62].

To the author's knowledge, no experimental investigations exist which focused on ice particle impact onto a liquid water film. Moreover, current models do not account for aspects which could be important in this special case: e.g. the surface roughness of ice, potential melting/freezing of the ice/water during liquid film contact, or particle fragmentation upon impact. For this reason, as a first step, there is the need to build a suitable test apparatus to allow the collection of impact data of fully frozen spherical ice particles impacting onto a thin water film. Subsequently, the impact of more and more complex ice particle shapes could be investigated to better predict ice accretion in glaciated icing conditions.

2.4 Ice Accretion in Mixed-Phase and Glaciated Icing Conditions

Ice accretion on cold and hot surfaces in mixed-phase and glaciated icing conditions is a complex process. It may depend on LWC and IWC, ice particle size and shape, target temperature and shape, airflow pressure, velocity, temperature and RH. It may also depend on ice particle temperature, surface roughness, and wettability of the target as well as on further effects such as erosion and sticking. Up to 2006, when Mason et al. published "The Ice Particle Threat to Engines in Flight"[9], publications focusing on the investigation of ice accretion in mixed-phase and glaciated icing conditions have been rare and adequate test facilities were very limited.

Before 2006, Al-Khalil et al.[73] conducted probably the most important experimental ice accretion study in the field of ICI whose results are frequently used in present times by the ice crystal icing community. In 2002, the authors investigated the influence of mixed-phase and glaciated icing conditions on thermal ice protection system performance and the relevant physics of ice accretion in the Cox & Company Icing Wind Tunnel. A NACA 0012 airfoil with

14 heater zones and a zero angle of attack was used in the test section. Air velocity was 53 m/s and air temperature was mostly either -17.8 °C or -11.1 °C. Supercooled, glaciated, or mixed-phase icing conditions were generated. Independent from LWC and surface temperature, (partial) rebound of ice particles from the airfoil was observed in mixed-phase and glaciated icing conditions. In glaciated icing conditions, a thin layer of frost, presumably consisting of ice particle residuals, was observed on the unheated surface. The frost layer did not grow further with time. They emphasized that ice particles (at least partially) stuck to heated surfaces under glaciated icing conditions since liquid water was observed on the heated surfaces. Due to the restrictions of the imaging equipment, particle rebound and splashing could not be quantified. They observed that in mixed-phase conditions at an air temperature of -17.8 °C ice particles did not significantly influence the amount of accreted ice except for "the erosion of the feather-like ice growths close to the impingement limits". In mixed-phase conditions at -5.6 °C, the increase of the IWC from 0.0 to 0.7 g/m³ (LWC was kept constant at 0.7 g/m³) led to a decrease of the amount of accreted ice. Al-Khalil et al. assumed that this decrease was caused by erosion and splashing of the liquid layer provoked by ice particle impact.

Since the work of Mason et al.[9] in 2006, the awareness of the significance of ICI increased enormously throughout the aircraft icing community and several theoretical and experimental studies have been conducted in this field. Many of the recent publicly available experimental studies were conducted by NASA and NRC, who developed an icing test facility for glaciated icing and mixed-phase icing conditions.

In 2007, MacLeod[74] did exploratory tests with a cold and heated flat plate in glaciated icing conditions in NRC's Gas Turbine Laboratory in Ottawa. Airflow velocity was varied from 80 m/s to 150 m/s and the ambient temperatures were in the range from -5 °C to 12 °C. IWC was between 1.0 and 5.0 g/m³ and plate temperature was either equivalent to the ambient temperature in the cold case or, in the heated case, up to 30 °C. In the case of the cold plate, no ice accretion was observed. In the heated case, rapid ice accretion on the leading faces of small metal blocks attached to the flat plate was observed. A decrease of the surface temperature was measured simultaneously to the activation of the ice particle stream. An increase of IWC led to a faster buildup of ice. During ice buildup, he could observe water streaming away from the buildup location and concluded that the ice is growing faster than being melted in the ice – metal interface and that the ice was not adhered to the surface. At the end of an ice accretion cycle, ice shedding due to aerodynamic drag was observed and the cycle started again.

In 2011, Mason et al.[22] published a study in which mixed-phase and glaciated icing conditions in an S-shaped duct containing an airfoil mounted to a temperature-controlled endwall were simulated in NRC's Research Altitude Test Facility (RATFac). The geometry represented the transition duct between the low and high pressure compressor of a typical aircraft engine with an engine strut (simulated by the airfoil) connecting the inner and outer surfaces of the duct. At subfreezing airflow (only IWC; no LWC) and surface temperatures, no ice accretion occurred. At subfreezing airflow (only IWC; no LWC) and above freezing endwall temperatures, a small amount of ice accreted at the stagnation area where airfoil and endwall met. Several tests were done with above freezing airflow temperatures which led to partial melting of the ingested ice particles before impact. In these mixed-phase conditions, ice accretion was most significant on surfaces below freezing. Moreover, they concluded that icing severity might depend on the ratio of LWC to TWC and that an optimum icing regime might exist (Currie et al.[75] quantified this dependence for a certain test case shown in Figure 2-4 in 2014). The left boundary (low LWC/TWC ratio) of the optimum icing regime might be traced back to a loss of sticking capability of the partially melted ice particles due to a lack of the liquid phase. The right boundary (high LWC/TWC ratio) might be determined by too much liquid leading to "continuous shedding" instead of accretion and leading to a lack of ice particles with temperatures below freezing which could cool down the surface to freezing upon impact. Within the optimum icing regime, the rate of ice accretion increased with increasing IWC.

In 2011 and 2012, Struk et al.[76] and Currie et al.[77] published experimental studies conducted in RATFac to investigate the fundamental physics of ice accretion caused by mixed-phase and glaciated icing conditions. For the icing tests, an unheated double wedged airfoil was used. Its shape allowed some phenomena to occur which are similar to the ones found in a jet engine compressor, e.g. high incidence ice particle impacts onto a stator blade or guide vane. Most of the tests were done at $M = 0.2, 0.25, 0.3$ and total pressures of 44.8 kPa and 93.0 kPa. Total temperatures ranged from 5 °C to 23 °C. LWC and IWC ranged up to 5 and 20 g/m³, respectively. They concluded that the accretion process can be correlated with the wet bulb temperature T_{wb}. The wet bulb temperature depends on air temperature, pressure, and moisture content of the flow. It was calculated under dry conditions, i.e. without the injection of liquid water or ice particles. According to Currie et al., "*the wet bulb temperature is the temperature of a wet adiabatic surface in an airflow. […] T_{wb} is obtained by equating the rate of heat transfer to a surface by convection to the heat loss by evaporation, assuming any water added to replace that lost by evaporation, and therefore keep the surface wet, is at T_{wb}. […] The*

importance of T_{wb} is that $T_{wb} = 0$ °C demarcates conditions where (partial) freezing of water on an adiabatic surface is possible from those where it is not, regardless of whether the surface is that of an obstacle or ice crystal in the freestream.". With respect to ICI, T_{wb} determines the degree of melting (i.e. the ratio of LWC to IWC) of the ice particles in an airflow for $T_{wb} > 0$ °C. With increasing T_{wb} the ratio of LWC to IWC increases. T_{wb} also determines if freezing ($T_{wb} < 0$ °C) or melting ($T_{wb} > 0$ °C) of a mixed-phase ice accretion is promoted. Under the assumption of constant temperature and moisture content of the flow, a pressure drop results in a lower wet bulb temperature due to enhanced evaporative cooling. A derivation of T_{wb} is shown in Currie et al.[77]. For $T_{wb} < 0$ °C (in the optimum icing regime suggested by Mason et al.[22]), the accreted ice was well-adhered. However, for high LWC/TWC ratios and for $T_{wb} < 0$ °C, poorly adhered ice accretions were possible. For $T_{wb} > 0$ °C, ice accumulations were small at low IWC (7 g/m³) and were disproportionately higher for high IWC (17 g/m³). These large ice accumulations did not adhere well to the surface and were subject to deformation before shedding. Shedding occurred regularly.

In 2012 and 2013, Knezevici et al.[78,79] investigated the effect of ice particle size on ice accretion in mixed-phase icing conditions. The experiments were conducted in RATFac and a test article simulating the bleed slot of the outer casing of a jet engine compressor was used. Total pressure, Mach number, and total temperature of the airflow were 44.8 kPa, 0.25, and ~8 °C, respectively. Particle size distribution significantly affected the ice accretion rate, even if aerodynamic conditions, the LWC/TWC ratio, and TWC were matched. This observation was valid for wet bulb temperatures below and above freezing and can be traced back to different erosion, splashing, and particle bouncing behaviour. The authors believed that the right tails of the particle size distributions (i.e. the larger particles) were responsible for the different accretion rates and needed to be accounted for to define the ice crystal icing phenomenon. Larger particles/MMDs had the tendency to reduce ice accretion rates.

In 2013, Currie et al.[80] found that the key parameter which must be matched to obtain similar ice accretions in different simulated altitudes (i.e. pressures) was the LWC/TWC ratio (melt ratio). To set a certain melt ratio, the wet bulb temperature was varied. Beyond its effect on the LWC/TWC ratio, the influence of T_{wb} was observed to be negligible on ice accretion. Since evaporative cooling is stronger at lower pressures, the total temperature was increased at lower pressures to obtain melt ratios similar to the ones at higher pressures. The LWC/TWC ratio had a significant influence on accretion size (i.e. volume). The largest accretions occurred for melt ratios between 10 and 25 %. At constant melt ratios, the accretion rate scaled in direct proportion to TWC in the early growth phase. Moreover, the accretion steady-

state size scaled directly with TWC, which is currently subject to further investigations. Tests were conducted at M = 0.25. Total pressures were 34.5 kPa and 69 kPa and total air temperatures at these pressures were 15 °C and 8 °C, respectively. Wet bulb temperatures were varied from -2 °C to +6 °C. The test article was an axisymmetric, hemispherical nose with a conical afterbody. A semi-empirical ice accretion model was developed which successfully predicted the accretions of two different runs.

In 2014, Currie et al.[75] conducted an experimental study to develop an ice accretion model based on sticking efficiency. Sticking efficiency was defined as the ratio of the mixed-phase impinging mass flux remaining on the surface to the total impinging mass flux. Three different test articles were used: two axisymmetric models with either a hemispherical or conical forebody, and one crowned cylinder. In contrast to classical icing models (e.g. for icing caused by supercooled droplets), heat transfer and phase change were not considered. Sticking efficiency was strongly correlated with the melt ratio and was highest in the optimum icing regime ranging from ~10 to ~20 % melt ratio. In the case of the axisymmetric spherical test article, Figure 2-4 was suggested showing icing severity vs. melt ratio.

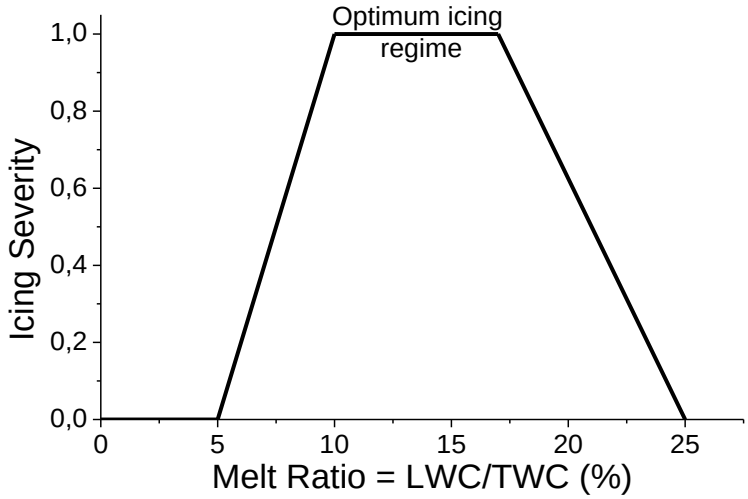

Figure 2-4. Icing severity (0 = lowest severity; 1 = highest severity) vs. melt ratio as suggested by Currie et al.[75] for an axisymmetric test article.

Currie et al. showed that sticking efficiencies are independent of TWC, Mach number, and particle size for normal impacts. However, for oblique impacts, sticking efficiencies strongly depend on these quantities. An erosion-based semi-empirical model was developed and showed good agreement with most of the experimental results.

In 2015, Struk et al.[81] published experimental test results to help the icing community to model ice accretion due to ICI. The tests were conducted at RATFac. A NACA 0012 and the aforementioned wedge type airfoil were used. Ice accretion growth and surface temperature evolutions were presented.

Several ice accretion models for mixed-phase icing have been developed recently[54,82–88]. Many of these models are founded on the model from Messinger[89]. Messinger analysed the heat and mass transfers taking place during icing of an unheated, adiabatic surface caused by supercooled water droplets in an airflow. His goal was the derivation of the steady-state temperature of the surface. The accreting ice layer was assumed to be isothermal. In the case of rime ice conditions, i.e. all of the impinging water freezes, the relevant heat (red dashed arrows) and mass (black solid arrows) fluxes to and from the accreting ice layer are shown in Figure 2-5.

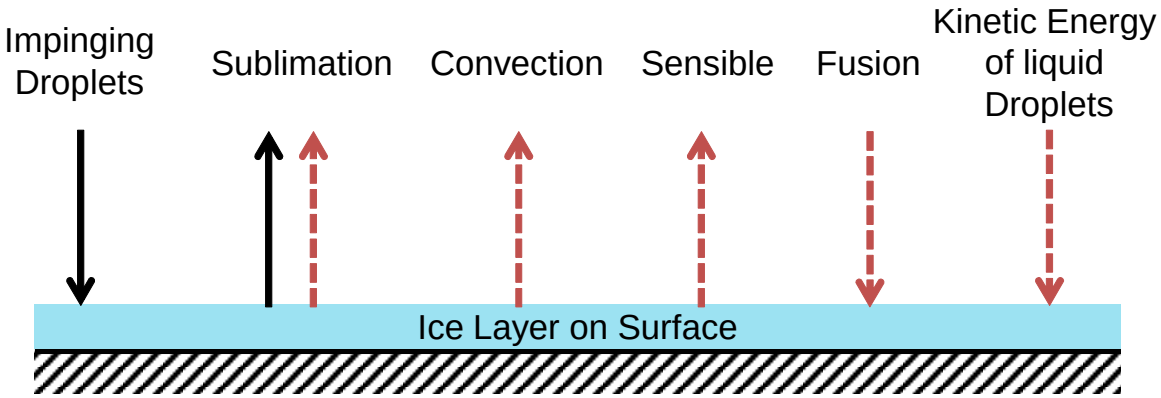

Figure 2-5. Typical heat (red dashed arrows) and mass (black solid arrows) fluxes in rime ice conditions during icing caused by supercooled droplets according to Messinger[89].

All of the impinging droplets freeze on the surface and build the ice layer. Mass is transferred into the environment due to sublimation only (no runback; no shedding). Under the assumption that the airflow temperature is smaller than the temperature of the ice layer and that the vapour mass concentration in the flow is smaller than at the ice layer's surface, heat is lost (from the ice layer's point of view) due to sublimation, convection[††], and due to heating of the impinging droplets (sensible heat). During solidification of the supercooled droplets, the heat of fusion is added to the ice layer. Upon droplet impact, the kinetic energy of the droplets is transformed into heat and is also added to the ice layer. The last term as well as

[††]In this term, the recovery temperature of the airflow at the surface needs to be considered to account for viscous heating in the boundary layer.

radiation (not shown in Figure 2-5) are often not considered due to their negligible sizes. The definitions of the different terms are described in detail in Messinger's work.

As described in detail, several experimental and theoretical studies have been conducted to investigate ice accretion in mixed-phase and glaciated icing conditions, recently. NRC and NASA have conducted several experimental studies showing that the LWC to TWC ratio determines icing severity and that it is likely a suitable parameter for altitude scaling. They also showed the influence of the wet bulb temperature on mixed-phase ice accretions. Based on the Messinger model, several models were developed which describe the ice accretion process in mixed-phase icing conditions.

In the future, more studies will have to be conducted to understand ice accretion in mixed-phase and glaciated icing conditions on different test articles and in different thermodynamic conditions. For example, the roles of the effects of particle sticking as well as particle erosion are not yet well understood. Moreover, the initial mechanisms leading to ice accretion on a heated surface in glaciated and mixed-phase icing conditions have not been investigated in detail yet.

3 Exploratory Ice Accretion Experiments on a Warm Surface

Several experimental and numerical studies, including model developments, have been conducted in the past to improve the understanding of ice accretion in glaciated and mixed-phase icing conditions. Knowledge and observations of the initial mechanisms which lead to ICI on a microscale level are still very limited. Better understanding of these mechanisms could contribute to conceptions of how to prevent or reduce ICI. For this reason, exploratory experiments have been conducted which investigate the initial instants of ice accretion on a warm surface in detail.

3.1 Test Apparatus

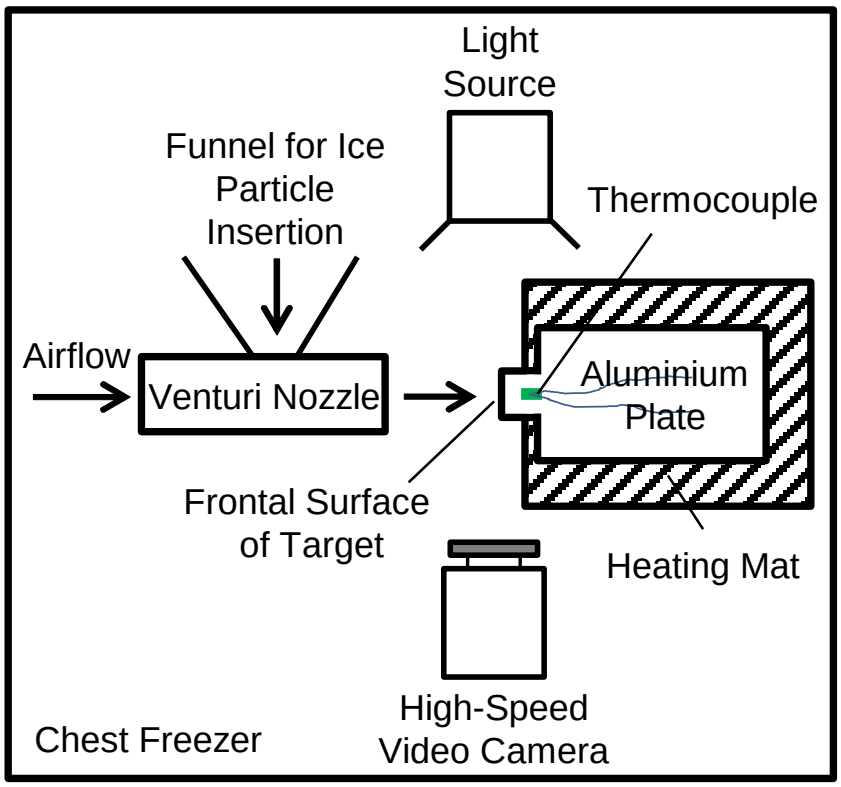

Figure 3-1. Sketch of the test apparatus, located in a chest freezer, for exploratory ice accretion tests on a warm surface.

The main part of the test apparatus was located in a chest freezer to set ambient temperatures below freezing (Figure 3-1). A self-made Venturi nozzle was used to accelerate the ice particles with cold pressurised air. Before each test, a certain mass of ice particles was collected from the chest freezer's walls. At the beginning of a test, the ice particles were

poured into the funnel and entered the nozzle perpendicular to the direction of the airflow. The target consisted of a polished aluminium plate. The plate was attached to a power-controlled heating mat to set the target's surface temperature. A thermocouple was installed 3 mm behind the frontal surface of the target, where the ice particles hit, to estimate its temperature. The area of the frontal surface of the target was 2.5 mm². A 12x zoom lens (Navitar, Rochester, USA) attached to a high-speed video camera (Photron Fastcam SA1.1, Photron Europe Limited, West Wycombe, UK) was used to record a side view of the ice accretion process. A cold light source (Dedocool, Dedo Weigert Film GmbH, Munich, Germany) for illumination was placed next to the target. A close-up view of the test apparatus is shown in the Appendix.

3.2 Cold versus Warm Surface in Glaciated Icing Conditions

Two tests with a cold and warm target surface were conducted which allow the investigation of the role of the surface temperature on ice accretion. Both tests were conducted with a cold flow and fully frozen ice particles. In the case of the cold surface, flow, surface, and ice particle temperatures were approx. -8 °C. In the case of the warm surface, the surface was continuously heated with constant electrical power and had an initial temperature of approx. +7 °C under active flow. Flow and ice particle temperatures were approx. -10 °C. The mean velocity of the ice particles was approx. 5 m/s. The IWC values were estimated to be approx. 2400 g/m³. This value seems to be very large at first. However, assuming that aircraft experience glaciated icing conditions at cruise speed (~250 m/s) in ambient IWC values up to 10 g/m³ and considering the fact that local IWC in the compressor can be more than ten times higher than the ambient IWC[90], the ice particle mass fluxes in the experiments are comparable to the ones found in a real flight in the engine core. In both tests, the stream of ice particles lasted approx. 400 ms.

In the case of the cold surface (Figure 3-2), ice accretion did not occur since ice particles simply bounced off the surface. This observation agrees with more macroscopic experimental results described by Mason et al.[22]. The temperature of the frontal surface of the target remained at -8 °C (Figure 3-3).

In the case of the warm surface, significant ice accretion was observed after 50 ms consisting of meltwater and ice (*slushy layer*). The ice accretion grew till the stream of ice particles stopped at $t = 400$ ms. The estimated temperature of the frontal surface of the target decreased initially due to the heat flux from the relatively warm surface into the cold slushy

layer, where ice was heated to the melting point and melted, and meltwater evaporated (Figure 3-3).

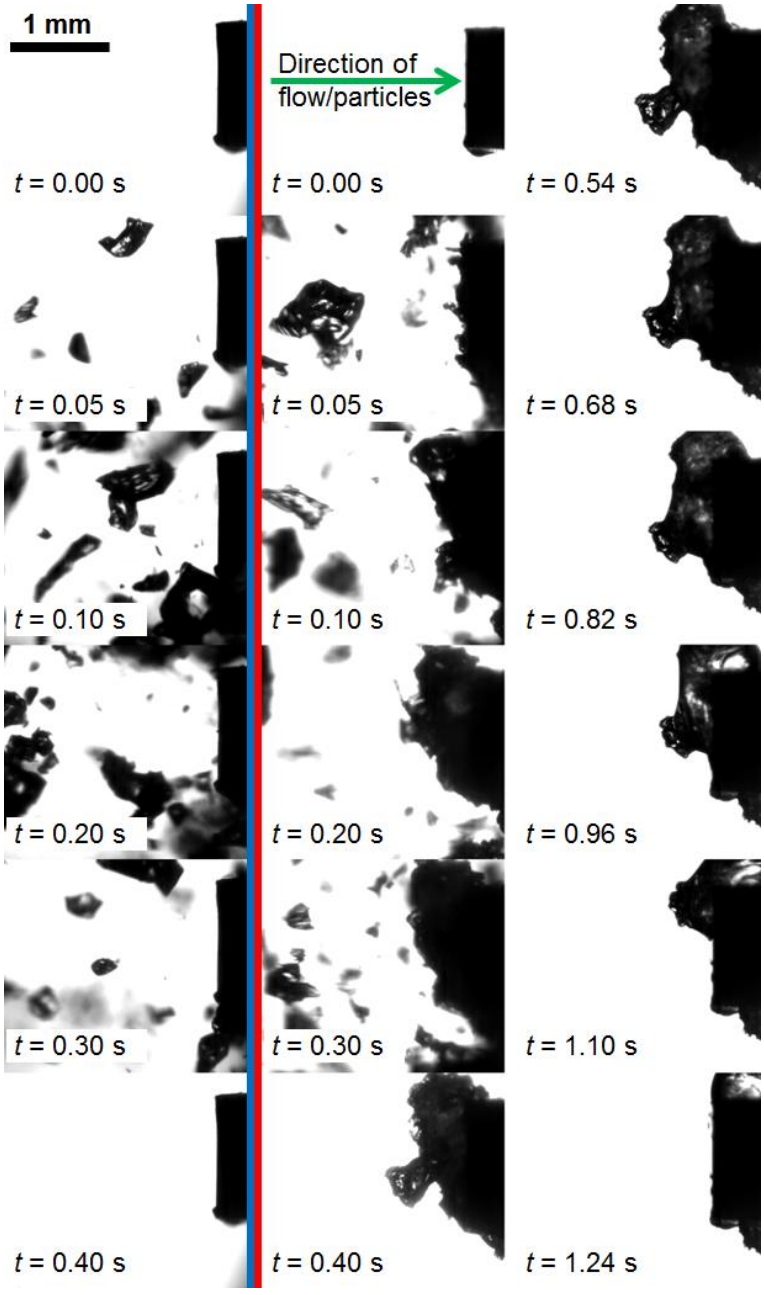

Figure 3-2. Comparison of ice accretion on cold (left) and warm surface (centre and right) in glaciated icing conditions. Cold surface: no ice accretion. Warm surface: ice accretion and shedding. Ice particles travelled from left to right.

At $t = 600$ ms, the temperature reached a minimum and slowly increased again due to the cessation of the ice particle stream and the continuous heat flux from the heating mat. It is

assumed that the measured temperature did not reach 0 °C due to the sensor's position ~3 mm behind the target's frontal surface and the short duration of the particle stream.

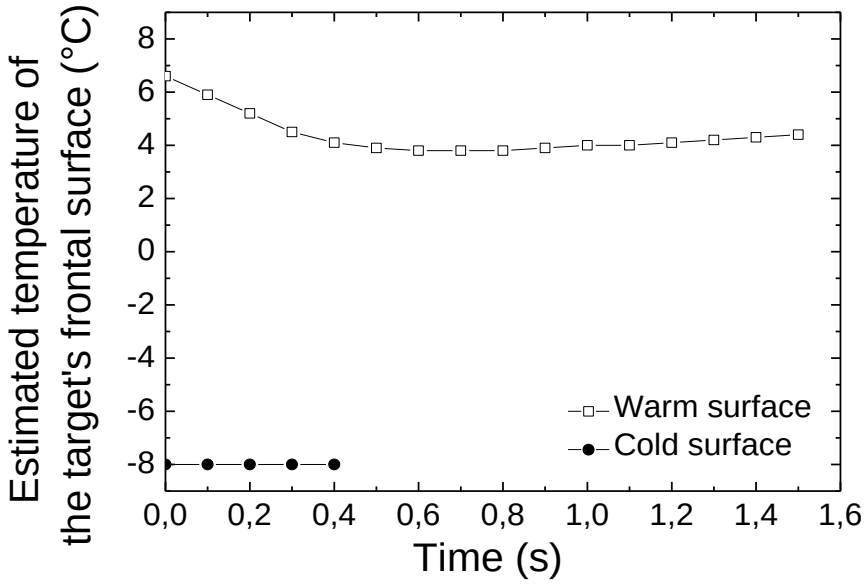

Figure 3-3. Estimated temperature evolution of the target's frontal surface during the cold and warm surface tests.

It was observed that ice particles accreted by sticking to the slushy layer within approx. the first 100 ms when capillary forces acted between the surface, liquid, and ice particles. From approx. 100 ms onwards, the ice accretion mainly grew by the mutual mechanical interlocking of (dry) ice particles. It was not possible to observe if refreezing took place at the surface or to which extent the surface was covered by a liquid layer.

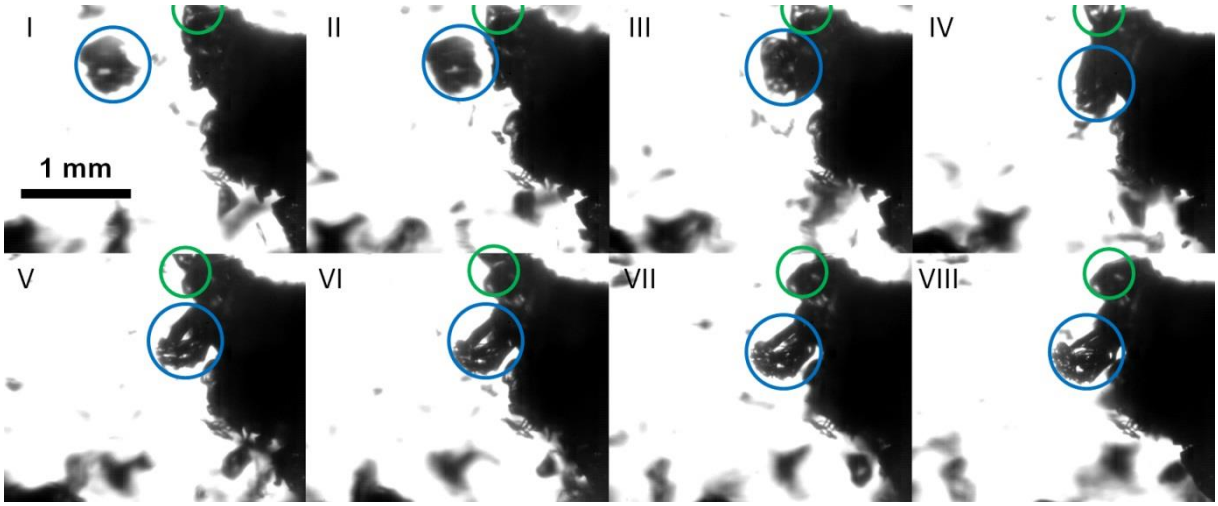

Figure 3-4. Removal of an ice particle (green circle) from the slushy layer by another incoming ice particle (blue circle). Time step between frames is 100 µs.

Ice particles being removed from the slushy layer by other arriving ice particles were observed. Figure 3-4 shows a typical impact of an ice particle (blue circle) onto another one (green circle) belonging to the slushy layer. Due to sufficient momentum transfer between the particles, the ice particle marked by the green circle was pushed away from the slushy layer. Between $t = 0.4$ s and $t = 1.24$ s (Figure 3-2), the bigger part of the slushy layer was melted by the heat flux provided by the heating mat. The formation of meltwater can be clearly seen at $t = 0.68$ s. Due to aerodynamic forces acting on the almost completely melted slushy layer, it is fully shed till $t = 1.24$ s.

In another test, where the target's surface temperature was initially lower (~3 °C), ice shedding of a relatively large piece of ice, presumably sliding on a growing liquid layer, was observed. The shedding took place shortly after the stop of the ice particle stream under active flow (Figure 3-5).

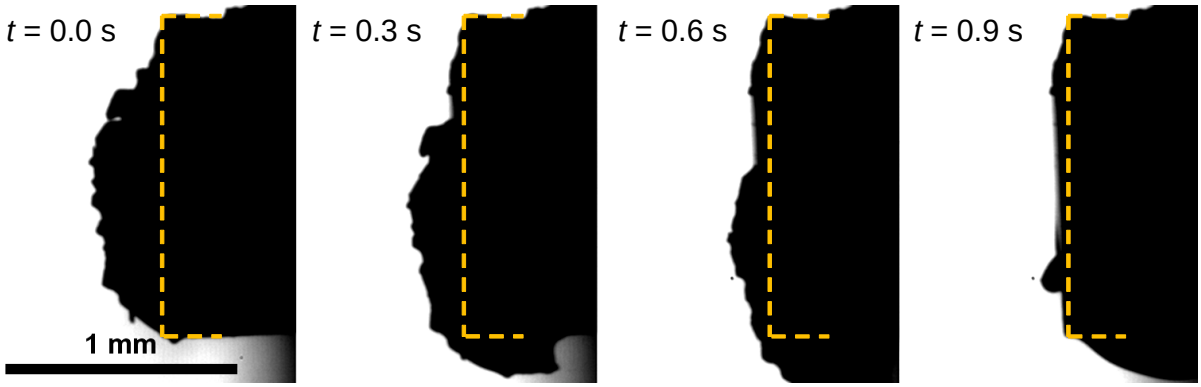

Figure 3-5. Ice shedding of largely frozen piece of ice. Orange dash line shows approximate position of target's frontal surface.

3.3 Detailed Mechanisms of Ice Accretion

In this section, the mechanisms initiating ice accretion in glaciated icing conditions are shown in detail. These investigations were conducted with high frame rates (up to 67,000 fps) and high magnifications (up to 6 µm/pixel). The IWC was approx. 240 g/m³, about one tenth of the value used in the previous section, to have a clear view of the target's frontal surface. The target's frontal surface temperature was approx. 25 °C and the temperatures of the flow and ice particles were approx. -18 °C. Impact velocities of the ice particles were approx. 23 m/s.

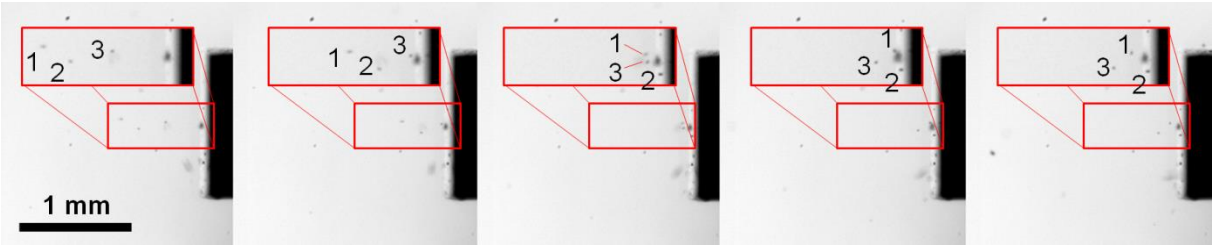

Figure 3-6. Impact of three very small ice particles (~10 µm) onto a warm surface. Particles 1 and 3 fully rebounded whereas particle 2 stuck to the surface and melted promptly.
Time step between frames is 14.9 µs.

Initially, liquid water droplets formed on the warm surface from tiny ice particles coming to rest after impact. In Figure 3-6, very small ice particles with maximum dimensions of the order of 10 µm impacted onto the warm, dry surface. Particles 1 and 3 fully rebounded whereas particle 2 stuck to the surface and melted immediately on first contact.

In Figure 3-7, another very small ice particle is shown which came to rest and melted on the surface on second contact after having lost a significant part of its kinetic energy during the first rebound.

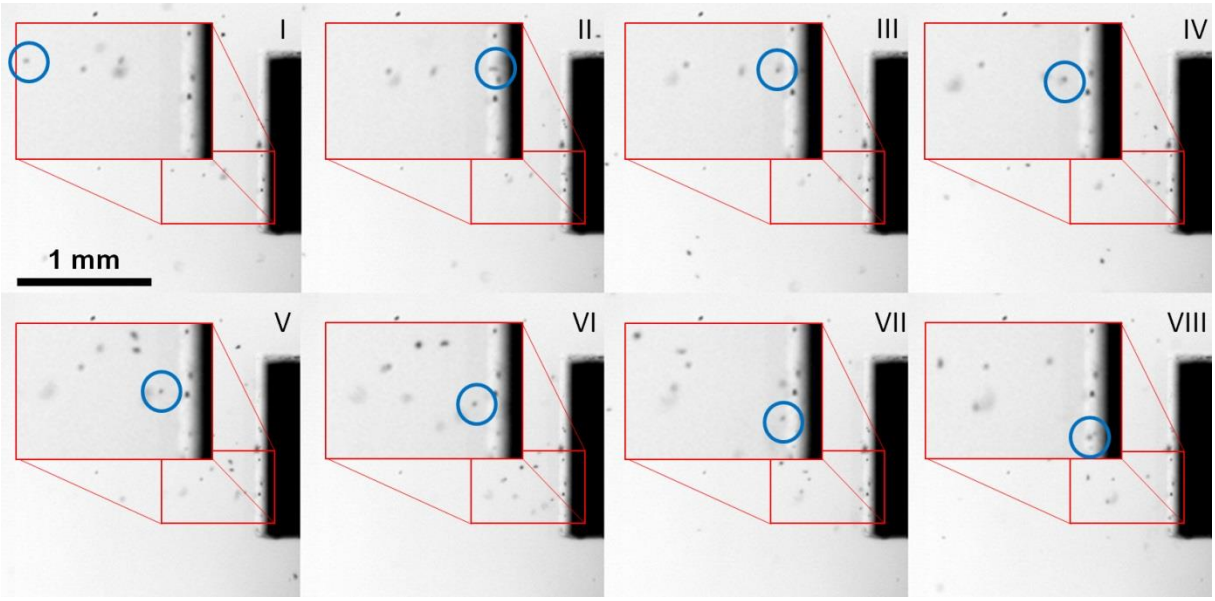

Figure 3-7. Sticking of very small ice particle (~10 µm) on second impact.
Time step between frames is 29.8 µs.

At this stage, sticking of ice particles larger than approx. 10 µm on the dry, warm surface was not observed. However, some larger particles were observed contributing to the development of the first droplets by leaving behind tiny residuals on the surface after impact. These residuals had maximum dimensions of few µm at most.

The subsequent mechanism is based on the presence of liquid droplets - or even a thin liquid film in the case of good surface wettability - on the surface which significantly increases the sticking probability of incoming ice particles due to capillary forces. With increasing droplet size/film thickness, larger and larger ice particles were observed to stick to the surface.

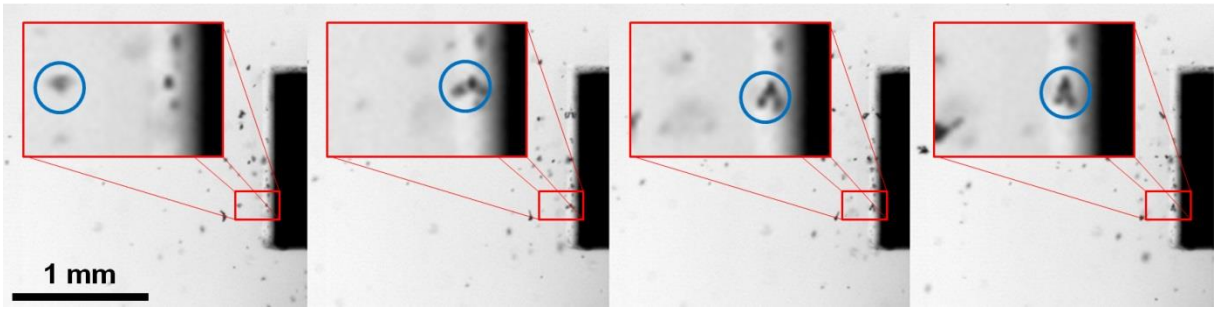

Figure 3-8. Sticking of very small particle (~10 µm) to droplet of comparable size. Time step between frames is 14.9 µs.

In Figure 3-8, a particle with a size of the order of 10 µm is shown. Upon impact, it stuck to a droplet of comparable size and melted.

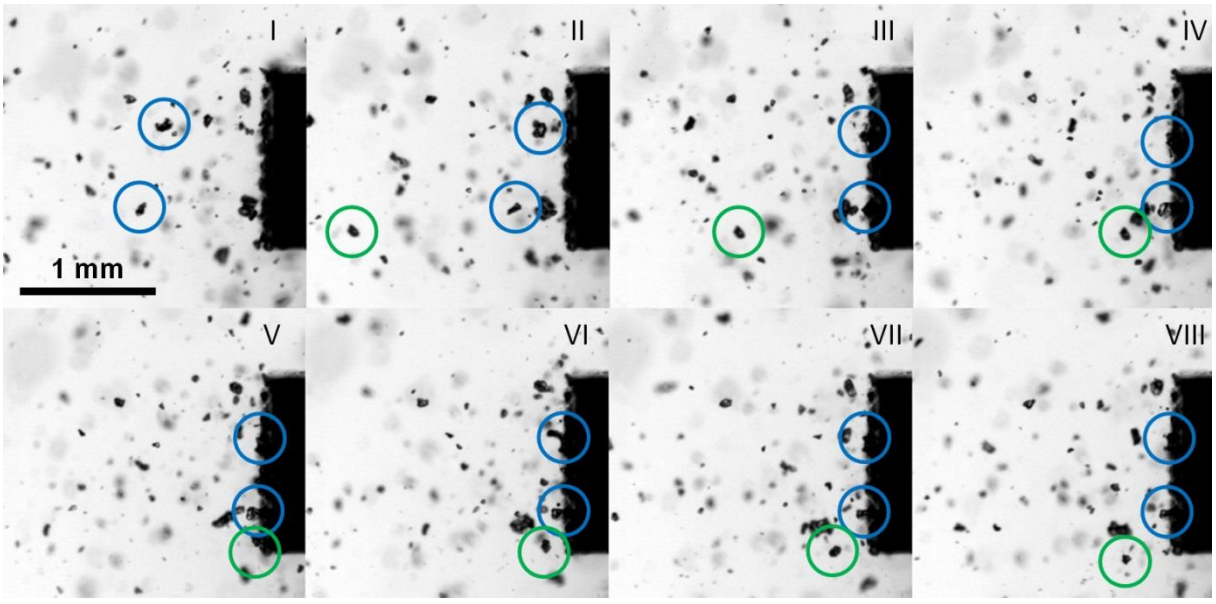

Figure 3-9. Small ice particles (~100 µm; blue circles) sticking to droplets. Simultaneously, rebound of another ice particle was observed (green circle). Time step between frames is 29.8 µs.

Some milliseconds later, larger droplets consisting of meltwater were observed on the target's frontal surface, which were able to capture ice particles with maximum dimensions of up to 500 µm (Figure 3-9 and Figure 3-10).

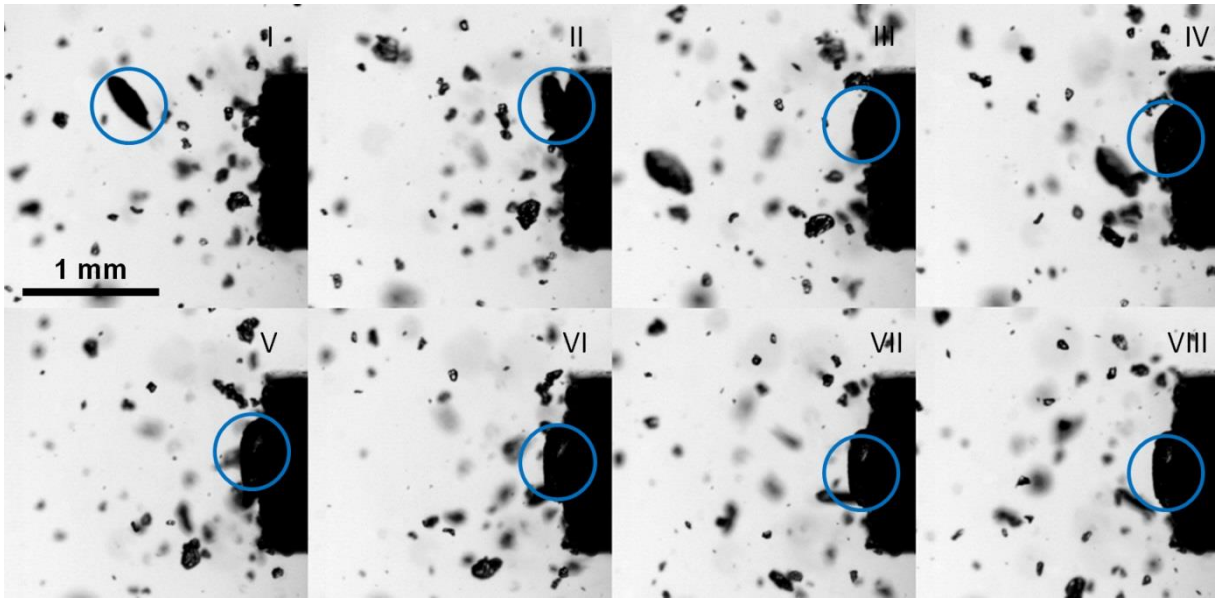

Figure 3-10. Relatively large ice particle with a maximum dimension of 500 μm stuck to layer of droplets. Time step between frames is 59.6 μs.

As discussed in the previous section, at this stage, a high ice particle mass flux may lead to a significant decrease of the target's frontal surface temperature, eventually reaching 0°C and promoting refreezing and ice accretion. In the present case, ice accretion was not observed after 57 ms when the stream of ice particles stopped (Figure 3-11).

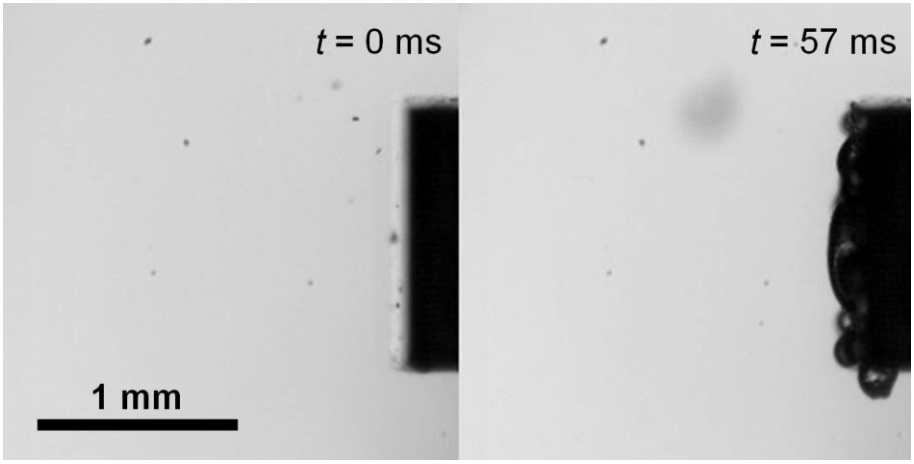

Figure 3-11. Target's frontal surface before and after stream of ice particles.

However, water accumulation on the target's frontal surface was visible. It is assumed that there was no ice accretion mainly due to the smaller and shorter ice particle mass flux and the warmer initial surface temperature in comparison to the warm surface case described in the previous section.

In the following, it is shown how partially melted ice particles may contribute to ice accretion in comparison to ice accretion by fully frozen ice particles. In Figure 3-12, an ice particle with a maximum dimension of 250 µm impacts onto a dry, inclined surface (25°) with a velocity of approx. 30 m/s. Surface and flow temperatures were 20 °C. It was not possible to determine from its initial shape if the particle was partially melted or fully frozen. However, upon impact the particle fragmented and started to rotate. Due to centrifugal forces, the particle lost at least part of its meltwater and its partially melted state became evident. The meltwater partially rested on the target's surface, potentially enhancing the sticking probability of further incoming ice particles.

Partially melted ice particles (Figure 3-13) as well as liquid droplets which deposit on the surface represent another source of water and may enhance sticking as well.

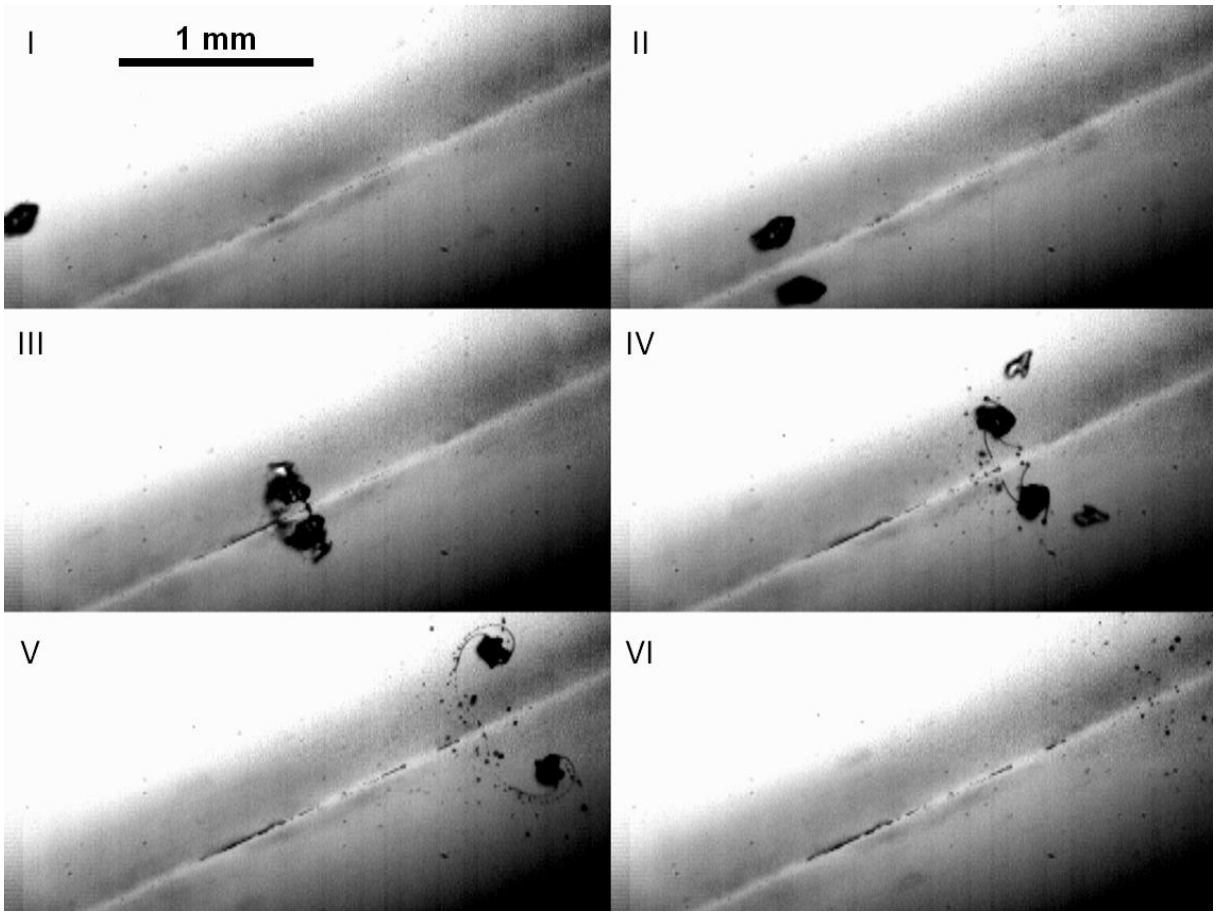

Figure 3-12. Fragmentation and rebound of a partially melted ice particle. Meltwater is released upon impact due to centrifugal forces. Meltwater on the surface may enhance sticking for further incoming ice particles. Time step between frames is 24.4 µs.

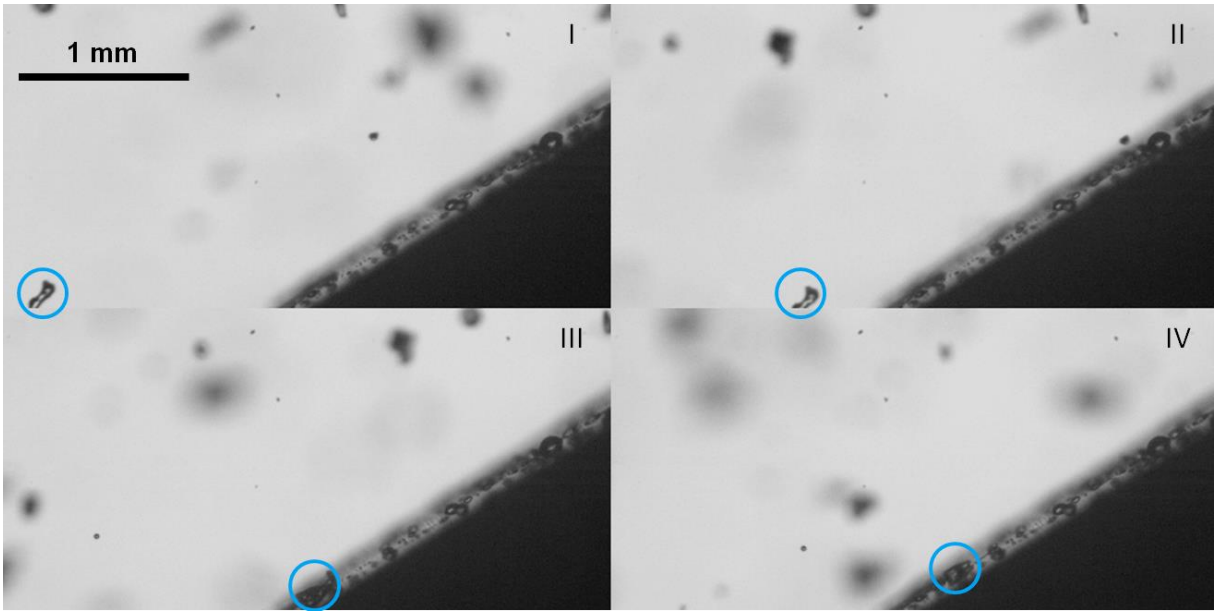

Figure 3-13. Partially melted ice particle coming to rest on surface. Time step between frames is 48.8 μs.

3.4 Summary and Conclusions

The exploratory experiments showed that drops or a film of liquid water on a surface are required for the initiation of ice accretion in glaciated icing conditions. On an initially dry, warm surface, liquid water spots are generated by tiny ice particles, or fragments of larger ice particles generated upon impact, which come to rest and melt on the surface. Moreover, partially melted ice particles and liquid droplets can provide liquid water to the surface to promote ice accretion. At these liquid water spots, larger and larger ice particles can stick due to capillary forces acting between the surface, liquid, and ice particles. Hence, a *slushy layer* is formed which absorbs heat from the surface. The presence of a slushy layer leads to a decrease of the surface temperature (Figure 3-14). The slushy layer can grow by further incoming ice particles either being captured by the liquid phase or, particularly in the case of incoming ice particles not being in contact with the liquid phase, by mechanical inter-locking. After the termination of the ice particle stream, the surface temperature may increase again. Shedding may also occur due to the presence of a liquid layer between the ice/slushy layer and the surface which allows sliding due to gravitational or aerodynamic forces. If no continuous liquid layer is present, these forces may also cause shedding if they overcome the adhesive forces between the ice/slushy layer and the surface. The factors which determine ice accretion and shedding are currently under investigation.

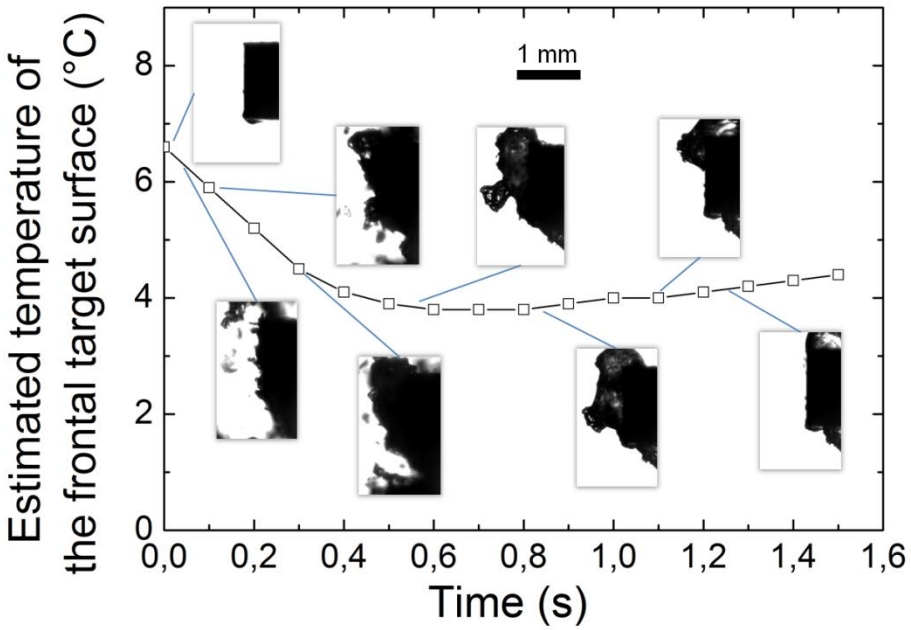

Figure 3-14. Illustration of the relation between the state of ice accretion on initially warm and permanently heated surface, and the surface temperature. Termination of the ice particle stream occurred at $t = 0.4$ s.

The observations described in this chapter confirm that further fundamental investigations of ice particle impact onto a dry and wet wall as well as melting in forced convection is crucial to be able in future to predict ice accretion in glaciated icing conditions.

To delay/reduce ice accretion in glaciated icing conditions, it is assumed that superhydrophobic, smooth, and inclined surfaces could be applied where possible. The inclination could cause less fragmentation due to the lower normal component of the impact velocity and the smoothness of the surfaces could lead to less abrasion of the ice particles (resulting in less tiny fragments). Moreover, superhydrophobic, inclined surfaces could lead to less water - in form of droplets or a film - on surfaces in the initial instants of ICI since the less wetting water droplets are more “easily” dragged away by the aerodynamic shear forces (instead of being pressed against the surface if it is normal to the flow) due to their larger aerodynamic cross section. Moreover, due to the superhydrophobic property of the surfaces lower adhesion forces between the water and the surface would contribute to easier removal as well. In presence of accreted ice at the surface, a heatable surface could loosen the bonds between the ice and the surface by generating a liquid water film between them and, hence, could promote ice shedding.

4 Ice Particle Impact onto a Dry, Cold Surface[‡‡]

The physics of ice particle impact and the mechanisms of fragmentation are not completely understood, e.g. the role of different crack types such as lateral or radial cracks. To extend the understanding of the impact process of small ice particles and to develop models which capture the main physics of particle impact onto a rigid surface, an experimental and theoretical study was conducted. An experimental test apparatus was developed which allowed the investigation of the impact process of non-spherical and spherical ice particles with diameters ranging from approximately 30 µm to 3.5 mm. The impact velocity was varied from 1 to 74 m/s. The impact angle was set to 30° or 90°. The impact process was observed and the main modes of particle fragmentation were identified. Considering similar phenomena relevant in the fields of penetration mechanics and transport of granular materials, e.g. the impact of an elastoplastic spherical particle onto a solid substrate investigated by Andrews[91] and the impact of an elastic-plastic long rod onto a perfectly rigid substrate[92,93], velocity scalings were proposed for different fragmentation modes. The scalings are based on the assumption of lateral and radial/median cracks developing in the particle upon impact and they describe fragmentation threshold velocities as a function of particle size. Probability distributions for various fragmentation modes were determined and the post-impact angles and velocities of the fragments were analysed.

4.1 Materials and Methods

The ice particle impact experiments were conducted in the Icing and Contamination Research Facility (iCORE)[94] at Airbus Group Innovations in Munich, Germany (Figure 4-1). iCORE is a laboratory icing wind tunnel with a test section height of 15 cm and width of 10 cm. The icing wind tunnel allowed the control of the airflow temperature within the transparent test section during the impact tests in the range from 0 °C to -40 °C. The pressure within the test section was measured by a pressure transducer array (Aerolab LLC, Laurel, USA).

[‡‡] This chapter is largely based on the publication: Hauk, T., Bonaccurso, E., Roisman, I. V, and Tropea, C., "Ice crystal impact onto a dry solid wall. Particle fragmentation," *Proceedings of the Royal Society A: Mathematical, Physical and Engineering Science*, vol. 471, Sep. 2015.

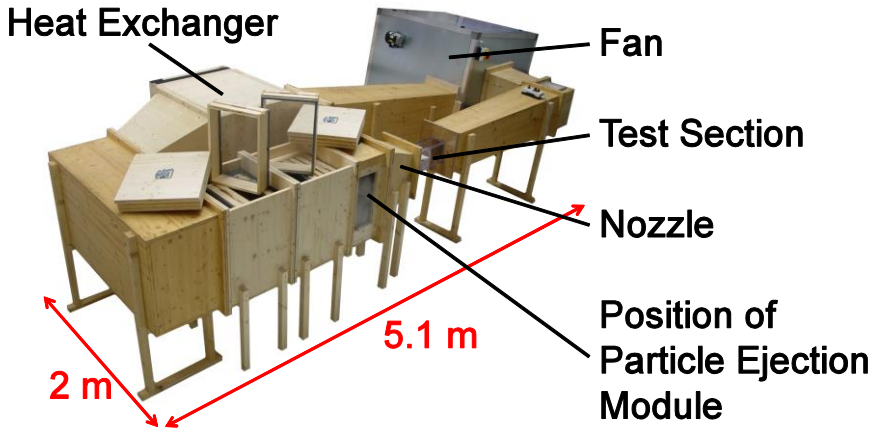

Figure 4-1. Overview of the icing and contamination research wind tunnel (iCORE).

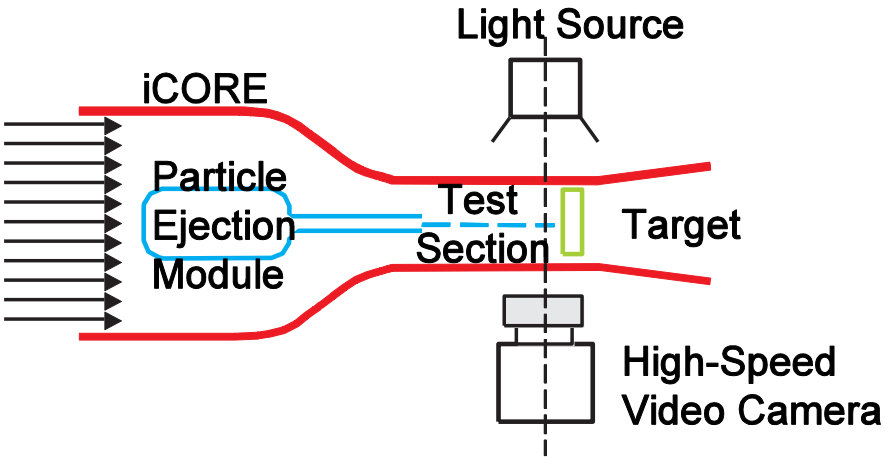

Figure 4-2. Schematic of the experimental setup for ice particle impact tests. Ice particles were accelerated with the particle ejection module and hit the target placed in the test section. The impact of the ice particles were recorded by a high-speed video camera.

4.1.1 Experimental Apparatus

A schematic of the experimental setup is shown in Figure 4-2. A particle ejection module accelerated the ice particles. An aluminium target was placed in the centre of the test section. The particle impact and fragmentation process was recorded with a high-speed video camera (Phantom v611, Vision Research Inc., Wayne, USA) in shadowgraphy mode. The images were analysed with a self-written MATLAB (MathWorks Inc, Natick, USA) code to extract the projected area, maximum dimension, and two-dimensional velocity vector of the initial particle and of the largest fragment after impact. The particle ejection module is aerodynamically shaped and was placed upstream of the nozzle. The particle ejection module was loaded with small portions of ice particles (typically a few mg). Cold compressed air

stored in an inner reservoir was used to accelerate the ice particles in a tube which ended approximately 20 mm upstream of the target. Directly using the airflow to accelerate portions of ice particles had the advantage that loose aggregations were separated and single ice particles impacted the target. The air pressure in the particle ejection module was controlled by a pressure gauge to set the impact velocity of the particles. The target consisted of a polished aluminium plate with an impact surface of size 2.0 × 1.4 mm. The aluminium plate was attached to a tilting mount to control the impact angle. The optical and recording system consisted of a high-speed video camera which was placed next to the transparent test section. A 12X Zoom lens (Navitar, Rochester, USA) was mounted to the high-speed video camera allowing to image an impacting ice particle with sufficient resolution. Opposite to the camera, a cold light source (Dedocool, Dedo Weigert Film GmbH, Munich, Germany) was positioned for illumination. A close-up view of the test apparatus is shown in the Appendix.

4.1.2 Test Procedure

The target was tilted to control the impact angle of the ice particles. The airflow velocity was set to approximately 5 m/s and the power of the heat exchanger was adjusted to attain the desired ambient temperature in the test section. Naturally grown, *non-spherical ice particles*, scraped from the wall of a chest freezer, whose ambient temperature was approximately -25 °C, were placed in the cooled particle ejection module. The equivalent projected area diameter of the non-spherical particles ranged from approximately 30 to 800 µm. The high-speed video recording was started simultaneously with the particle ejection. *Spherical ice particles* were prepared on a superhydrophobic metal plate. First, non-spherical ice particles of different sizes were spread on the superhydrophobic plate at room temperature. Upon melting, the ice particles formed small water droplets with an almost spherical shape. The plate with the droplets was then placed in a chest freezer and after several minutes the frozen droplets could be collected from the plate with a cold brush and fed into the particle ejection module. The diameter of the spherical particles ranged from approximately 260 to 3500 µm. The ambient temperature, ice particle temperature and target temperature were between -10 and -20 °C. The uncertainty of the particle velocity was 2 %. The resolution of the pictures varied between 5.9 and 16.7 µm/pixel, depending on the preset magnification. The uncertainty of the particle's maximum dimension ranged from ±2 to ±7 pixels.

4.2 Observations of Particle Fragmentation

Based on the experimental observations, four different fragmentation modes of non-spherical and spherical ice particles were defined in this work:

- No fragmentation
- Minor fragmentation
- Major fragmentation
- Catastrophic fragmentation

No Fragmentation. In this mode, ice particles bounce off the target's surface without being damaged to any extent. No fragments form. Figure 4-3 shows two sequences of particle bouncing. Figure 4-3a shows six consecutive images of a non-spherical ice particle with a maximum dimension of 200 µm and an impact velocity of 6.9 m/s. Significant particle rotation, i.e. the tangential velocity is comparable to or larger than the translational velocity, occurred upon impact. Figure 4-3b shows a spherical ice particle with a diameter of approximately 1200 µm and an impact velocity of 1.3 m/s. No post-impact rotation occurred.

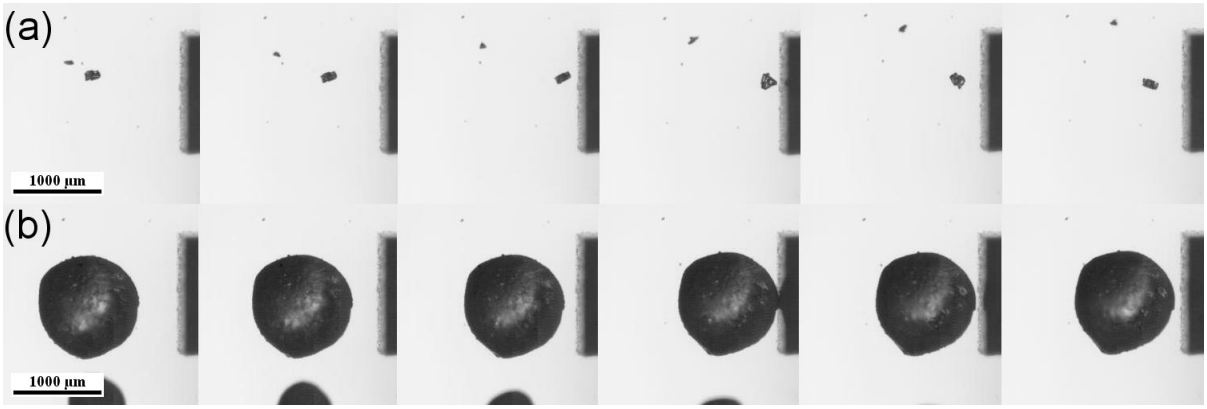

Figure 4-3. "No fragmentation" mode impact of a non-spherical, (a), and spherical ice particle, (b). Time step between single frames of the top sequence is 59.6 µs and of the bottom sequence is 119.2 µs.

Minor Fragmentation. In the case of "minor fragmentation", small fragments are observed. Up to 20 % of the original particle volume is shattered into fragments. Figure 4-4a shows the impact of a non-spherical ice particle with a maximum dimension of 300 µm and an impact velocity of 26 m/s. A small ice residual, stemming from the original particle, was observed on

the target's surface after impact. The ice sphere in Figure 4-4b had a diameter of approx. 1130 µm and a velocity of 5.1 m/s. Significant particle rotation was observed in both cases after impact.

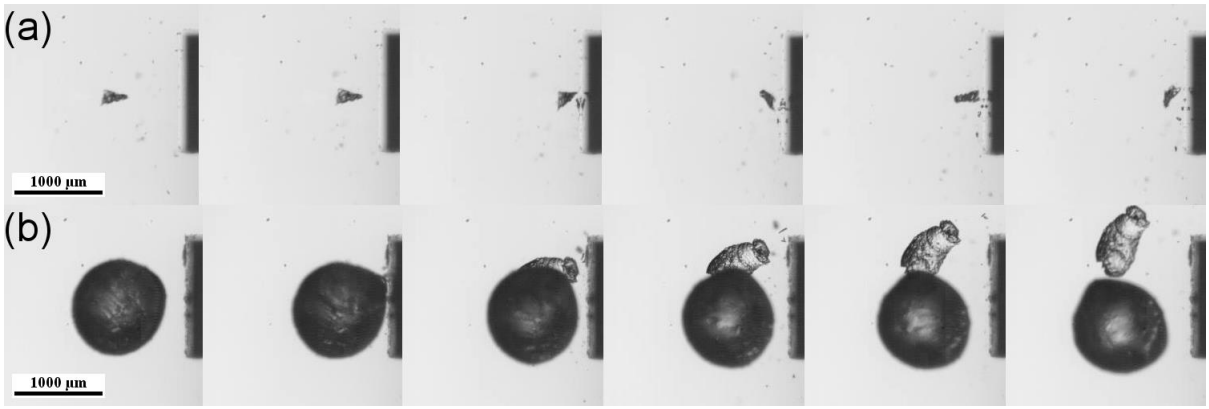

Figure 4-4. "Minor fragmentation" mode impact of a non-spherical, (a), and spherical ice particle, (b). Time step between single frames of top sequence is 14.9 µs and of bottom sequence is 75 µs.

Major Fragmentation. "Major fragmentation" occurs if between 20 and 50 % of the original ice particle volume is lost due to fragmentation. In Figure 4-5a, the maximum particle dimension was approximately 280 µm and the impact velocity was 36 m/s. A small residual on the surface was observed. In Figure 4-5b, an almost spherical particle is shown which was nearly split in half upon impact. Particle diameter was approximately 440 µm and impact velocity was 11 m/s. In both cases, significant post-impact particle rotation took place.

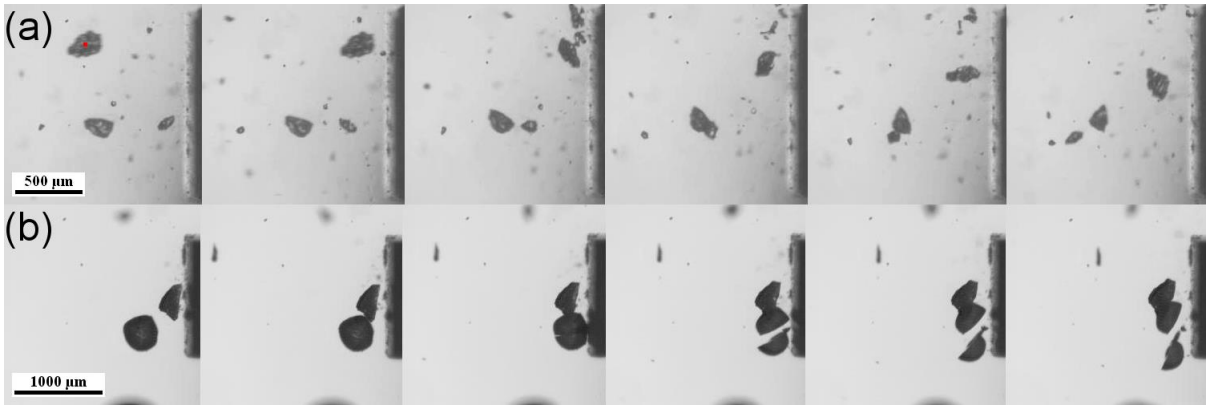

Figure 4-5. "Major fragmentation" mode impact of a non-spherical, (a), and spherical ice particle, (b). Time step between single frames is 14.9 µs.

Catastrophic Fragmentation. In this mode, more than 50 % of the original volume of the ice particle is affected by fragmentation. Several fragments are generated as an outcome of the

impact. In the extreme case, the particle shatters into hundreds of small fragments. In Figure 4-6a, a non-spherical particle with a maximum dimension of approximately 360 µm and an impact velocity of 48 m/s fragmented into several small particles. A small residual stuck to the surface at the impact location. In Figure 4-6b, a spherical particle with a diameter of approx. 960 µm impacted at a velocity of 36 m/s and broke apart completely.

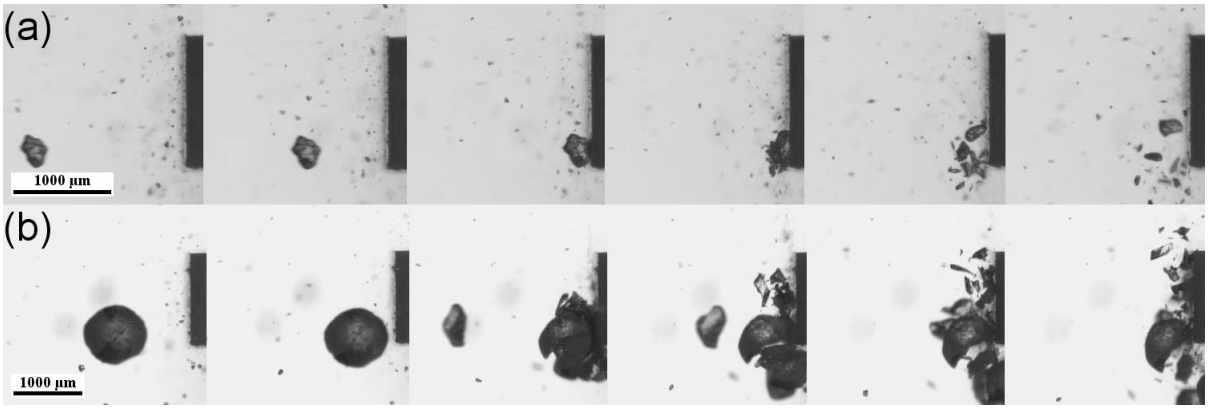

Figure 4-6. "Catastrophic fragmentation" mode impact of a non-spherical, (a), and spherical ice particle, (b). Time step between single frames is 14.9 µs.

In approx. 80 % of the impact cases, no significant particle rotation was observed before impact. Upon impact, if the particle was either of non-spherical shape or showed major or catastrophic fragmentation, at least part of the fragments started to rotate. In the case of the spherical ice particles, which showed no or minor fragmentation, the particles or fragments started rotating after impact in 75 % of the cases. In between 30 and 40 % of the cases where fragmentation occurred, small ice fragments stuck to the surface after impact. The volume of these residuals was at most few percent of the total volume of the original ice particles.

4.3 Mechanisms of Particle Fragmentation

The collision of a spherical (ice) particle onto a perfectly rigid, flat *target* is shown schematically in Figure 4-7. The particle deformation, recently analysed theoretically by Roisman & Tropea[43], consists of the *crushed region* near the target, the *plastic deformation region*, and the *rear part* of the particle. The rear part contains a *fine fragmentation region* and *propagating cracks*. The zone which includes propagating cracks near the particle surface can be fragmented. Later in the text, we will call this zone a *fragmentation region* (not shown in Figure 4-7).

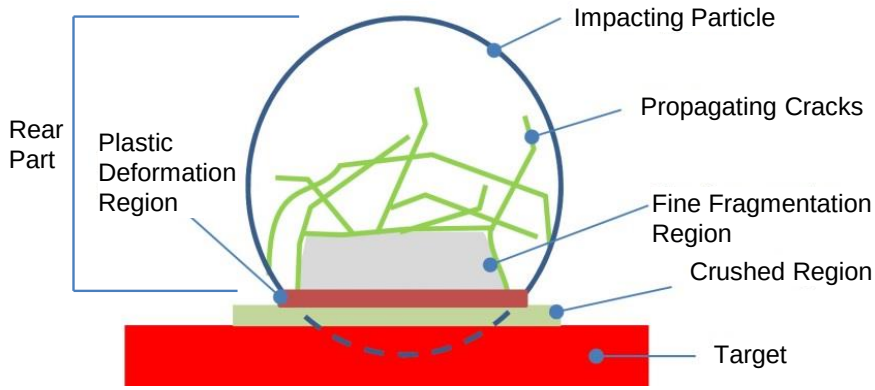

Figure 4-7. Sketch of the fragmentation of an impacting (ice) particle. Definition of the crushed, plastic deformation, and fine fragmentation region, and the propagating cracks.

The description of the formation and propagation of cracks in different materials is a rather complicated topic, belonging to fracture mechanics. Upon impact of semi-brittle materials like ice, cracks are generated. In the following analysis, we obtain typical velocity scales associated with the cracking process leading to different types of particle fragmentation. Simplified scaling models are used which, however, allow to capture the main physics of particle fragmentation.

In this study, two main types of cracks are considered: lateral cracks parallel to the surface, leading to particle attrition and splitting (at higher velocities), and radial or median cracks, leading to particle breakup. The geometry of these cracks is defined in Figure 4-8. We assume that these two types of cracks may be responsible for the fragmentation of ice particles.

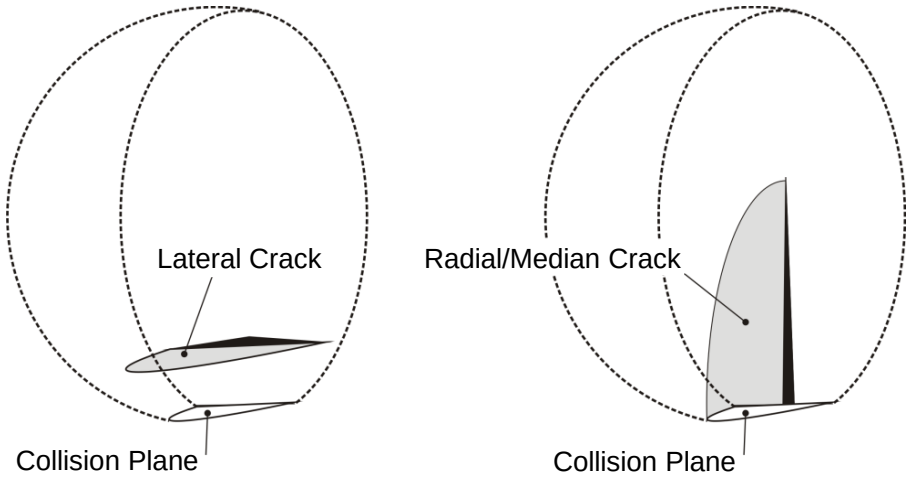

Figure 4-8. Sketch of the main types of cracks appearing in semi-brittle materials: lateral cracks, leading to attrition and splitting (at higher velocities), and radial or median cracks, leading to breakup.

4.3.1 Lateral Crack Formation in Ice Particles

Assuming that ice behaves like semi-brittle material during impact, the propagation of cracks in the particle can be described by results from Evans & Wilshaw[95] and Ghadiri & Zhang[96] for various configurations and particle geometries. For an impacting particle the scaling for the length of a crack l_{cr}:

$$l_{cr} \sim \frac{Y a^{3/2}}{K_c} \tag{4-1}$$

can be applied. In Eq. (4-1), Y is the yield strength of ice, a is the impression radius, and K_c is the fracture toughness. The scaling in Eq. (4-1), namely the dependence of the length of the fragmentation region as power "3/2" of the impression radius, was derived for a cubic impactor geometry, but it can be shown that it is independent from the geometry by fitting results obtained with a cylindrical ice crystal impactor, as shown in Figure 4-9.

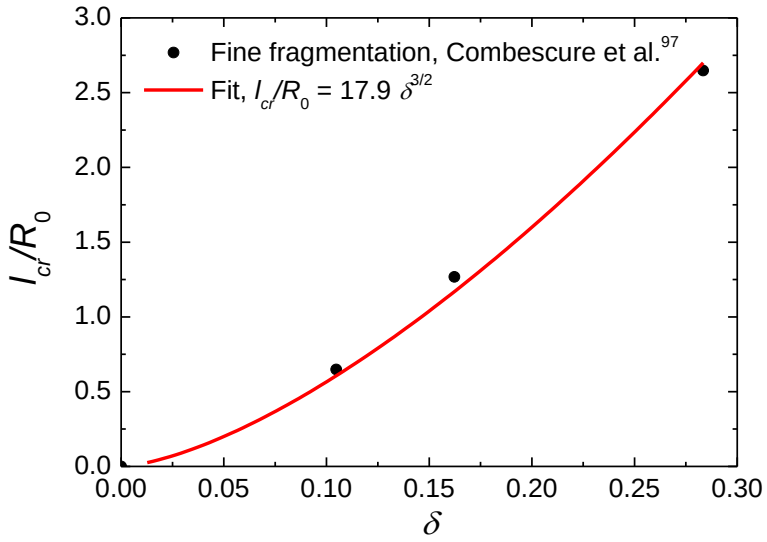

Figure 4-9. The dimensionless length of the fragmentation region, l_{cr}/R_0, in an impacting ice crystal cylinder as a function of the dimensionless length of the crushed region $\delta = (L_0\text{-}L)/R_0$, where L_0 and L are the initial and instantaneous cylinder length, R_0 is its radius. The experimental data are obtained from the images of the ice crystal impactor in Figure 13 from Combescure et al.[97]. δ for a cylinder is associated with the instantaneous impression radius a for a spherical particle.

These measurements are obtained from the images of the impactor in Figure 13 from Combescure et al.[97].

The residual impression radius a for a spherical particle of radius R_0 having the normal impact velocity U_0 is determined by the particle deformation during its collision with the rigid target. The expression for the impression radius is obtained from Roisman & Tropea[43] and from Andrews[91] in the form:

$$a \sim R_0 U_0^{1/2} \left(\frac{\rho}{Y}\right)^{1/4}. \tag{4-2}$$

Therefore, the length of a crack in an ice particle can be scaled as:

$$l_{cr} \sim R_0^{3/2} U_0^{3/4} Y^{5/8} \rho^{3/8} K_c^{-1}. \tag{4-3}$$

The length of the lateral crack determines a spall radius of a crater produced by an impact of a solid particle onto an ice block[98–100]. This case is analogous to the phenomenon of impact of a cracked particle, considered in this study. Therefore, the physics of these two cases is the same. In Figure 4-10, the dimensionless spall radius R_{crater}/R_0 of craters produced by impacts of solid particles of radius R_0, measured in Kato et al.[98] and Lange & Ahrens[99], is shown as a function of the parameter:

$$\lambda \equiv R_0^{1/2} U_0^{3/4} Y^{5/8} \rho^{3/8} K_c^{-1}. \tag{4-4}$$

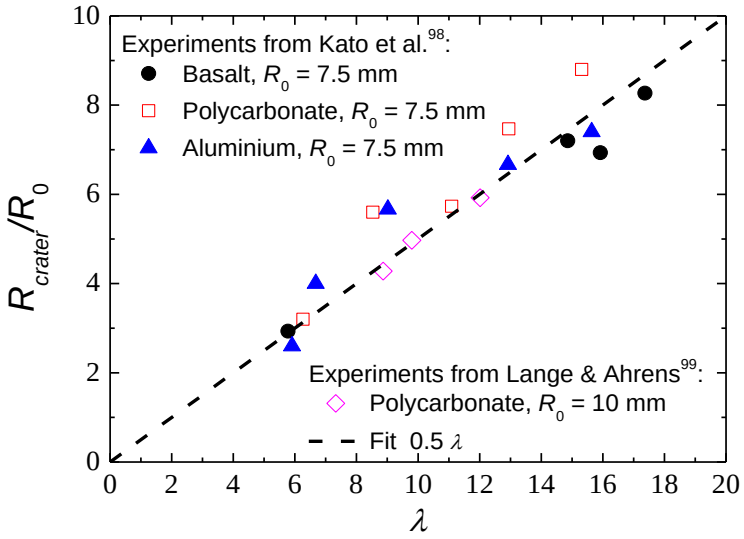

Figure 4-10. Solid particle impact onto an ice block. Dimensionless spall radius R_{crater}/R_0 as a function of the parameter λ, with $Y = 5.2$ MPa, $K_c \approx 10^5$ Pa m$^{1/2}$, Liu & Miller[101]. The experimental data are from Kato et al.[98] and Lange & Ahrens[99].

Linear dependence of the radius R_{crater}/R_0 on λ confirms the scale for the crack length in Eq. (4-3). Moreover, these two dimensionless parameters are of the same order. This fact also indicates the correctness of our estimation of the crack length.

4.3.2 Particle Attrition

The particle material spreading in the plastic deformation region can also lead to damage in the rear part of the particle. It is known that upon ice particle impact an expanding cracked region ahead of the plastic wave develops[40,43,102]. In a certain velocity range, this phenomenon leads to particle attrition[103].

If we assume that the thickness of the region fragmented by the lateral cracks is proportional to the impression radius a, the ratio of the volume of the fragmented region, to the initial particle volume, η, can be expressed in the form:

$$\eta \sim \rho Y K_c^{-2} R_0 U_0^2. \tag{4-5}$$

Equation (4-5) for the dimensionless attrition propensity parameter η is derived by Ghadiri & Zhang[96] for semi-brittle particulate solids. The idea that the thickness of the fragmentation region is proportional to the impression radius $a \sim U_0^{1/2}$, defined in Eq. (4-2), is confirmed by the linear dependence of the dimensionless measured maximum fragment diameter[36] on the square root of the impact velocity $U_0^{1/2}$, shown in Figure 4-11.

In the study of Pan & Render[36], the normal impact velocity was varied between 60 and 150 m/s and the particle diameters were 12.7 and 19.0 mm. It is assumed that the linear relation between D_{max}/D_0 and $U_0^{1/2}$ holds for the impact conditions described in this paper as well. Equation (4-5) yields the dependence of the typical attrition velocity in the form:

$$U_{attrition} \sim R_0^{-1/2}. \tag{4-6}$$

$U_{attrition}$ represents a definite level of relative damage of a particle by attrition, represented by a constant value of the dimensionless attrition propensity parameter η.

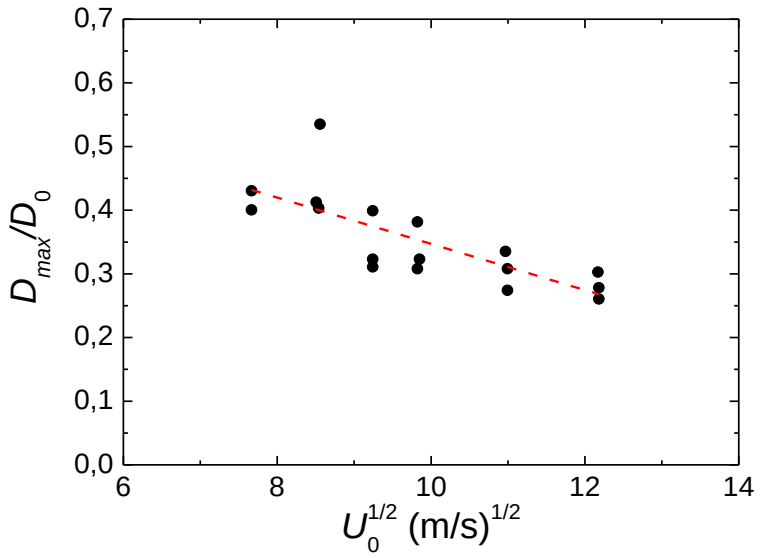

Figure 4-11. Size of the dimensionless maximum fragment diameter, D_{max}/D_0, as a function of the square root of the impact velocity $U_0^{1/2}$ ~ a. The experimental data are from Pan & Render[36].

4.3.3 Particle Splitting by Lateral Cracks

While attrition takes place at rather low impact velocities, the particle suffers more damage with increasing velocity breaking apart into fragments. As a plausible fragmentation criterion, we can take the condition at which the crack length (Eq. (4-3)) is comparable with the initial particle diameter ($l_{cr} \approx 2R_0$). In this case, the particle can be split by the developed crack. The condition for particle splitting is therefore:

$$U_{split} \sim K_c^{4/3} \rho^{-1/2} Y^{-5/6} R_0^{-2/3}. \tag{4-7}$$

4.3.4 Particle Breakup by Median/Radial Cracks

It was observed that the length of the median/radial cracks depends on the load P applied to a media. Marshall & Lawn[104] and Lawn et al.[105] have observed that for radial cracks:

$$\frac{P}{l_{cr,radial}^{3/2}} = \text{constant}. \tag{4-8}$$

In the present case, we can estimate the load as:

$$P \approx Y \pi a^2. \tag{4-9}$$

Using Eq. (4-2) for the impression radius a, we obtain the following expression for the length of a radial crack:

$$l_{cr,radial} \sim R_0^{4/3} U_0^{2/3}. \tag{4-10}$$

The critical impact velocity corresponding to the particle breakup by a median/radial crack, can be estimated from the condition $l_{cr,radial} \approx 2R_0$. The expression for this critical velocity $U_{breakup,radial}$ is obtained with the help of Eq. (4-10) in the form:

$$U_{breakup,radial} \sim R_0^{-1/2}, \tag{4-11}$$

which has the same dependence on the particle size as the attrition velocity, defined in Eq. (4-6).

In order to check the hypothesis that the outcome of ice particle fragmentation can be described by these two velocity scales, $U_{split} \sim R_0^{-2/3}$ and $U_{attrition}$ (or $U_{breakup,radial}$)$\sim R_0^{-1/2}$ associated with splitting and attrition/radial cracks, we perform an analysis of the experimental data considering different modes of particle fragmentation for various particle sizes. This analysis is presented in the next section.

4.4 Upper Bounds of No Fragmentation and Minor Fragmentation

Figure 4-12 shows the map of ice particle impact events leading to *no fragmentation* or *minor fragmentation* outcomes. Impacts of spherical and non-spherical particles are shown. In the case of non-spherical particles, D_0 represents the mean equivalent projected area diameter measured before impact. These results clearly demonstrate the dependence of the typical velocities, characterizing particle fragmentation, on the particle size. In general, the velocity of a specific fragmentation mode reduces with increasing particle size.

The threshold velocity for *no fragmentation* (above which any particle fragments or particle attrition can be identified) is scaled as:

$$U_0 \sim D_0^{-0.58}. \tag{4-12}$$

It should be noted that it is not always easy to identify particle damage, especially for small-sized particles. In any case, the experimentally determined scaling exponent, lying

between -0.5 and -0.66, suggests that the initial fragmentation is governed by both mechanisms, particle attrition (Eq. (4-5)) and splitting (Eq. (4-7)).

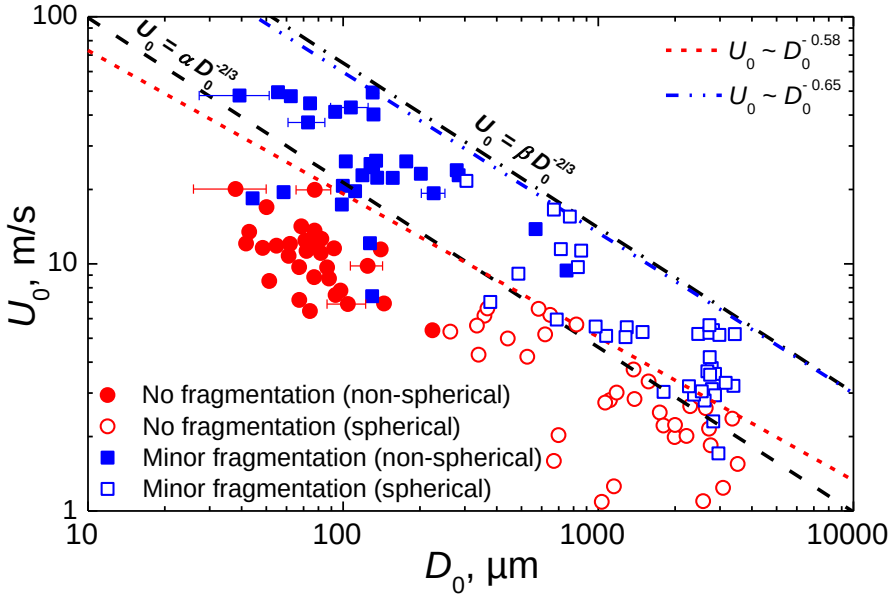

Figure 4-12. Map of *no fragmentation* and *minor fragmentation*. The upper bounds of *no* (long dash line) and *minor* (dash dot line) *fragmentation* are shown based on the model for particle splitting (Eq. (4-7)). Best fits to the *no fragmentation* (short dash line) and *minor fragmentation* (dash dot dot line) data are shown. Typical error bars for the initial particle diameter are shown. The error bars of the normal impact velocity are smaller than the symbols.

A best fit to the experimental data in Figure 4-12 shows that the threshold velocity for *minor fragmentation* (above which only major or catastrophic fragmentation associated with particle splitting have been observed) is scaled well as:

$$U_0 \sim D_0^{-0.65} \tag{4-13}$$

This scaling is very close to the predicted expression for the critical splitting velocity (Eq. (4-7)), which suggests that the transition between minor and major/catastrophic fragmentation is mainly governed by splitting.

In the further analysis, we thus assume that for high particle impact velocities, causing major or catastrophic fragmentation, particle fragmentation is governed mainly by splitting. In Figure 4-12, the upper boundary for *no fragmentation* and the upper boundary for *minor fragmentation* are described by the expressions:

$$U_0 = \alpha D_0^{-2/3} \tag{4-14}$$

and:

$$U_0 = \beta D_0^{-2/3}, \tag{4-15}$$

respectively.

$\alpha = 0.046\ \mathrm{m^{5/3}s^{-1}}$ and $\beta = 0.14\ \mathrm{m^{5/3}s^{-1}}$ are determined from manual fits to the experimental data. The fitting in the form $U_0 = \alpha D_0^{-2/3}$ describes relatively well even the threshold for *no fragmentation*, which supports the assumption that the transition from no fragmentation to minor fragmentation is partially based on splitting.

4.5 Probability of a Specific Fragmentation Mode

An empirical dimensionless variable:

$$\xi = \frac{U_0 D_0^{2/3}}{\beta}, \tag{4-16}$$

where $\beta = 0.14\ \mathrm{m^{5/3}s^{-1}}$, is introduced in order to describe the probability of a specific fragmentation mode based on the characteristic velocity scale for particle splitting. The units of U_0 and D_0 used in Eq. (4-16) are m/s and m, respectively. The experimentally obtained probability distributions for minor and major/catastrophic fragmentation are shown in Figure 4-13.

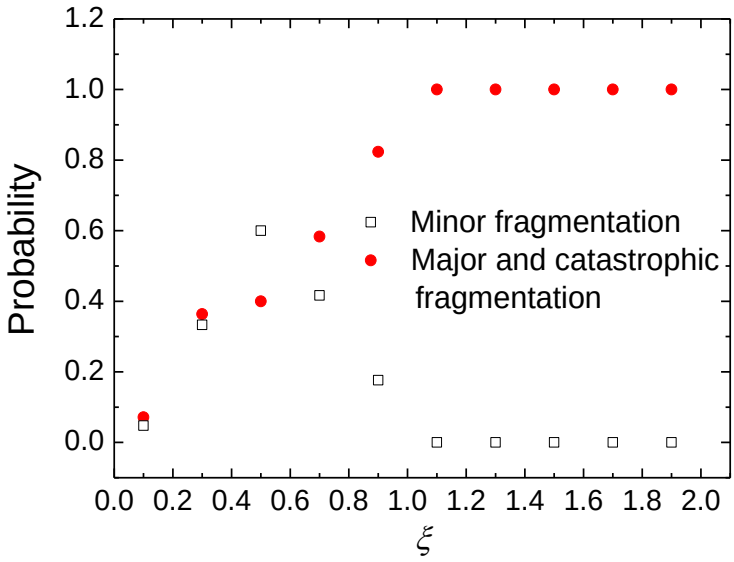

Figure 4-13. Probability for the minor and major/catastrophic particle fragmentation as a function of ξ defined in Eq. (4-16). The width of the ξ bins was 0.2.

For $\xi > 1.1$, the probability of the catastrophic fragmentation approaches unity, while for $\xi \to 0$, the probability of fragmentation approaches zero.

4.6 Post-Impact Velocity and Direction of Motion of the Fragments

Better understanding of the post-impact behaviour of the fragments (or of the original particle in the case of no fragmentation) is crucial to simulate their trajectories and to determine potential ice accretion locations within aircraft engines. For this reason, restitution coefficients as well as post-impact angles between the velocity vectors of the fragments and the surface (hereinafter referred to as "post-impact angles of the fragments") were analysed.

In the case of normal and oblique ice particle impacts, two restitution coefficients are defined: the normal restitution coefficient e_n, which considers the normal components of the impact and rebound velocities, and the tangential restitution coefficient e_t, which considers the tangential components of these velocities.

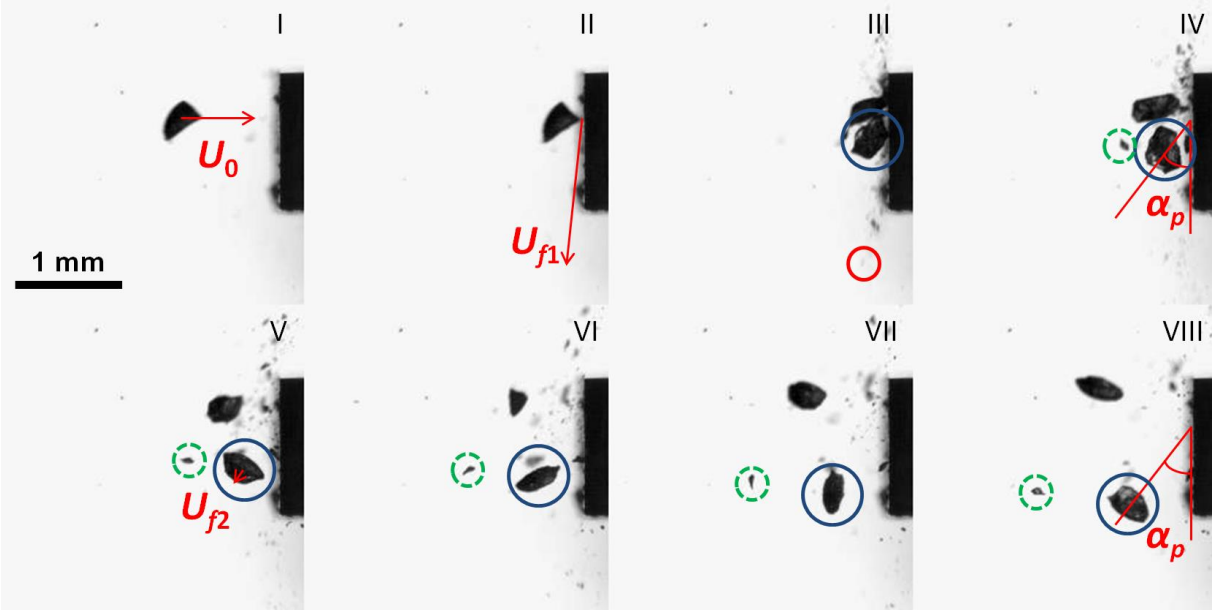

Figure 4-14. Major fragmentation impact of a non-spherical ice particle with a maximum dimension of approx. 400 µm. Time step between single frames is 14.9 µs. Post-impact velocity vectors ($\boldsymbol{U_{f1}}$ and $\boldsymbol{U_{f2}}$) of the fastest fragment (small red circle) and of the biggest fragment (blue circle) remaining in the focal plane as well as the initial impact velocity vector ($\boldsymbol{U_0}$) are shown. The lengths of the vectors represent the magnitudes of the velocities. The post-impact angle of the biggest fragment is also shown ($\alpha_p \approx 35°$). The green dash circle shows a small fragment with a larger post-impact angle (~60°) than the biggest fragment. Since 2D images were recorded only, the sum of the areas of all visible fragments can be larger than the area of the original ice particle.

In the case of fragmentation, it was observed that the first tiny fragments that formed upon impact ($D \lesssim 10$ µm) had post-impact velocities up to twice as large as the initial impact velocity (e.g. compare the lengths of the velocity vectors $\boldsymbol{U_{f1}}$ and $\boldsymbol{U_0}$ in Figure 4-14, which represent the magnitudes of the velocities). The angles between the velocity vectors of the first tiny fragments and the surface were shallow ($\alpha_p < 10°$), which is similar to the angles detected by previous observations on the impact of large ice particles ($D > 1.5$ mm)[37,39,41].

In Figure 4-14, most fragments leave the focal plane rapidly and their borders become blurry. In this case, it is not possible to determine the post-impact velocities and angles. In the following analysis, the post-impact behaviour of the biggest fragment only was analysed under the following conditions: 1) the biggest fragment did not significantly overlap with other particles/fragments and 2) the biggest fragment remained in the focal plane within approx. 1 mm of the impact location. Under these conditions, it was assumed that the angle between the focal plane and the biggest fragment's velocity vector was less than 10°.

Predominantly in the case of a minor or major fragmentation impact, it was observed that the biggest fragment had mostly a larger post-impact angle and a smaller post-impact velocity than the smaller fragments. For example, in Figure 4-14, where a major fragmentation impact is shown, the post-impact angle of the biggest fragment (blue circle) was 35° and, hence, was larger than the post-impact angles of the smaller fragments except for one (green dash circle) which had a post-impact angle of ~60°. The biggest fragment's total post-impact velocity was approx. 20 % of the initial velocity of the particle (compare the lengths of $\boldsymbol{U_{f2}}$ and $\boldsymbol{U_0}$). The biggest fragment had a smaller post-impact velocity than most of the other fragments.

In the case of a catastrophic fragmentation impact, it was often hard to determine the biggest fragment since there were several big fragments of comparable size. It was observed that the post-impact angles and velocities of these big fragments were similar. The volume of the biggest fragment was at least 10 % of the initial particle volume.

4.6.1 Impacts of Spherical Ice Particles

In Figure 4-15, the normal restitution coefficient e_n of the biggest fragment (or original particle in the case of no fragmentation) is illustrated versus ξ, defined in Eq. (4-16). ξ, which was previously successfully applied to illustrate the probability of different fragmentation modes, proved to be a suitable parameter for the illustration of the restitution coefficients and post-impact angles, as can be seen in the following. 30° and 90° impacts of spherical ice particles were considered. *No fragmentation* and *fragmentation* (including any kind of the three fragmentation modes) were distinguished.

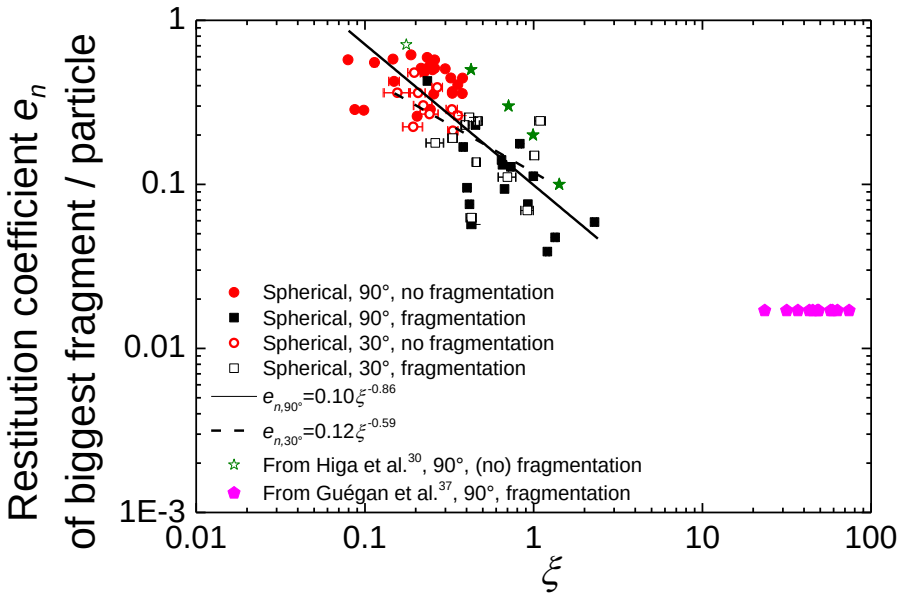

Figure 4-15. Normal restitution coefficient e_n versus ξ. The biggest fragments of originally spherical ice particles were analysed. Impact angles were 30° and 90°. For both impact angles, fits are shown. Similar results from Higa et al.[30] and Guégan et al.[37], who investigated the impact of larger spherical ice particles ($D > 2.8$ mm and $D > 6.2$ mm, respectively), are illustrated. With respect to the data from Higa et al., the hollow star represents a no fragmentation impact and the filled stars represent fragmentation. Typical error bars are shown for ξ, whereas error bars for e_n were smaller than the symbols.

It was observed that with increasing ξ, which is equivalent to the increase of the probability of major/catastrophic fragmentation, the normal restitution coefficient decreased. The same tendency was observed by Higa et al.[30], who investigated the normal impact of spherical ice particles onto an ice block. This tendency may be traced back to the transformation of the particle's initial kinetic energy into plastic deformation energy and surface energy due to the

development of cracks and fragments. Moreover, the fragments showed rotational motions storing a part of the initial kinetic energy as well.

In Figure 4-15, the normal restitution coefficients are approximated by the following two functions. In the case of 90° impacts:

$$e_{n,90°} = 0.10\xi^{-0.86}, \quad \text{for } 0.08 < \xi < 2.3, \tag{4-17}$$

and in the case of 30° impacts:

$$e_{n,30°} = 0.12\xi^{-0.59}, \quad \text{for } 0.16 < \xi < 1.1. \tag{4-18}$$

For $\xi < 0.4$, no fragmentation mostly occurred and the mean normal restitution coefficient in the case of normal impacts was larger than in the case of an impact angle of 30° (0.45 versus 0.31). Similar observations were made by Antonyuk et al.[106] for the impact of sodium benzoate granules onto a steel plate and by Kantak & Davis[107] for the impact of nylon and steel spheres onto a quartz disk. Antonyuk et al. concluded that this tendency of the mean normal restitution coefficient being larger in the case of normal impacts than in the case of an impact angle of 30° may be traced back to the surface roughness and small deviations from spherical shape. It is assumed that both conclusions hold for the presented oblique impacts of spherical ice particles which had shape imperfections and surface irregularities as well. However, the influence of the surface roughness of the spherical ice particles seems minor since the size of the irregularities seems smaller than observed by Antonyuk et al. (compare Figure 4-3 - Figure 4-6 with Figure 18 in their study). Generally, the normal restitution coefficients were larger in the case of no fragmentation than in the case of fragmentation.

For $\xi \gtrsim 0.4$, fragmentation occurred and the restitution coefficients decreased with increasing ξ approaching values observed by Guégan et al.[37] for $\xi > 20$. In their study, *perfectly catastrophic fragmentation* of spherical ice particles upon normal impact onto a glass target was investigated. Perfectly catastrophic impacts result in hundreds of fragments and a hardly identifiable biggest fragment which has less than 1 % of the initial volume of the spherical ice particle.

The restitution coefficients derived from Guégan et al. are based on their observations that the post-impact angle is 2° at most and that the total post-impact velocity of the fragments is approx. half of the initial velocity of the spherical ice particle.

In Figure 4-16, the post-impact angles of the biggest fragments (or the original particles in the case of no fragmentation) versus ξ are shown. The initial impact angle was 90°.

In the case of no fragmentation, the post-impact angle was close to the initial impact angle (mean value: 79°). Deviations from the expected 90° post-impact angle may be traced back to imperfections of the ice particle's internal structure and deviations from spherical shape.

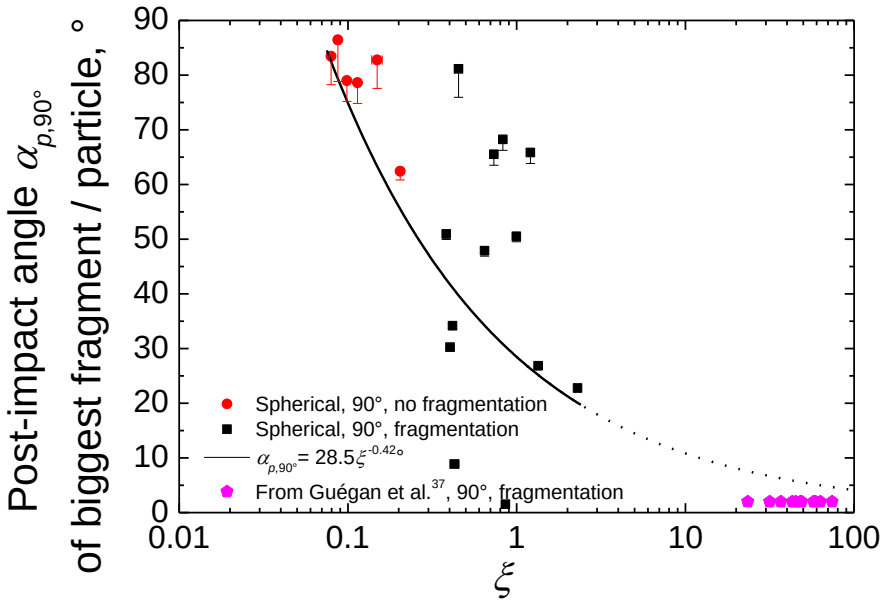

Figure 4-16. Post-impact angle $\alpha_{p,90°}$ versus ξ including fit to the data. Impact angle was 90°. In the case of no fragmentation, $\alpha_{p,90°}$ was close to 90°. With increasing ξ, $\alpha_{p,90°}$ decreased. The fit agrees well with results from Guégan et al.[37] Typical error bars are shown.

For $\xi > 0.4$, fragmentation occurred and the post-impact angle decreased with increasing ξ which is approximated by the following function:

$$\alpha_{p,90°} = 28.5\xi^{-0.42°}, \quad \text{for } 0.08 < \xi < 2.3. \tag{4-19}$$

The data was much more scattered than in the case of no fragmentation since particle fragmentation is a complex process including, e.g. the formation of cracks and fragment-fragment interaction, which influences the post-impact behaviour of the fragments. For large values of ξ ($\xi > 20$), the fit agrees well with the results of the post-impact angle from Guégan et al.[37].

In Figure 4-17, the tangential restitution coefficient e_t versus ξ is shown for an impact angle of 30°. In the case of no fragmentation, the mean tangential restitution coefficient was

approx. 0.95 which points out that friction between the particle and surface during contact was almost negligible. Significant particle rotation caused by the conversion of tangential kinetic energy into rotational energy was not observed. In the case of fragmentation, the mean value of e_t was approx. 0.88.

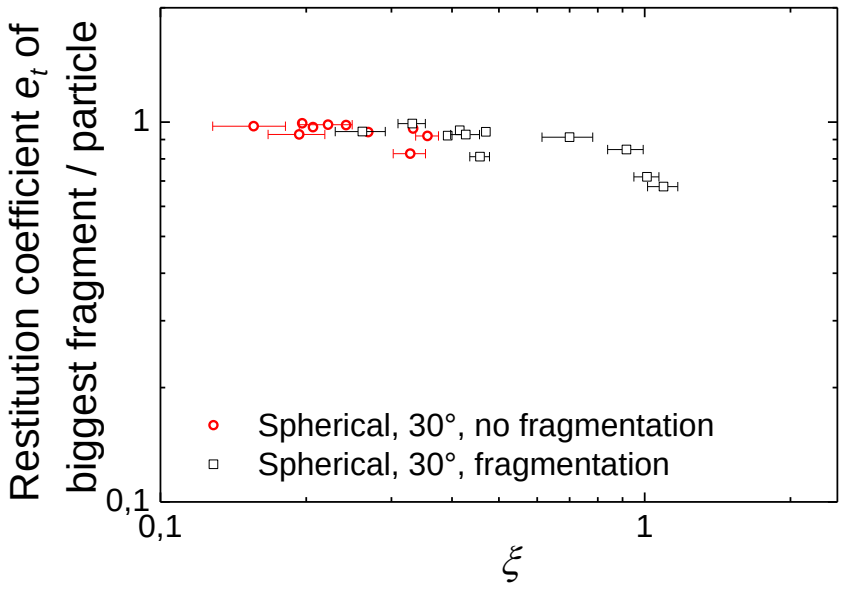

Figure 4-17. Tangential restitution coefficient e_t versus ξ. Impact angle was 30°. In the case of no fragmentation, the mean value of e_t was ~0.95. In the case of fragmentation, the mean value of e_t was ~0.88. Typical error bars are shown for ξ, whereas error bars for e_t were smaller than the symbols.

A mean tangential restitution coefficient close to 1 for oblique impacts in combination with the normal restitution coefficients shown in Figure 4-15 resulted in reduced post-impact angles, as shown in Figure 4-18. Here, the initial impact angle was 30°. In the case of no fragmentation, the mean post-impact angle was approx. 11°. With increasing ξ, the post-impact angle decreased. The function:

$$\alpha_{p,30^\circ} = 4.88\xi^{-0.44}{}^\circ, \quad \text{for } 0.16 < \xi < 1.1 \tag{4-20}$$

illustrates the best fit for the post-impact angle which approximates well the maximum post-impact angles observed by Render & Pan[39] for “perfectly catastrophic” fragmentation. Assuming that $e_t = 1$ and considering Eq. (4-18), the post-impact angle was calculated:

$$\alpha_{p,30^\circ,calculated} = \arctan\left(0.12\xi^{-0.59}\frac{1}{\sqrt{3}}\right)\frac{180^\circ}{\pi}, \quad \text{for } 0.16 < \xi < 1.1, \tag{4-21}$$

which agrees well with the measured post-impact angles (Figure 4-18).

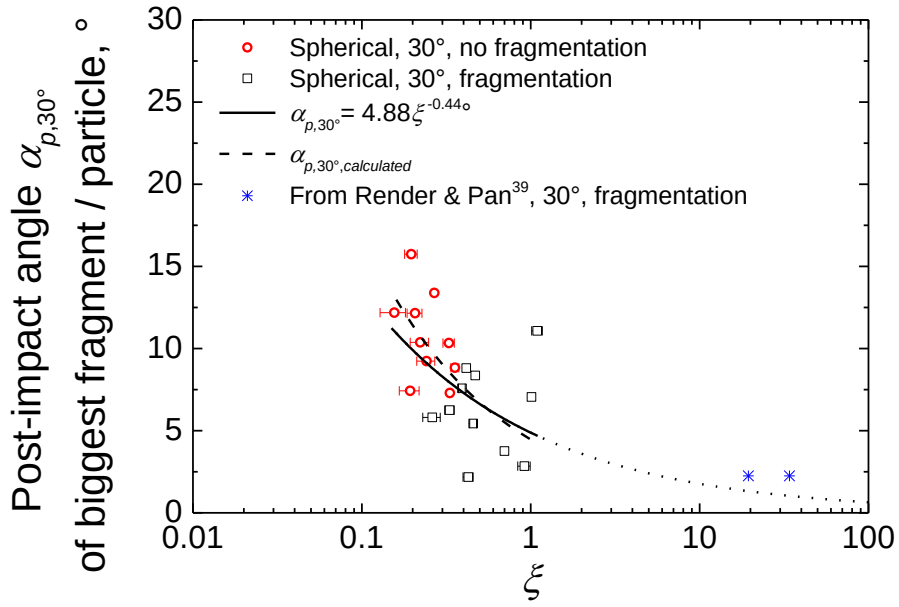

Figure 4-18. Post-impact angle $\alpha_{p,30°}$ versus ξ. Impact angle was 30°. In the case of no fragmentation, the mean post-impact angle was 11°. With increasing ξ, the post-impact angle decreased. The fit agrees well with results from Render & Pan[39]. The measured post-impact angles are well approximated with the calculated post-impact angles $\alpha_{p,30°,calculated}$, assuming that $e_t = 1$. Typical error bars are shown for ξ. Error bars for $\alpha_{p,30°}$ are smaller than the symbols.

4.6.2 Impacts of Non-Spherical Ice Particles

In this section, normal restitution coefficients and post-impact angles resulting from normal impacts of initially non-spherical ice particles are shown.

In Figure 4-19, the normal restitution coefficient versus ξ is illustrated. The restitution coefficient decreased with increasing ξ. The best fit to the data is:

$$e_{n,90°} = 0.11\xi^{-0.33}, \quad \text{for } 0.08 < \xi < 2.1. \tag{4-22}$$

Up to $\xi \approx 0.65$, which includes all no fragmentation impacts, the restitution coefficients were generally smaller for non-spherical particles than for spherical particles (Figure 4-15). In the case of no fragmentation and in contrast to impacting spherical particles, significant post-impact rotational motions of the non-spherical particles were observed. In fact, it is more likely that non-spherical ice particles start to rotate significantly upon impact than spherical ice particles (with small density and shape imperfections).

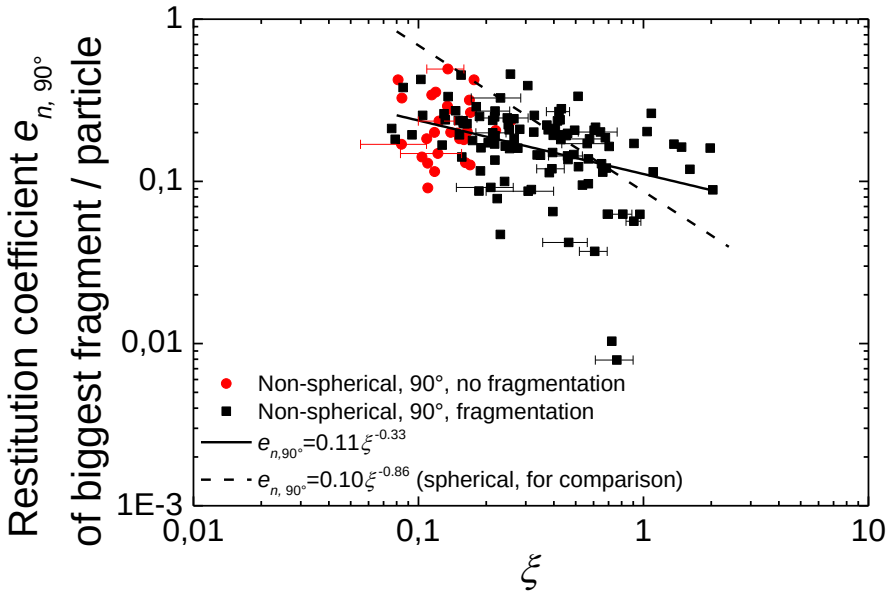

Figure 4-19. Normal restitution coefficient versus ξ including fit. The biggest fragments of originally non-spherical ice particles were analysed. Impact angle was 90°. For comparison with the fragments of spherical ice particles, the fit from Figure 4-15 is shown. Typical error bars are shown for ξ, whereas error bars for e_n were smaller than the symbols.

This is the case since the vector of the reaction force applied on the particle upon impact by the surface will likely be further apart from the centre of gravity in the case of non-spherical particles than in the case of spherical particles. The further the reaction force vector and centre of gravity are apart, the larger is the torque and the more significant the rotational motions are. For the same reason, it was observed that up to $\xi \approx 0.65$, where minor fragmentation dominated (Figure 4-13), the biggest fragments (>80 % of the initial volume) of non-spherical particles experienced significant post-impact rotational motions, whereas the biggest fragments of spherical particles did not. In fact, in the case of a minor fragmentation impact of a spherical particle the impact of the rear part of the sphere, which represents the biggest fragment and which may not be affected by fragmentation, is dampened by the small front part which is affected by fragmentation. However, the fragmentation of the small front part does not necessarily lead to significant torque acting on the rear part.

In the case of non-spherical particles, the rotational motions took up part of the initial kinetic energy (mainly translational energy) leading to decreased normal restitution coefficients in comparison to spherical particles.

For $\xi \gtrsim 0.65$, major and catastrophic fragmentation dominated. A small difference in the normal restitution coefficients between the biggest fragments of initially spherical and non-

spherical particles was observed. However, the data for analysis was relatively scarce, since it was hard to achieve relatively high ξ. It is assumed that for $\xi \gtrsim 0.65$, the restitution coefficients converge since the influence of the initial particle shape diminishes. In fact, significant rotations of the fragments and decreasing impact angles (with increasing ξ) were observed and were independent of the initial particle shapes. Up to date, data from literature for comparison does not exist.

In Figure 4-20, the post-impact angle versus ξ is shown.

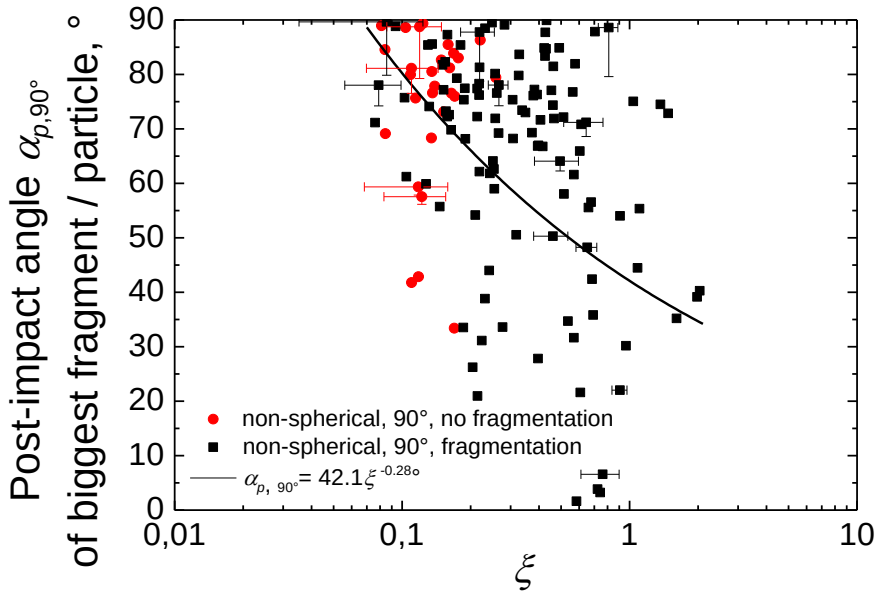

Figure 4-20. Post-impact angle $\alpha_{p,90°}$ versus ξ including fit. Impact angle was 90°. In the case of no fragmentation, the mean post-impact angle was 75°. With increasing ξ, the post-impact angle decreased. Typical error bars are shown.

The mean post-impact angle in the case of no fragmentation was 75°. With increasing ξ, the post-impact angle decreased and was approximated with the following fit:

$$\alpha_{p,90°} = 42.1\xi^{-0.28°}, \quad \text{for } 0.08 < \xi < 2.1. \tag{4-23}$$

The data was strongly scattered which is due to the non-spherical shape and the unknown morphology of each particle. However, it is assumed that for relatively big values of ξ (catastrophic fragmentation), the post-impact angle would approach small values as observed in the case of spherical particles (Figure 4-16). Up to now, there is no data available in the literature for comparison to the presented data.

In section 4.6, it was shown that the parameter ξ, which represents the probability of the fragmentation modes ranging from *no* via *minor* to *major/catastrophic fragmentation* (Figure 4-13), is adequate to describe the post-impact velocities and post-impact angles of the biggest fragments. With the change of the fragmentation mode from *no* ($\xi \lesssim 0.4$) to *major/catastrophic fragmentation* ($\xi > 1.1$), the restitution coefficients and post-impact angles of the original particles (no fragmentation) and biggest fragments (any kind of fragmentation) decreased. The tendencies were independent of the initial particle shape. Best fits to the experimental data were provided which showed good agreement with data from Guégan et al. and Render & Pan, who investigated the impact of spherical ice particles onto solid walls for $\xi > 20$. They investigated *perfectly catastrophic fragmentation*, which represents the upper extreme of *catastrophic fragmentation* defined in this work. For this reason, the post-impact angles and normal restitution coefficients observed in their works represent extreme values ($\alpha_{p,90°} \approx 2°$, $\alpha_{p,30°} \approx 2°$, and $e_{n,90°} \approx 0.02$). The impacts investigated in chapter 4 ($0.07 < \xi < 2.5$) were part of the transition between *no* and *perfectly catastrophic fragmentation*. All kinds of fragmentation were observed except for *perfectly catastrophic fragmentation* as the biggest fragment's volume was at least 10 % of the initial particle volume and fewer fragments were created than observed by Guégan et al. and Render & Pan. The post-impact behaviour of the fragments depends not only on ice particle morphology but also on fragmentation mode and particle shape. For this reason, post-impact angles and restitution coefficients varied significantly in this study in comparison to the studies of Guégan et al. and Render & Pan, where *perfectly catastrophic fragmentation* of spherical ice particles only was investigated.

4.7 Summary and Conclusions

The study was devoted to the experimental and theoretical investigation of ice particle impact onto a flat, rigid target. Spherical and non-spherical ice particles were used in the experiments while the models were developed for a characteristic spherical semi-brittle impactor. Four typical modes of fragmentation were identified in the experiments: no fragmentation, minor, major, and catastrophic fragmentation.

Typical scaling relations describing particle attrition/splitting by lateral cracks and breakup by median/radial cracks were derived capturing the main physics of particle impact onto a rigid target. Analysis of the experimental data showed that the typical velocity for particle splitting describes well the transition from minor to major/catastrophic fragmentation. Particle

splitting is probably the main mechanism leading to major and catastrophic fragmentation. Particle attrition is significant only at relatively small velocities, leading to no fragmentation (in the case of tiny fragments that cannot be resolved) or minor fragmentation together with particle splitting.

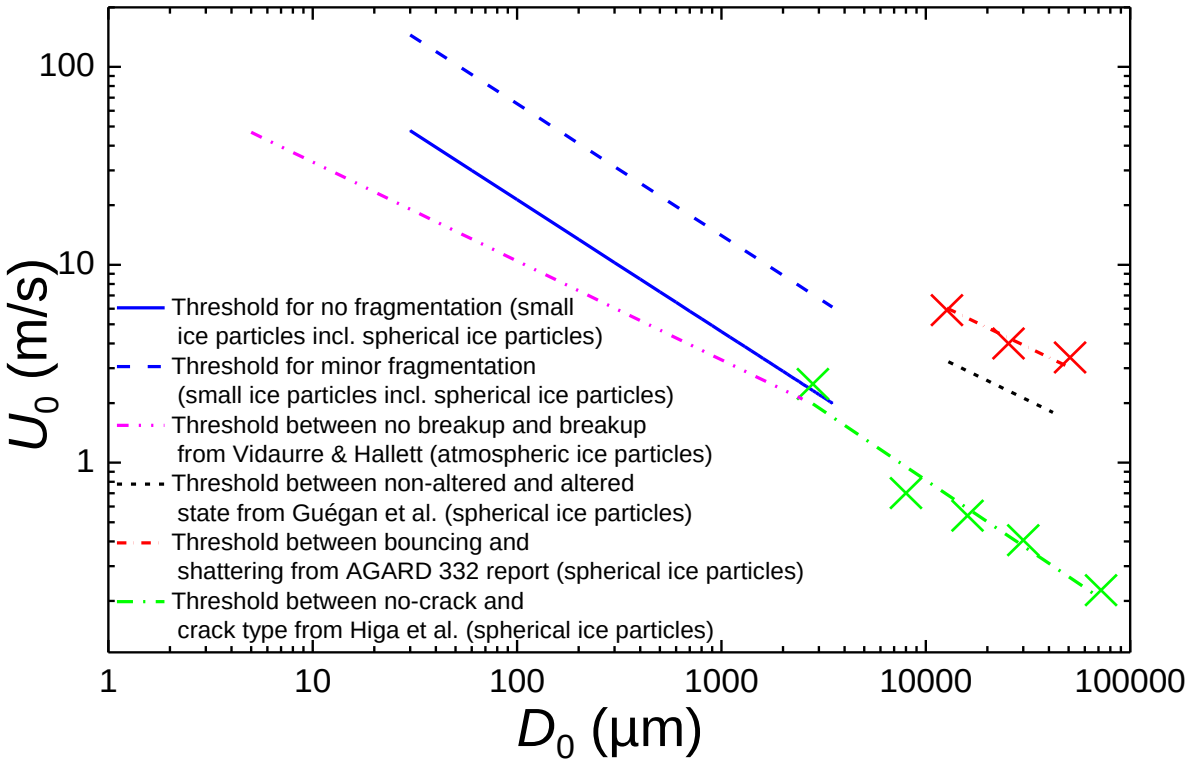

Figure 4-21. No and minor fragmentation thresholds of this study in comparison to thresholds from literature. References are mentioned in the text.

The thresholds for no and minor fragmentation are shown in comparison to different thresholds from the literature (Figure 2-2) in Figure 4-21. The agreement is good between this study's no fragmentation threshold and the thresholds from Vidaurre & Hallett[31] and Higa et al.[30] which investigated (partly) the same diameters. The thresholds from Higa et al. and Vidaurre & Hallett are shifted towards lower velocities in comparison to this study's no fragmentation threshold. In the case of Higa et al., this shift may be explained by the different definition used by the authors for the threshold where visible cracks (and no fragments) were needed only to cross the threshold. In the case of Vidaurre & Hallett, this shift could be explained by 1) the observation of impacting natural, dendritic ice crystals (amongst others) whose branches easily fragmented and 2) better optical resolution (~1 µm/pixel). This study's minor fragmentation threshold is similar to the thresholds from Guégan et al.[34] and from the AGARD 332 report[35] which describe the threshold between the non-altered and altered state

as well as the threshold between bouncing and shattering, respectively. Since the investigations from Guégan et al. and from the AGARD 332 report focused on the investigation of relatively large spherical ice particles, the optical resolutions were most likely lower than in this study. This could be the reason why their thresholds agree well with the *minor fragmentation* - instead of the *no fragmentation* - threshold of this study since small fragments potentially created upon impact in their investigations could not be observed due to lower resolution limits. Moreover, different ice particle generation techniques leading to different, unknown internal structures could have influenced the thresholds for particle fragmentation behaviour.

Furthermore, in this study, probability distributions for minor and major/catastrophic fragmentation were calculated from the experimental data using an empirical dimensionless parameter ξ. This parameter was also used to describe the restitution coefficients and post-impact angles of the original particles in the case of no fragmentation and of the biggest fragments in the case of fragmentation. With increasing ξ, both quantities decreased for initially spherical and non-spherical particles. The fits to the experimental data showed good agreement with data from literature where *perfectly catastrophic fragmentation* of larger spherical ice particles ($D > 2.8\,\mathrm{mm}$, $\xi > 20$) was investigated resulting in hundreds of small fragments.

The presented investigation led to a better understanding of the occurrence of the observed fragmentation modes and of the post-impact behaviour of the fragments (or original particles in the case of no fragmentation). The obtained knowledge allows more accurate simulations of ice particle impact processes, including the post-impact trajectories, onto dry, cold targets, e.g. onto the spinner, fan, or inlet of an aircraft engine. Hence, more accurate predictions of potential ice accretion sites within aircraft engines and probes in glaciated icing conditions are possible.

5 Ice Particle Melting in Forced Convection[§§]

In this chapter, the melting process of non-spherical and spherical ice particles was theoretically and experimentally investigated. Individual ice particles were suspended in an acoustic levitator placed in a chest freezer. Melting of the particles was initiated by directing a warm stream of air with controlled temperature, flow rate, and relative humidity towards them. Tests were conducted at 13 different flow conditions. The melting process was recorded by a high-speed video camera. Datasets of 222 individual melting events were collected. From the images, the melting time and the cross-sectional area of the ice particles during melting were measured. Furthermore, a method was presented which allowed an approximate calculation of the initial mass of the ice particles based on the post-melting evolutions of the cross-sectional area. Theoretical melting times were calculated based on a model for spherical and non-spherical particles and were compared with the experimental melting times. The model was validated with spherical ice particles and its predictions of melting times of non-spherical ice particles agreed very well with the experimental data.

In the next sections, heat and phase change models are introduced and the experimental apparatus allowing for the investigation of the melting process of ice particles under defined flow conditions is described. The melting model is validated with data of melting spherical ice particles and the comparison between the experimental and theoretical melting times of non-spherical ice particles is shown.

5.1 Heat Exchange and Phase Change Models for Melting Ice Particles

In this section, the heat exchange and phase change models for calculating melting times of ice particles under forced convection are introduced. First of all, it is shown how the particle sphericity used in the later applied Nusselt correlation is approximated.

5.1.1 Characteristic Particle Quantities

The *ISO circularity* is the ratio of the perimeter of a circle with equivalent projection area as the particle to the actual perimeter of the projection area:

[§§] This chapter is based on the publication: Hauk, T., Bonaccurso, E., Villedieu, P., and Trontin, P., "Theoretical and Experimental Investigation of the Melting Process of Ice Particles", *Journal of Thermophysics and Heat Transfer*, American Institute of Aeronautics and Astronautics, Reston, USA, Nov. 2015, (submitted).

$$C = \frac{2\sqrt{A_{proj}\pi}}{P}, \text{ where } 0 < C \leq 1 \text{ and,} \tag{5-1}$$

where A_{proj} is the projected area and P is the perimeter of the projected area of the particle. For $C = 1$, the projected area is a circle.

The *area ratio* (*AR*) is the ratio of the actual projected area of the particle to the area of a circle with a diameter equal to the maximum dimension of the projected area (Figure 5-1).

Figure 5-1. Area ratio is the ratio of the projected area of the particle to the area of the red circle. *AR* ≈ 0.25.

ISO circularity and area ratio can be determined by video analysis.

The knowledge of the (initial) particle sphericity is crucial for the application of the heat exchange and phase change models. However, the measurement of the actual surface area of a non-spherical ice particle is hardly possible. For this reason, the (initial) particle sphericity is approximated with two different approaches:

1) Using the crosswise sphericity $\Phi_{\perp}$, which is derived from the particle's projected area.
2) Using a combination of the ISO circularity *C* and area ratio *AR*:

$$\Phi \simeq C^x AR^y, \text{ where } x, y \geq 0 \text{ and,} \tag{5-2}$$

where *C* is the average ISO circularity before melting and *AR* is the average area ratio before melting. x and y are determined from the best fit to the data (shown in section 5.5). The expression for the sphericity considers that it decreases for decreasing average area ratio and decreasing average ISO circularity for a constant

volume. For a spherical particle, C and AR are equal to 1 which leads to $\Phi = 1$. For a non-spherical particle, Φ has a value between 0 and 1.

5.1.2 Heat Exchange Model

Neglecting phase transitions and radiative heat transfer, the general equation describing the convective heat transfer of a particle in air is:

$$m_p \, c_p \, \frac{dT_{p,m}}{dt} = A_p \, h_m \left(T_a - T_{p,s}\right). \tag{5-3}$$

Using the volume-equivalent sphere diameter d_p of the particle, and the particle sphericity Φ, Eq. (5-3) may be re-written as:

$$m_p \, c_p \, \frac{dT_{p,m}}{dt} = \frac{\pi \, d_p^2}{\Phi} \, h_m \left(T_a - T_{p,s}\right). \tag{5-4}$$

To obtain the mean convective heat transfer coefficient h_m, which is linked with the particle Nusselt number Nu_p, the Nusselt number can be calculated with an adequate empirical correlation. For spherical particles, the Frössling[108] correlation reads:

$$\mathrm{Nu}_p = 2 + 0.552 \, \mathrm{Re}_p^{\frac{1}{2}} \, \mathrm{Pr}^{\frac{1}{3}}. \tag{5-5}$$

As pointed out in the work of Villedieu et al.[87], this expression can be extended to non-spherical particles using a formal Reynolds analogy between the friction coefficient and the dimensionless heat transfer coefficient.

The following correlation was proposed by Hölzer and Sommerfeld[109] for the drag coefficient of a generic particle:

$$C_d = \frac{16}{\mathrm{Re}_p} \frac{1}{\sqrt{\Phi}} + \frac{3}{\sqrt{\mathrm{Re}_p}} \frac{1}{\Phi^{3/4}} + \frac{8}{\mathrm{Re}_p} \frac{1}{\sqrt{\Phi_\perp}} + \frac{0.421}{\Phi_\perp} 10^{0.4(-\log(\Phi))^{0.2}}. \tag{5-6}$$

The first two terms in Eq. (5-6) depend on the total surface area of the particle (Φ) and thus correspond to friction drag. The two last ones are related to the projected area ($\Phi_\perp$) and correspond to form drag (pressure gradient effect) and must not be taken into account in the

analogy between heat transfer and friction force. Indeed the Reynolds analogy, which relies on the mathematical analogy between the heat and the momentum transport equations, is strictly valid only for flows without pressure gradient. The general equation of motion of a particle in air can be written as:

$$m_p \frac{d\boldsymbol{v_p}}{dt} = \pi\, d_p\, \mu_a \frac{\mathrm{Re}_p}{8} C_d(\boldsymbol{v_a} - \boldsymbol{v_p}), \tag{5-7}$$

where $\boldsymbol{v_p}$ is the particle velocity vector and $\boldsymbol{v_a}$ is the air velocity vector. Eq. (5-7) is formally similar to the particle heat transfer equation which can be written as:

$$m_p\, c_p \frac{dT_{p,m}}{dt} = \pi\, d_p\, k_a \frac{\mathrm{Nu}_p}{\Phi}(T_a - T_{p,s}). \tag{5-8}$$

The analogy between Eq. (5-7) and Eq. (5-8) shows that the term $\frac{\mathrm{Re}_p}{8} C_d$ formally plays the same role for momentum transfer as the term $\frac{\mathrm{Nu}_p}{\Phi}$ for heat transfer. Using Eq. (5-6) without the latter two terms as explained above, it is thus reasonable to assume the following expression for the Nusselt coefficient of non-spherical particles:

$$\mathrm{Nu}_p \approx 2\sqrt{\Phi} + \frac{3}{8}\Phi^{\frac{1}{4}}\sqrt{\mathrm{Re}_p}. \tag{5-9}$$

This expression does not account for the effect of the Prandtl number which is implicitly assumed to be equal to 1 in the Reynolds analogy. Since our objective is to generalize the Frössling correlation, it is better to finally replace Eq. (5-9) by the following expression which takes into account the influence of the Prandtl number and coincides with the Frössling correlation for spherical particles ($\Phi = 1$):

$$\mathrm{Nu}_p = 2\sqrt{\Phi} + 0.552\, \mathrm{Re}_p^{\frac{1}{2}}\, \mathrm{Pr}^{\frac{1}{3}}\Phi^{\frac{1}{4}} \tag{5-10}$$

5.1.3 Phase Change Model

The modelling of the melting process is based on the work of Villedieu et al.[87] who considered the studies of Mason[52] and Wright et al.[53]. It is assumed that the melting process can be divided into two successive phases. In the first phase, the ice particle is solid and is heated from its initial temperature to the melting temperature T_{melt}, equal to 0 °C. In the second

phase, the particle starts melting at constant temperature $T_p = 0$ °C until all solid ice becomes liquid water. Further assumptions are made in the different phases:

Phase I

- Mass transfer due to sublimation and deposition can occur
- The temperature of the ice particle is uniform ($T_p = T_{p,s} = T_{p,m}$)
- The density of the ice particle is constant

Phase II

- Mass transfer into and from the environment due to evaporation and condensation can occur
- The ice core is completely surrounded by a liquid film
- The particle sphericity progressively increases up to 1
- The liquid layer is at rest
- Shedding of meltwater does not occur
- The density of the ice core is constant

In **Phase I**, the modelling equations are:

$$m_p\, c_{p,i}\, \frac{dT_p}{dt} = \pi\, d_p\, \frac{\mathrm{Nu}_p}{\Phi} k_a \left(T_a - T_p\right) - \dot{m}_{sub}\left[L_f\left(T_p\right) + L_v\left(T_p\right)\right], \tag{5-11}$$

$$\frac{dm_p}{dt} = -\,\dot{m}_{sub}, \tag{5-12}$$

$$\dot{m}_{sub} = \pi\, d_p\, \frac{\mathrm{Sh}_p}{\Phi}\, \rho_a\, D_{v,a}\left[y_{v,s}\left(T_p, p_a\right) - y_{v,a}\right], \tag{5-13}$$

where $c_{p,i}$ is the heat capacity of ice, L_f is the latent heat of fusion of ice, L_v is the latent heat of vaporization of ice, and p_a is the pressure of the airflow. Equations (5-11) and (5-12) describe the particle energy and mass conservation accounting for the sublimation mass rate, determined in Eq. (5-13). The diffusivity of vapour in air is given by Schirmer[110]:

$$D_{v,a} = D_0 \left(\frac{p_0}{p_a}\right)\left(\frac{T_a}{T_0}\right)^{1.81}, \tag{5-14}$$

where $D_0 = 22.6$ E-6 m²/s, $p_0 = 1$ bar, and $T_0 = 273.15$ K. p_a and T_a are the pressure and the temperature of the airflow.

The particle Sherwood number Sh_p, based on the analogy of heat and mass transfer, is:

$$\mathrm{Sh}_p = 2\sqrt{\Phi} + 0.552\ \mathrm{Re}_p^{\frac{1}{2}}\ \mathrm{Sc}^{\frac{1}{3}}\Phi^{\frac{1}{4}}. \tag{5-15}$$

In **Phase II**, the energy conservation equation is:

$$\pi\ d_p\ \frac{\mathrm{Nu}_p}{\Phi}\ k_a(T_a - T_{melt}) = \dot{m}_{ev} L_v(T_{melt}) + \dot{m}_f L_f(T_{melt}), \tag{5-16}$$

where $\dot{m}_{ev}$ is the evaporation rate and $\dot{m}_f$ the melting rate.

The ice core mass evolution rate is given by:

$$\frac{dm_{p,i}}{dt} = -\dot{m}_f = \left[L_f(T_{melt})\right]^{-1}\left[\dot{m}_{ev} L_v(T_{melt}) - \pi\ d_p\ \frac{\mathrm{Nu}_p}{\Phi}\ k_a(T_a - T_{melt})\right], \tag{5-17}$$

where $m_{p,i}$ is the mass of the ice core surrounded by liquid water.

The evolution rate of the total particle mass is described by:

$$\frac{dm_p}{dt} = -\dot{m}_{ev} = -\pi\ d_p\ \frac{\mathrm{Sh}_p}{\Phi}\ \rho_a\ D_{v,a}\left[y_{v,s}(T_p, p_a) - y_{v,a}\right]. \tag{5-18}$$

The mass of the liquid water layer $m_{p,w}$ is given by:

$$m_{p,w} = m_p - m_{p,i}. \tag{5-19}$$

The diameter of the particle can be calculated from considerations of the mass of the liquid layer:

$$m_p = m_{p,i} + \rho_w \frac{\pi}{6}\left(d_p^3 - d_{p,i}^3\right), \tag{5-20}$$

which yields:

$$d_p = \left[\frac{6}{\pi}\left(\frac{m_p - m_{p,i}}{\rho_w} + \frac{m_{p,i}}{\rho_{p,i}}\right)\right]^{\frac{1}{3}}, \tag{5-21}$$

where ρ_w is the density of liquid water.

In the case of non-spherical particles, the particle sphericity increases from its initial value $\Phi_0 < 1$ to 1 according to:

$$\Phi = \left(\frac{m_{p,i}}{m_p}\right)\Phi_0 + \left[1 - \left(\frac{m_{p,i}}{m_p}\right)\right]. \tag{5-22}$$

5.2 Experimental Method

In this section, the experimental apparatus and its components are described. Moreover, an overview of the test conditions, test procedure, and post-processing is presented.

5.2.1 Experimental Apparatus

A top view sketch of the experimental apparatus is shown in Figure 5-2. It consists of an acoustic levitator, aimed to suspend individual ice particles, an optical and recording system to magnify and record the melting particle, and a flow control system to generate a defined airflow. Overall and close-up views of the test apparatus are shown in the Appendix.

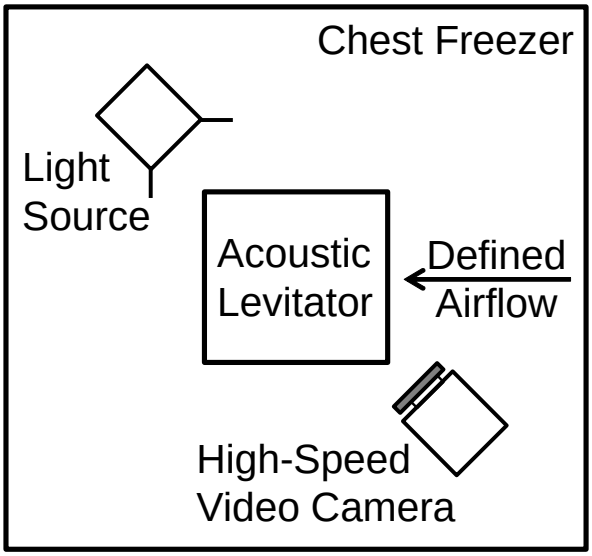

Figure 5-2. Top view sketch of the experimental apparatus for the ice particle melting experiments in a defined airflow. The acoustic levitator, the high-speed video camera and the light source are shown.

5.2.1.1 Acoustic Levitator

The acoustic levitator (tec5 AG, Oberursel, Germany) is placed in a chest freezer to maintain a defined initial ice particle temperature which is assumed to be equal to the surrounding temperature. The levitator mainly consists of an ultrasound transducer with a working frequency of 58 kHz and a concave reflector between which a standing wave is generated. The distance between the transducer and the reflector is set with a micrometre screw (Figure 5-3).

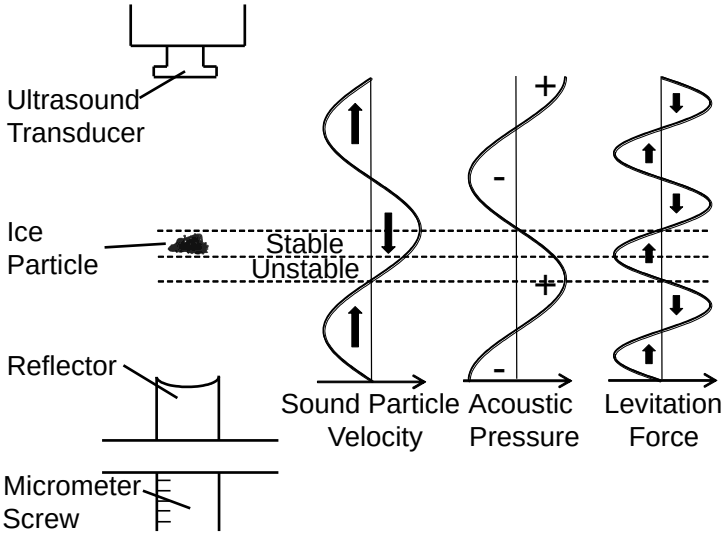

Figure 5-3. Sketch of suspended ice particle in an acoustic levitator and illustration of sound particle velocity, acoustic pressure and levitation force distributions.

The standing wave has several equally spaced nodes and antinodes of sound particle velocity and sound pressure. Due to the axial levitation force and the Bernoulli stress which stabilizes the suspended particles radially, particles with a density in the range of 0.5 to 2 g/cm³ can be levitated just below the pressure nodes in the stable region. The particle size is limited to half a wavelength. The magnitude of the acoustic force can be controlled via a power supply unit. Detailed theoretical descriptions of the working principle of an acoustic levitator can be found in the literature, e.g. in the dissertation of Höppner[111]. The vertical position of the levitator in the chest freezer sets the surrounding and initial ice particle temperature, which is measured by a RTD sensor (Pt100) attached to one of the levitator's rods next to the ice particle's position. A DP9602 high accuracy digital thermometer (OMEGA®, Stamford, USA) is used.

5.2.1.2 Flow Control System

A warm, uniform, and controlled airflow to heat up and melt the ice particle is generated as follows. Pressurised air (RH = 4 % at 1 bar and 20 °C) is initially used. To control the RH of the airflow, the air is passed through several gas washing bottles filled with water. Further downstream the mass flow rate of the pressurised air is controlled with a FMA-2600 mass flow controller (OMEGA®, Stamford, USA). To control the temperature of the airflow, the humidified air is passed through a coil of copper tube immersed in a temperature-controlled water bath. Finally, the warm air flows through a horizontal and thermally insulated aluminium tube with an inner diameter of 15 mm. The tube contains 20 screens which provide a uniform velocity distribution over the cross-section. The tube's open end is located approx. 5 mm away from the levitated ice particle which is positioned on the extended axis of the tube.

A RTD sensor (Pt100) is used for measuring the temperature of the airflow. The RH is measured by a B-530 humidity sensor connected with a GL220 data logger (both from Graphtec Corporation, Yokohama, Japan). The ambient pressure is measured by a pressure transducer system (Aerolab LLC, Laurel, USA).

5.2.1.3 Optical and Recording System

A Phantom® v611 high-speed video camera (Vision Research Inc., Wayne, USA) is attached to an SZX10 microscope (Olympus Corporation, Tokyo, Japan). The microscope and the Dedocool cold light source (Dedo Weigert Film GmbH, Munich, Germany) are placed above the acoustic levitator. Two mirrors placed in gimbal mounts are used to enable the

observation and the illumination of the ice particle suspended in the acoustic field. The angle between the flow vector and the line of sight is approx. 50°. Frame rates ranged from 120 to 250 fps. Typical values of overall resolution, pixel resolution, and exposure time were 752 x 504 pixels, approx. 156 pixels per mm, and 500 µs.

5.2.2 Test Procedure and Conditions

Non-spherical ice particles are collected from the walls of a chest freezer at temperatures between -15 and -25 °C. An ice particle is placed in the acoustic levitator with tweezers cooled to the temperature of the freezer. The vertical position of the test platform inside the chest freezer is adjusted to set the desired initial temperature of the ice particle. The power of the acoustic levitator is set so that the particle will not be blown away by the airflow and the final liquid droplet will be spherical. The flow velocity and temperature are set by adjusting the mass flow controller and the water bath temperature. The RH is controlled by the number of gas washing bottles and their water levels. The insulated aluminium tube is kept outside of the cooling chamber until steady-state airflow conditions are reached. Then, the tube is placed in its mount next to the ice particle and the melting process is recorded by the high-speed video camera.

To generate a spherical ice particle, a non-spherical ice particle is melted until approx. 90 % of its mass is liquid. Then, the warm airflow is removed and the refreezing of the particle usually occurs within seconds due to the residual ice core acting as a seed for crystallization. After some more seconds, the ice particle temperature is equal to the surrounding temperature and the melting process can be initiated.

In total, 222 melting processes were recorded. The airflow parameters were varied to reproduce 13 different conditions, which are similar to the conditions found within the first stages of a typical low pressure jet engine compressor[***]. The experimental (and theoretical) melting times were obtained. At each condition, a small number of spherical ice particles were melted, followed by several melting processes of non-spherical particles. The different test conditions are listed in Table 5-1.

[***] RH was varied to allow the validation of the melting model in a wide range and to investigate the effect of evaporative cooling.

Table 5-1. Test conditions of the 222 melting processes.

Condition [-]	Initial ice particle temperature [°C]	Ambient pressure [mbar]	Flow temperature [°C]	Flow velocity [m/s]	Relative humidity [%]	Number of tests - spherical/ non-spherical [-]
1	-16.7	0.954	20.0	1.0	4	4/15
2	-18.2	0.963	20.0	1.22	4	6/6
3	-17.5	0.952	15.0	0.75	63	5/17
4	-16.7	0.954	20.0	1.0	74	4/22
5	-18.0	0.953	25.0	1.25	3	7/4
6	-17.8	0.953	25.0	0.75	3	6/10
7	-18.7	0.953	25.0	0.75	44	6/13
8	-18.1	0.954	25.0	1.25	40	6/15
9	-17.4	0.955	25.0	1.75	36	4/11
10	-17.8	0.954	25.0	1.75	3	4/11
11	-18.1	0.954	30.0	1.25	2	5/11
12	-17.6	0.954	30.0	1.25	40	4/11
13	-17.2	0.954	20.0	1.25	56	4/11

5.2.3 Post-Processing

The post-processing of the recorded melting processes was done with an in-house MATLAB code. The flow chart summarizing the post-processing is illustrated in Figure 5-4.

Before the post-processing, the relevant video had to be manually analysed to set the start and end frames of the video sequence (including pre- and post-melting images) and the melting process only. As a result, several plots were obtained and relevant data such as melting time, initial mass, etc. were stored in an Excel file.

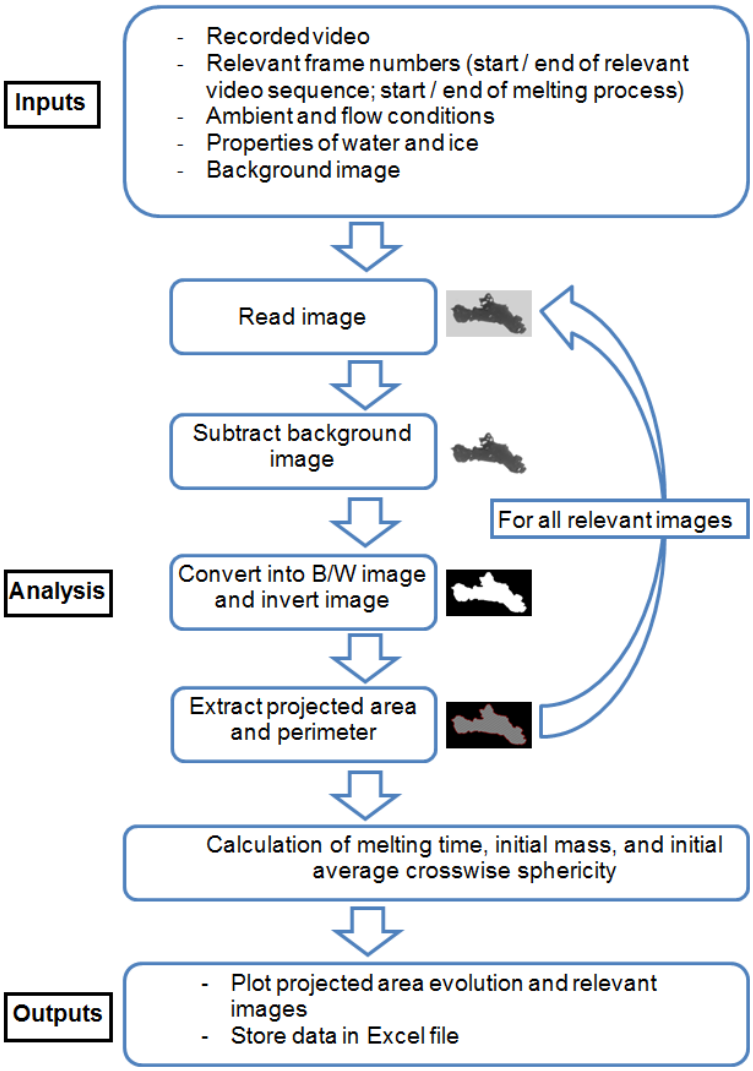

Figure 5-4. Flow chart illustrating the post-processing routine.

5.3 Observations of Ice Particle Melting

In this section, typical ice particle shapes and a method for the calculation of the initial ice particle mass are presented.

5.3.1 Ice Particle Shapes and Properties

Pictures of eight ice particles showing the maximum and minimum projected areas before melting, as well as the corresponding final liquid droplets, are shown in Figure 5-5. The non-spherical ice particles were aggregations of several smaller ice particles or crystals.

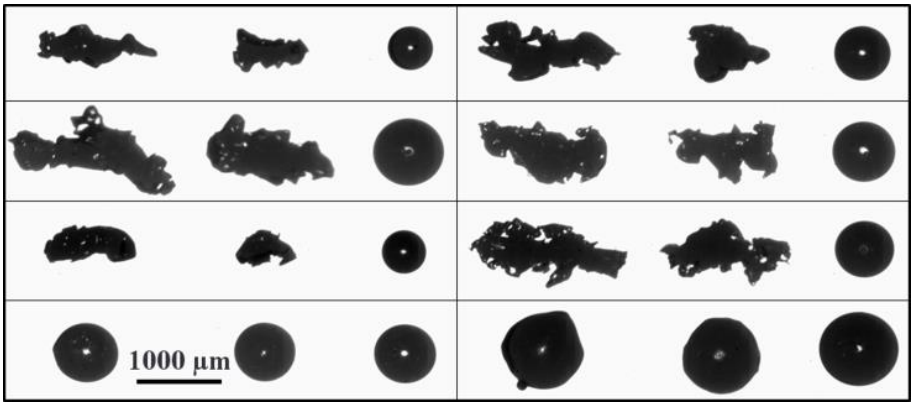

Figure 5-5. Shapes of eight typical ice particles before and after melting. Each box shows three different views of the same particle. 1st view: largest projected area before melting; 2nd view: smallest projected area before melting; 3rd view: final liquid droplet after melting.

The maximum dimension of the non-spherical ice particles placed in the acoustic levitator varied between 730 and 3,490 µm. The initial mass of the ice particles, which was extrapolated from the volume of the final water droplet and its evaporation/condensation rate, was between 2.5 E-5 and 59 E-5 g. Mass vs. diameter of all non-spherical ice particles is shown in Figure 5-6.

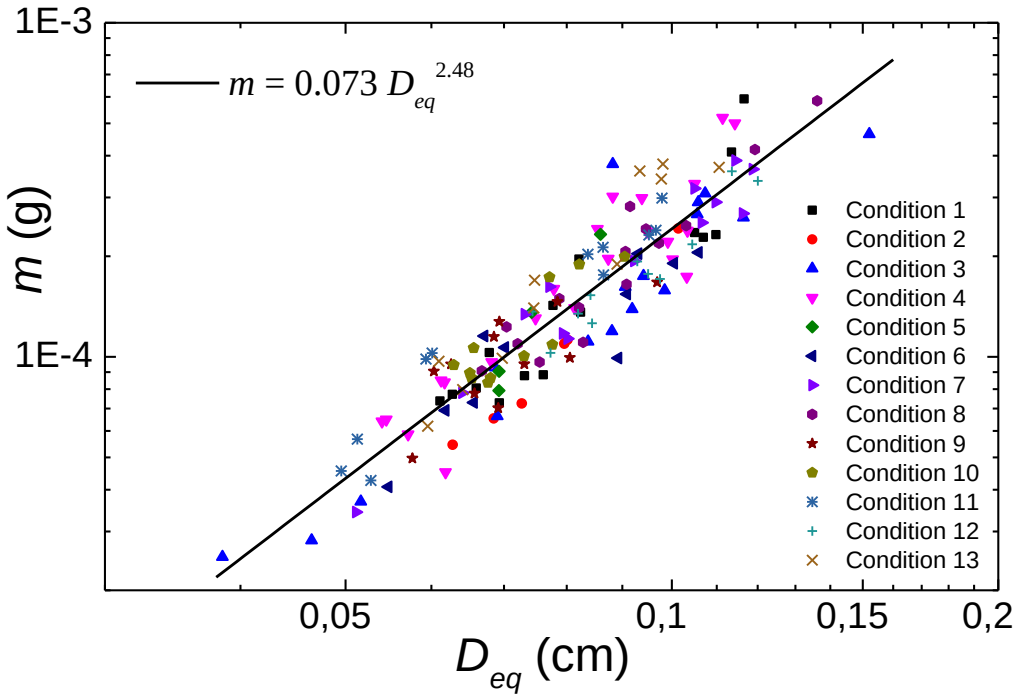

Figure 5-6. Mass vs. area-equivalent diameter of the mean projected area before melting of all non-spherical particles used in this study. The solid line represents a power law fit to the data.

D_{eq} represents the area-equivalent diameter of the mean projected area $A_{m,proj}$ before melting defined as:

$$D_{eq} = \sqrt{\frac{4A_{m,proj}}{\pi}}. \tag{5-23}$$

The mass-size relationship:

$$m = \alpha D_{eq}^{\beta} \tag{5-24}$$

is applied in atmospheric research to characterize sampled ice particles. α and β are constants. The common units g and cm were used for the mass and the area-equivalent diameter, respectively. For the non-spherical ice particles analysed in this study, the best fit to the data shown in Figure 5-6 led to $\alpha = 0.073$ and $\beta = 2.48$.

The spherical ice particles, generated by refreezing melted non-spherical ice particles, had a maximum dimension ranging from 570 to 1,290 µm. Their initial mass varied between 6.8 E-5 and 69 E-5 g. The spherical ice particles (lower part of Figure 5-5) showed some minor surface irregularities. Similar irregularities have been observed for all ice particles generated by refreezing.

5.3.2 Calculation of the Initial Particle Mass

An important parameter for the calculation of the melting time, according to the model introduced in section 5.1, is the initial mass of the ice particle. Due to sublimation, deposition, evaporation and condensation, the mass of the final liquid droplet, which can be derived from the measurement of the projected area, is usually not equal to the initial mass of the ice particle. Moreover, volume and density of the original ice particle are unknown. Due to these uncertainties, a method was established which allows to determine the initial mass more accurately.

Under the assumption that, during the melting process, the mass transfer rate between the particle and the flow is comparable to the evaporation/condensation rate of the liquid droplet after the melting process, the initial mass of the ice particle can be calculated on basis of the so-called d^2-law[112–114]. Ice sublimation (due to the absence of a liquid water film) or deposition (at high RH) during the first phase of particle melting is not separately considered

here because the initial heating phase is short compared to the overall melting time (less than approx. 10 %) and only a negligible mass is lost.

Non-spherical ice particles have a larger surface area than spherical ice particles of comparable mass and have thus an increased mass transfer rate during the melting process. Not knowing the exact surface area of each particle, the simplifying assumption is made that all particles have a surface area equivalent to that of a sphere. The d^2-law predicts that the square of the diameter of a spherical droplet during evaporation/condensation changes at a constant rate K given by:

$$\frac{d\,(d^2)}{dt} = K, \tag{5-25}$$

where d is the droplet diameter, t is the time, and K is a constant.

The instantaneous projected area of the droplet is given by the following equation:

$$\frac{\pi\, d^2}{4} = \frac{\pi\, d_0^2}{4} - \frac{\pi\, K}{4}\, t = \frac{\pi\, d_0^2}{4} - K_p t, \tag{5-26}$$

where K_p is the projected area rate constant and d_0 is the initial droplet diameter. To calculate the initial projected area of a droplet under the influence of evaporation/condensation for a certain time t, which is equal to the melting time t_{melt}, K_p must be determined. For this reason, the evolution of the projected area of the liquid droplet is measured for several more seconds after the completion of the melting process. The knowledge of this evolution allows calculating the projected area rate constant K_p by the application of the ordinary least squares method. Then, the projected area of the hypothetical initial droplet, which is assumed to have the same mass as the initial ice particle, can be calculated with:

$$\frac{\pi\, d_0^2}{4} = \frac{\pi\, d_{em}^2}{4} + K_p t_{melt}, \tag{5-27}$$

where d_{em} is the diameter of the droplet at the end of the melting process.

The initial mass of the liquid droplet $m_{droplet,0}$ and, hence the initial mass of the ice particle $m_{p,0}$ is:

$$m_{p,0} = m_{droplet,0} = \rho_w \frac{1}{6} \pi \, d_0^3 \tag{5-28}$$

In the case of conditions 1, 2, 5, 6, 10, and 11, where RH was smaller than 5 %, the initial mass was on average between 13.6 % and 19.7 % larger than the final mass (Table 5-2).

Table 5-2. Mean relative differences between initial and final mass for all conditions including their standard deviations.

Conditions	**1**	**2**	**3**	**4**	**5**	**6**	**7**	**8**	**9**	**10**	**11**	**12**	**13**
Mean relative difference between extrapolated initial mass and mass of final liquid droplet [%]	17.3	19.7	-0.4	0.0	17.2	15.4	1.2	1.8	3.6	15.9	13.6	2.3	0.3
Standard deviation [%]	4.7	2.5	1.9	1.4	4.1	2.9	1.2	1.3	1.3	1.9	3.0	0.9	1.1

These differences could be traced back to the relatively strong evaporative cooling effect which was present at these flow conditions. In the case of conditions 3, 4, 7, 8, 9, 12, and 13, where the RH was between 36 % and 74 %, both evaporation and condensation could be observed. In the case of prevailing evaporation, the initial mass was on average up to 3.6 % larger than the final mass. In the case of predominant condensation, the initial mass was on average 0.4 % smaller than the final mass. These rather small differences between the initial and final mass outline a significantly reduced mass transfer rate at larger RH values. A comparison between the extrapolated initial mass and the mass of the final droplet is shown in Figure 5-7. The illustrated conditions 2 and 3 represent the extreme cases with respect to the mean relative difference values (Table 5-2). All other conditions exhibit, depending on the RH of the flow, comparable tendencies and errors.

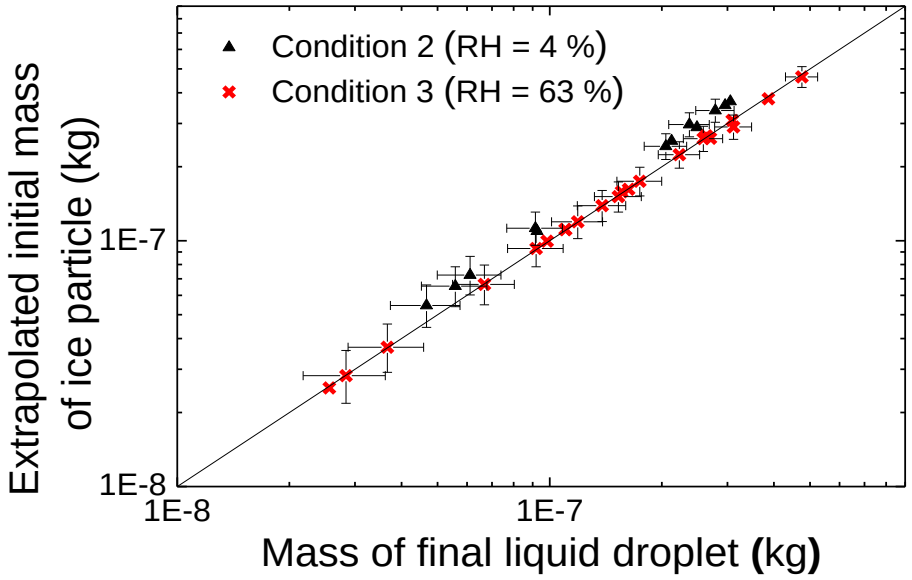

Figure 5-7. Extrapolated initial mass of the ice particles vs. mass of the final liquid droplets including typical error limits. The solid line has a slope of 1 and serves as a guide for the eye. Results for conditions 2 and 3 are shown.

In Figure 5-8, the evolution of the projected area of an ice particle during melting at low flow RH (condition 2) is shown, including pictures of the melting ice particle.

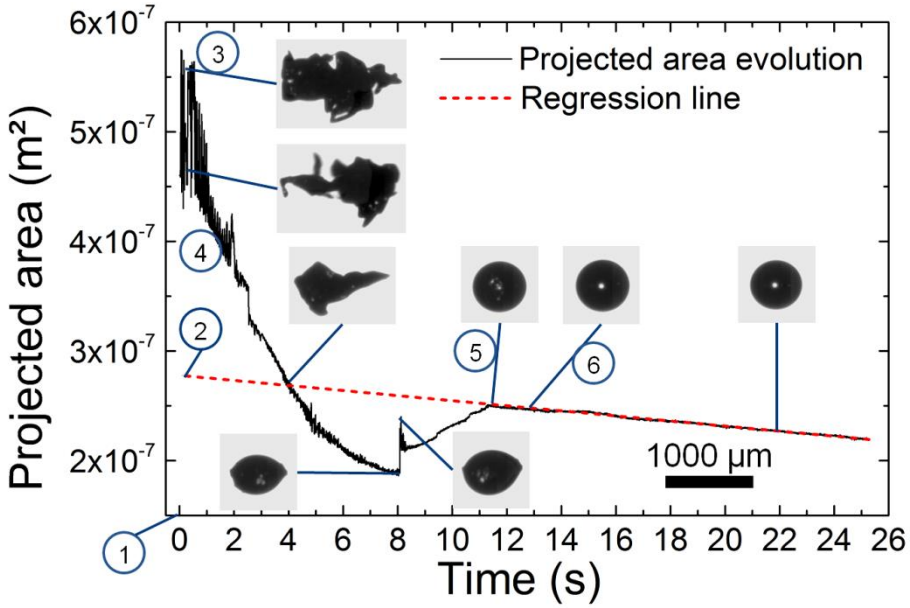

Figure 5-8. Evolution of the projected area during the melting process at low RH (condition 2); 1 – start of video recording, 2 – extrapolated initial projected area, 3 – rotational movements, 4 – shaking movements, 5 – first spherical shape, 6 – end of melting process; to determine K_p the evolution between $t = 13$ s and $t = 25$ s has been taken into account.

The ice particle rotates before melting starts due to asymmetrical acoustic forces acting on the non-spherical particle. Melting starts 0.1 s after the start of the video recording. Within some milliseconds, the first changes in the particle shape can be observed due to the build-up of a meltwater film on the particle's surface. Within the first seconds, the ice particle stops its rotational movements due to the increasing aerodynamic forces dominating over the asymmetrical acoustic forces and shows either almost no movement or some shaking movements around its vertical axis. Then, the projected area reaches a minimum and increases again until the first spherical shape is reached. The existence of a minimum can be explained by the 50° angle between the flow vector and the line of sight, and the orientation of the ice particle whose broadside is aligned perpendicular to the flow. That means that a significant amount of mass can remain hidden to the observer until it accumulates in liquid form in the centre of the particle and, finally, increases its projected area. This process can occur quite abruptly as can be seen at $t = 8$ s. When the first spherical shape is reached and the ice core is completely surrounded by meltwater, the ice core starts to rotate and its diameter continuously decreases until it is completely melted. Due to the low RH of the flow (RH $\sim$ 4 %), the projected area of the nearly spherical droplet decreases linearly with time after melting. As shown before, extrapolating the final nearly linear part of the curve back to the start of the melting allows to obtain the initial ice particle mass. The case shown in Figure 5-8 is representative for almost all recorded melting processes (except for the slope of the final linear part of the curve which depends on the RH of the flow). Only in few cases, continuous rotational movements were observed which lasted from the start of the melting process till the time when the first spherical shape occurred. However, the angular velocity of the particles compared to the flow velocity was sufficiently small so that a significant influence of the rotational movements on the heat transfer and on the melting time were not observed.

5.4 Model Validation

To quantitatively compare the results in sections 5.4 and 5.5, the mean value of the relative differences of the theoretical and experimental melting times $\bar{\Delta}_{rel}$ is introduced:

$$\bar{\Delta}_{rel} = \left(\sum_{n=1}^{n_{total}} \frac{|t_{melt,exper,n} - t_{melt,theo,n}|}{t_{melt,exper,n}} \right) / \, n_{total}, \tag{5-29}$$

where $t_{melt,theo,n}$ is the theoretical melting time and $t_{melt,exper,n}$ is the experimental melting time of melting process n. n_{total} is the total number of the relevant melting processes.

For the validation of the melting model presented in section 5.1, the almost spherical ice particles of each condition, which exhibit sphericity values close to 1, have been considered only. A comparison between the experimental and theoretical melting times of all 13 test conditions is shown in Figure 5-9.

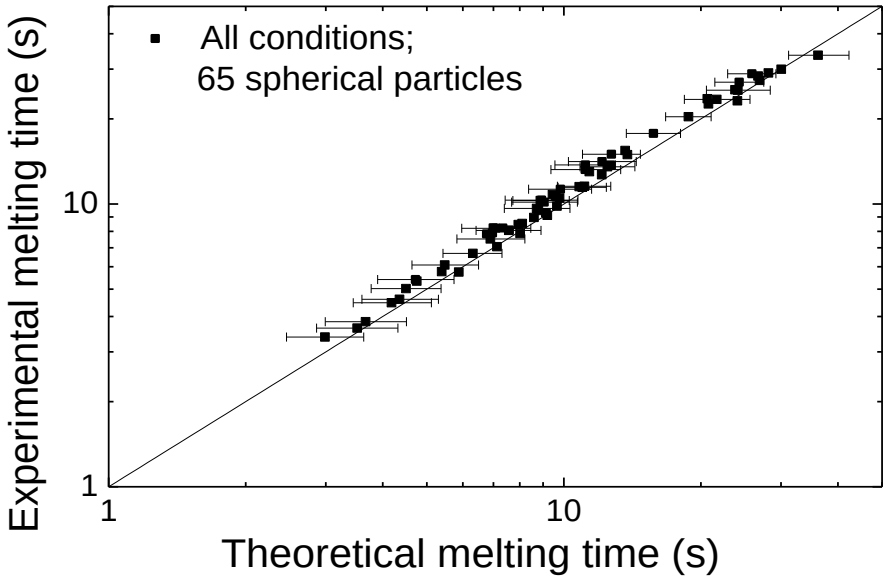

Figure 5-9. Experimental and theoretical melting times of all 13 test conditions with error bars – spherical particles only.

The comparison comprises 65 melting processes in total. The error limits of the different quantities as flow temperature, flow velocity etc., used to calculate the error bars of the theoretical melting times, are illustrated in Table 5-3. The error limit of the experimental melting time is estimated to be ±0.4 s and is not displayed in Figure 5-9 due to its negligible size compared to the total times recorded. In general, there is an excellent agreement between the theoretical and experimental melting times for the considered spherical ice particles. In only one out of 65 melting processes, the experimental melting time is significantly larger than the theoretical melting time, i.e. the error bars of both times do not overlap. The mean value of the relative differences is 8.1 %.

Table 5-3. Error limits of relevant quantities.

Quantity	Error limit
Flow temperature	Variable[†]
Flow velocity	±5 %
Flow relative humidity	±5 % if RH > 10 %, else ±1 %
Ambient/initial particle temperature	±0.5 K
Ambient pressure	±140 Pa
Final diameter	±32 µm

[†]Error limit is variable and depends, besides the calibration errors of the RTD element and measurement device (±0.2 K), on the cooling of the flow during melting. In most cases, it is between ±0.2 and ±0.3 K.

In comparison to the existing errors, the possible effect of inner and outer acoustic streaming[115] on the heat and mass transfer rates, which is induced by the acoustic field, cannot be resolved and is therefore neglected. Seaver et al.[116,117] investigated droplet evaporation using an acoustic levitator placed in a free-jet wind tunnel under similar flow conditions (0.25 m/s < v < 3.5 m/s). The authors concluded that no significant influence of the acoustic field on evaporation could be observed.

5.5 Experimental and Theoretical Melting Times of Non-Spherical Ice Particles

In Figure 5-10, the experimental melting times of 157 non-spherical ice particles are shown and compared to the theoretical melting times of assumed spherical ice particles ($\Phi = 1$). Theoretical melting times overestimated experimental melting times significantly in 31 out of 157 cases. The mean value of the relative differences was 19.9 %.

In Figure 5-11, the experimental and theoretical melting times calculated with the model introduced in section 5.1, under the assumption that the sphericity can be approximated with the crosswise sphericity (1st approach), are shown. Conditions 1 and 4 are shown separately to outline the effect of evaporative cooling. Flow parameters at conditions 1 and 4 were identical except for the RH (4 % vs. 74 %). Average values of the initial ice particle mass and crosswise sphericity were almost identical at conditions 1 and 4, but melting times at conditions 1 and 4 differed by approximately one order of magnitude. The reason is the effect of evaporative cooling which played a major role in condition 1 and increased the melting times significantly due to the low RH of the flow.

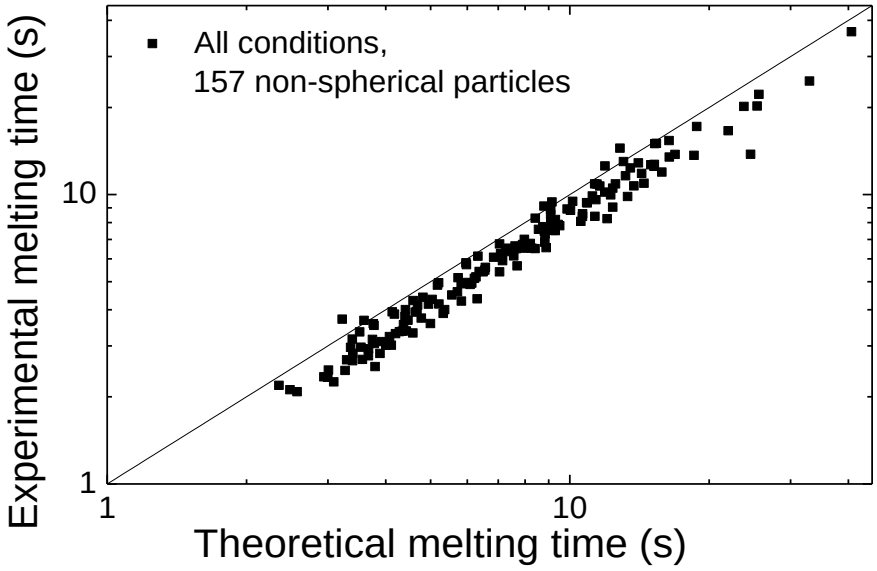

Figure 5-10. Experimental and theoretical melting times for all 13 test conditions assuming $\Phi = 1$ – non-spherical particles only.

Considering all the conditions in Figure 5-11, very good agreement between the theoretical and experimental melting times was reached. Taking into account the errors which were based on the same assumptions presented in section 5.4, only 5 out of 157 non-spherical particles showed significantly larger or smaller theoretical melting times than measured.

In the case of the simplifying assumption ($\Phi = 1$) $\bar{\Delta}_{rel}$ was 19.9 % whereas the application of the melting model, which takes particle crosswise sphericity into account, causes $\bar{\Delta}_{rel}$ to decrease to 9.7 %, which corresponds to an improvement by 51 %.

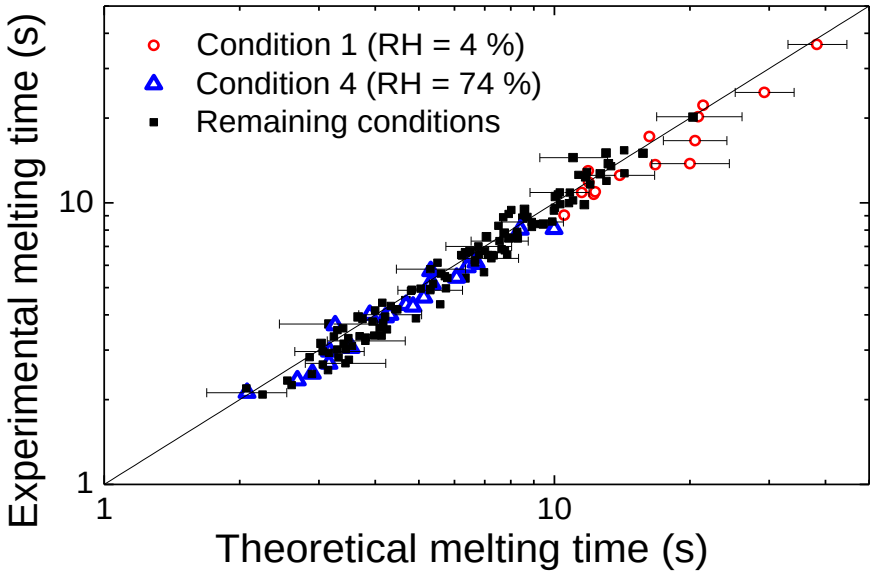

Figure 5-11. Experimental and theoretical melting times for all 13 test conditions with typical error bars considering $\Phi \simeq \Phi_{\perp}$ – non-spherical particles only.

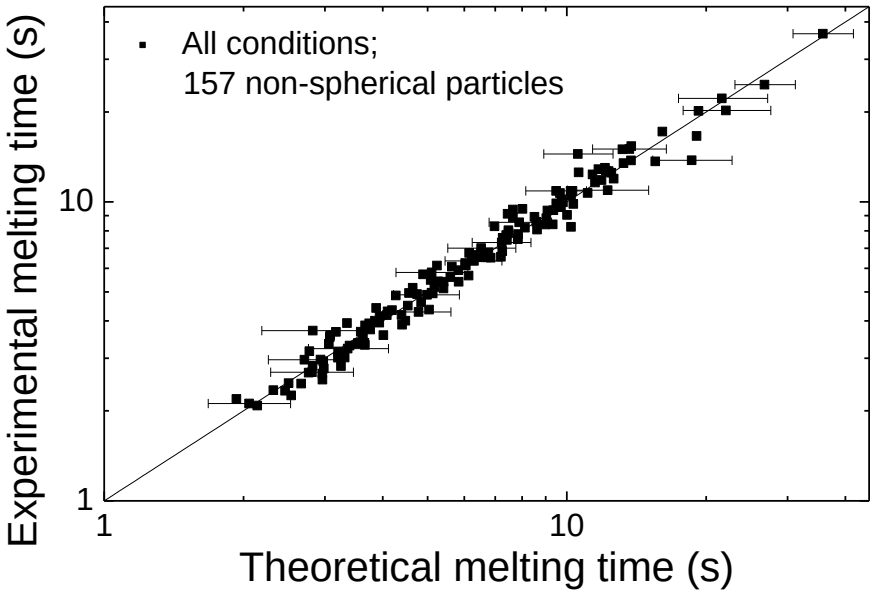

Figure 5-12. Experimental and theoretical melting times for all 13 test conditions with typical error bars assuming $\Phi \simeq C^{0.6}AR^{0.3}$ – non-spherical particles only.

In Figure 5-12, the experimental and theoretical melting times, which were calculated under the assumption that the sphericity can be approximated with a combination of the ISO circularity and area ratio (2nd approach), are shown. For all conditions, the exponents of C and AR were set to 0.6 and 0.3, respectively, to obtain the minimum value of $\bar{\Delta}_{rel}$, which was

6.8 %. Moreover, only 3 out of 157 ice particles exhibited experimental melting times which differed significantly from the theoretical melting times. Hence, the 2nd approach illustrates an improvement by 65.8 % with respect to the assumption of spherical ice particles and an improvement of 29.9 % with respect to the 1st approach, in which the particle crosswise sphericity was used.

The mean value of the relative differences of the theoretical and experimental melting times still has a noticeable magnitude which can be traced back to the existing experimental error limits and most likely to the unknown true particle sphericity which could only be approximated.

5.6 Summary and Conclusions

A test apparatus based on an acoustic levitator was built which allowed the detailed investigation of freely suspended, individual spherical and non-spherical melting ice particles under controlled airflow conditions. A model for the melting of (non-)spherical ice particles was presented which describes the melting process as succession of two phases and takes particle sphericity into account. To determine the initial mass of the ice particle before melting, a new method based on the d^2-law for drop evaporation was introduced. This method allowed the extrapolation of the initial mass from the mass of the final liquid droplet, the projected area rate constant measured after the melting process, and the melting time. Experiments under 13 different airflow conditions with 65 almost spherical and 157 non-spherical ice particles were performed. It was observed that the RH of the flow had a significant influence on the mass transfer during melting and on the melting time. The introduced melting model could be successfully validated by using almost spherical ice particles. Theoretical and experimental melting times showed excellent agreement. The mean value of the relative differences of the theoretical and experimental melting times was 8.1 % and in only 1 out of 65 melting processes this difference was significant.

With respect to the non-spherical ice particles, the application of the introduced melting model led to a major improvement in the calculation of the theoretical melting times by the approximation of the particle sphericity with two different approaches. In comparison to the assumption of a spherical shape, the mean value of the relative differences of the theoretical and experimental melting times was decreased by 51 % (from 19.9 % to 9.7 %) approximating the particle sphericity with the crosswise sphericity (1st approach). In this case,

in only 5 out of 157 melting processes (instead of 31 out of 157 under the assumption of a spherical shape) the difference between the melting times was significant.

With the 2nd approach, where the particle sphericity was approximated with a combination of the ISO circularity and area ratio, the mean value of the relative differences was decreased by 65.8 % (from 19.9 % to 6.8 %). Only 3 out of 157 ice particles exhibited experimental melting times which differed significantly from the theoretical melting times.

In conclusion, it was shown that the consideration of the particle sphericity, approximated by two different approaches, led to a major improvement of the predicted melting times of non-spherical ice particles. Both approaches solely use quantities (crosswise sphericity, ISO circularity, and area ratio) which can be measured by common optical aircraft probes used in flight test campaigns. In contrast to Nusselt correlations applied for non-spherical particles, which use both the sphericity and crosswise sphericity, e.g. the one from Richter & Nikrityuk[50], the recently derived Nusselt correlation from Villedieu et al.[87] uses only one sphericity definition, which allows easier approximation with measurable quantities.

Applying this recent correlation, it is possible to more accurately predict the melting process of ice particles in forced convection. Hence, with respect to ice crystal icing, the LWC to TWC ratio as well as the mass of ice particles upon impact onto structures within aircraft engines can be calculated with higher accuracy allowing a better prediction of icing severity.

6 Impact of Ice Particles onto a Thin Water Film

During flight through ice crystal icing conditions, (partially melted) ice particles may impact onto engine surfaces covered with water droplets or thin water films. The ice particle's inertia as well as viscous and capillary forces acting during contact between the ice particle and the liquid may significantly influence the probability of *sticking*, *bouncing*, and *fragmentation*.

In the case of *sticking*, the ice particle sticks to the water film and contributes to potential ice accretion. There is no fragmentation.

In the case of *bouncing*, the ice particle leaves the potential ice accretion zone after impact and does not contribute to ice accretion. Fragmentation does not occur. Bouncing of an ice particle (blue circle) upon impact onto a slushy layer is shown in Figure 6-1.

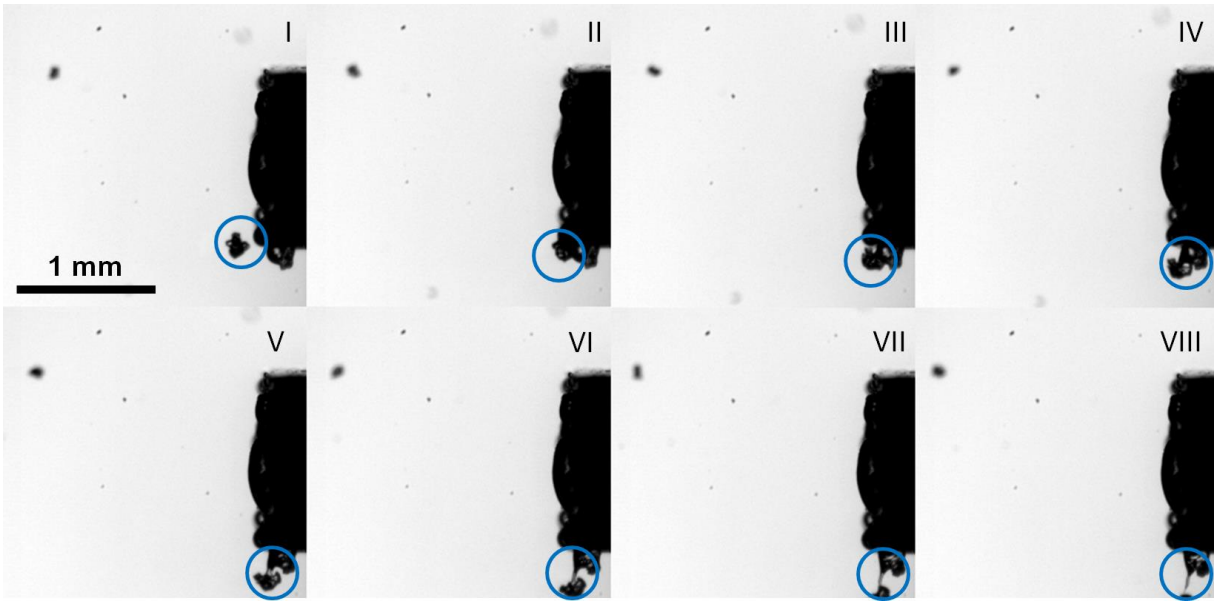

Figure 6-1. Impact of an ice particle (blue circle) with a maximum dimension of ~180 µm onto a slushy layer. The sequence has been recorded shortly after the sequence shown in Figure 3-10. In frames V - VIII, the formation of a liquid bridge and its final breakup can be seen. Time step between frames is 14.9 µs.

This sequence stems from the exploratory experiments presented in chapter 3. After the ice particle's impact onto the slushy layer, a liquid bridge was formed. However, capillary forces were not strong enough to keep the ice particle attached to the slushy layer. It left the potential ice accretion zone and did not contribute to ice accretion.

In the case of *fragmentation*, both bouncing and sticking of the fragments may occur and, hence, the ice particle's fragments may (partially) contribute to ice accretion.

To more accurately predict ice accretion, a test apparatus was developed and, as a first step, data of spherical ice particle impacts onto thin water films was acquired. In total, 237 particle impacts were recorded. The diameter of the ice particles was in the range from 1.18 to 3.52 mm. Impact velocity and film thickness were varied from 1.2 to 5.8 m/s and from approx. 130 to 600 µm. In the following, the test apparatus is described and typical ice particle impacts are shown. At the end of this chapter, results are presented.

6.1 Experimental Method

Generating a thin ($H < 1$ mm), smooth water film of known and constant thickness over time in a subfreezing environment, which prevents the ice particles from melting before impact, is a challenging task. In an above freezing environment, a thin liquid film can be established by using a certain amount of water covering a known surface area. However, in a subfreezing environment, the water film would freeze within a short time. Heating the surface area might prevent the liquid from freezing. However, a problem would remain: the evaporation of the film might lead to a significant reduction of the film thickness making it crucial to measure the actual film thickness before each test with scales or other methods. To easily generate a controllable thin film, another method was applied. A hydrophilic steel sphere with a diameter of $D_0 = 50$ mm was located in a chest freezer (Figure 6-2). A clearance hole with a diameter of 8 mm reached from the south to the north pole of the sphere. Using a water mass flow controller (ANALYT-MTC, Messtechnik GmbH, Mülheim, Germany), the mass of water entering the sphere's south pole and spreading horizontally in all directions along the sphere's surface at the north pole was regulated. Thus, the film thickness could be controlled. It was assumed that due to the relatively low curvature of the steel sphere, which had a diameter of 50 mm, in comparison to the curvature of the spherical ice particles the results would not significantly deviate from results obtained with a water film of the same thickness running down a vertical flat steel surface. No significant waviness of the water film was observed (Figure 6-3). Next to the hydrophilic steel sphere a spring mechanism was located in the chest freezer (Figure 6-2). Instead of using the particle ejection module, presented in chapter 4, a spring mechanism was used for ice particle acceleration. (The particle ejection module, using compressed air for acceleration, would have disrupted the smooth, thin water film at the impact location.) The spring mechanism allowed setting a certain impact velocity within ±0.5 m/s manually. The maximum impact velocity was 6 m/s.

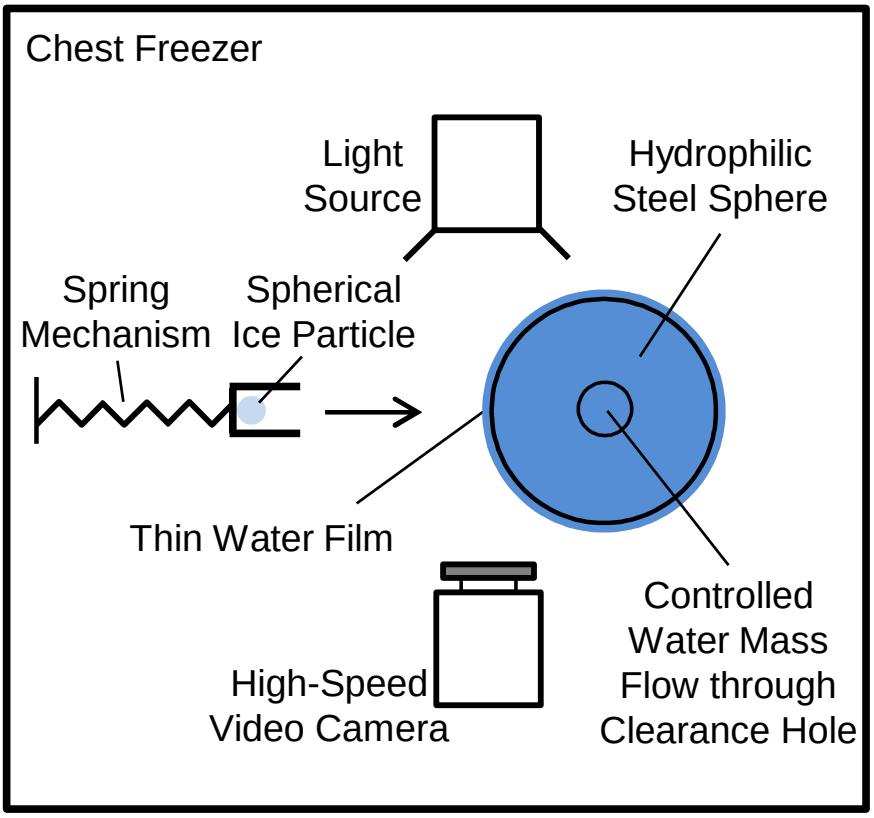

Figure 6-2. Test apparatus, located in a chest freezer, for spherical ice particle impact tests onto a water film with controllable thickness (top view). The spring mechanism for ice particle acceleration, the high-speed video camera and the light source as well as the hydrophilic steel sphere with the clearance hole are shown. Water mass flow controller, funnel, and waste water reservoir are not shown.

A high-speed video camera (Photron Fastcam SA1.1, Photron Europe Limited, West Wycombe, UK) was used to record a side view of the impact process.

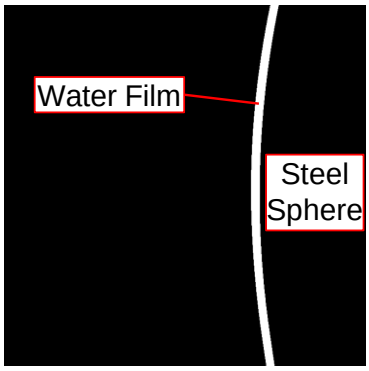

Figure 6-3. Illustration of the water film (white; side view) close to the equator after post-processing. Water film thickness is measured 0.1 ms before impact at the impact location.

A cold light source (Dedocool, Dedo Weigert Film GmbH, Munich, Germany) was used for illumination. A funnel, located below the steel sphere, routed the waste water into a reservoir (not shown). The water film temperature was ~20 °C. The frame rate of the high-speed video camera was 10,000 fps. The size of the frames was 768 x 768 pixels and the resolution was 12.72 µm/pixel. The exposure time was 50 µs. The spherical ice particles were generated from water droplets deposited on a superhydrophobic surface with a contact angle of ~160° placed in the chest freezer (Figure 6-4). They were collected from the superhydrophobic surface with a cold brush. The ice particles' temperatures before impact were in the range from -5 °C to -15 °C.

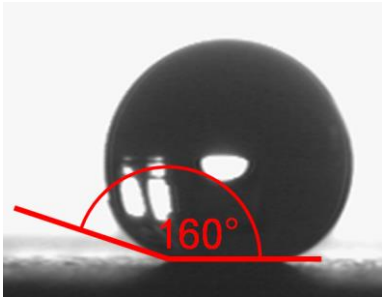

Figure 6-4. Typical water droplet ($D_0 \approx 3$ mm) on superhydrophobic surface before freezing. The contact angle is shown.

The videos were post-processed with MATLAB to obtain the actual impact velocity U_0, which is the velocity of the spherical ice particle at first contact with the water film. Moreover, the diameter of the spherical ice particle as well as the actual film thickness were derived from the videos. To measure the film thickness, a frame of the dry sphere and a frame of the wet sphere, recorded 0.1 ms before impact, were subtracted. The film thickness was measured at the actual impact location with an uncertainty of ±2 pixels. The uncertainty of the impact velocity was about ±1 % and the uncertainty of the spherical ice particle's volume was less than ±10 % (less than ±2 % due to possible deviations from the perfect spherical shape plus less than ±8 % due to the uncertainty of the diameter of ±2 pixels). Overall and close-up views of the test apparatus are shown in the Appendix.

6.2 Sticking, Bouncing, and Fragmentation Impacts

The impacts of the spherical ice particles onto thin water films were categorized into *sticking*, *bouncing* and *fragmentation*. Typical impacts representing these categories are shown in the following. In the cases of sticking and bouncing, the duration of the impact process was

determined as follows: the start of the impact process was defined as the spherical ice particle's first contact with the liquid film; the impact process ended if either the spherical ice particle re-established contact with the steel sphere or the liquid bridge broke up.

Sticking

In Figure 6-5, a spherical ice particle with a diameter of 2.18 mm and an impact velocity of 1.73 m/s impacted onto a water film with a thickness of approx. 230 µm. During rebound, a capillary bridge formed between the spherical ice particle and the water film. The capillary forces finally pulled the spherical ice particle back into the water film. The ice particle stuck to the water film and slowly moved downwards due to gravity and the downwards motion of the film whose average velocity was of the order of 0.1 m/s.

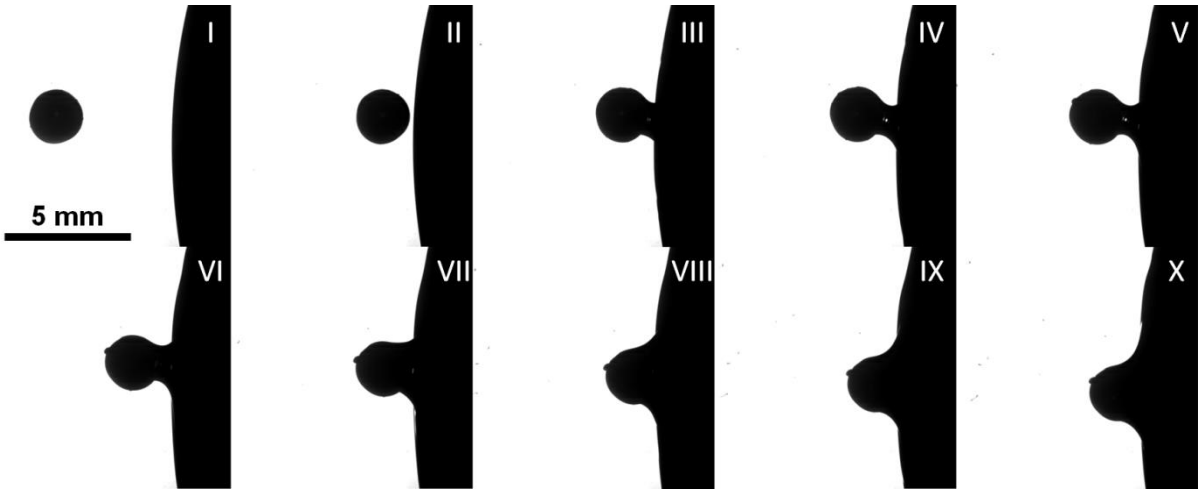

Figure 6-5. Sticking of spherical ice particle. $U_0 = 1.73$ m/s; $D_0 = 2.18$ mm; $H \approx 230$ µm; time step between frames is 2.0 ms. Impact duration: 11.2 ms.

Bouncing

In Figure 6-6, the impact velocity and diameter of the spherical ice particle were 2.41 m/s and 2.85 mm. The water film thickness was approx. 220 µm. During rebound, a liquid bridge was formed which was elongated by the spherical ice particle travelling away from the water film. Finally, the liquid bridge broke up and part of the liquid contained in the liquid bridge remained on the surface of the spherical ice particle.

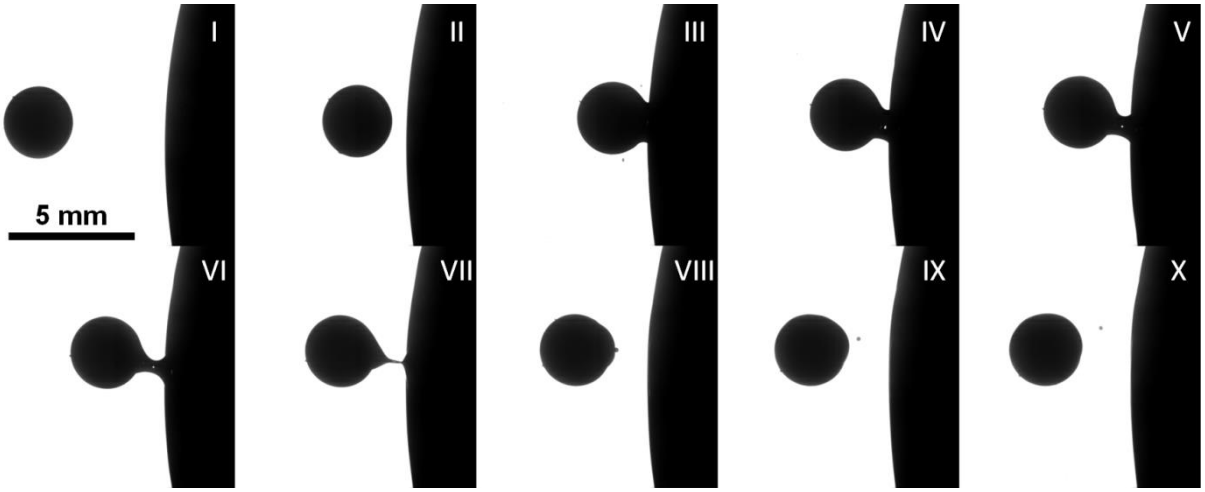

Figure 6-6. Bouncing of spherical ice particle. $U_0 = 2.41$ m/s; $D_0 = 2.85$ mm; $H \approx 220$ µm; time step between frames is 1.3 ms. Impact duration: 6.4 ms.

Fragmentation

In Figure 6-7, the impact velocity was 5.53 m/s and the diameter of the spherical ice particle was 2.60 mm. The water film had a thickness of approx. 600 µm. Upon impact, the spherical ice particle broke up into (at least) three relatively big fragments which adhered to the water film. At least one small fragment (blue circle; frame II) escaped and did not remain in contact with the water film. The fragments, which adhered to the water film, were observed sliding downwards along the surface.

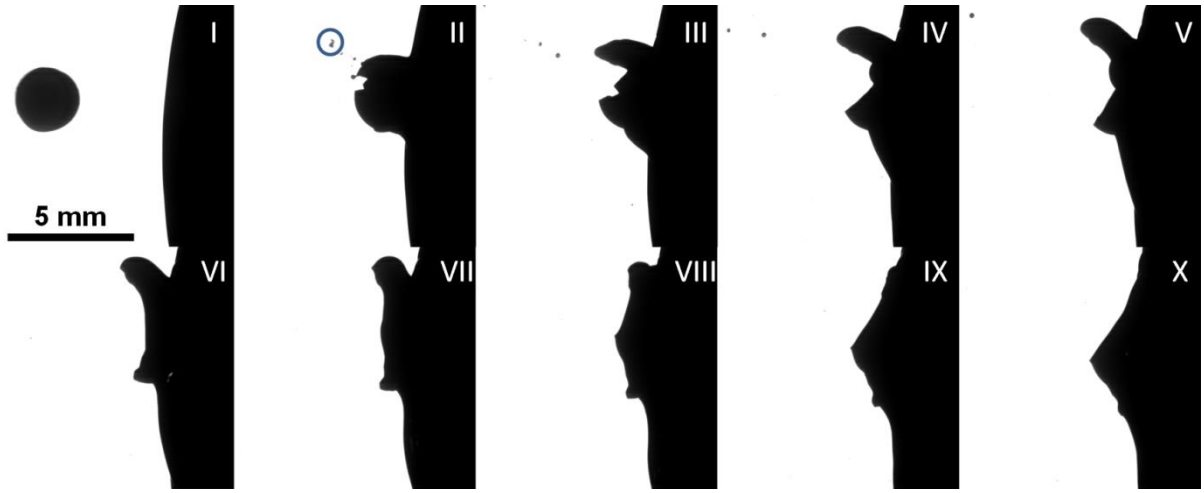

Figure 6-7. Fragmentation of spherical ice particle. $U_0 = 5.53$ m/s; $D_0 = 2.60$ mm; $H \approx 600$ µm; time step between frames is 1.4 ms.

It was observed that the capillary bridges, which formed in the case of sticking and bouncing during rebound, deviated from their ideal symmetrical shape the more, the thicker the water film was (Figure 6-8). Deformed liquid bridges were observed for $H \gtrsim 350$ µm.

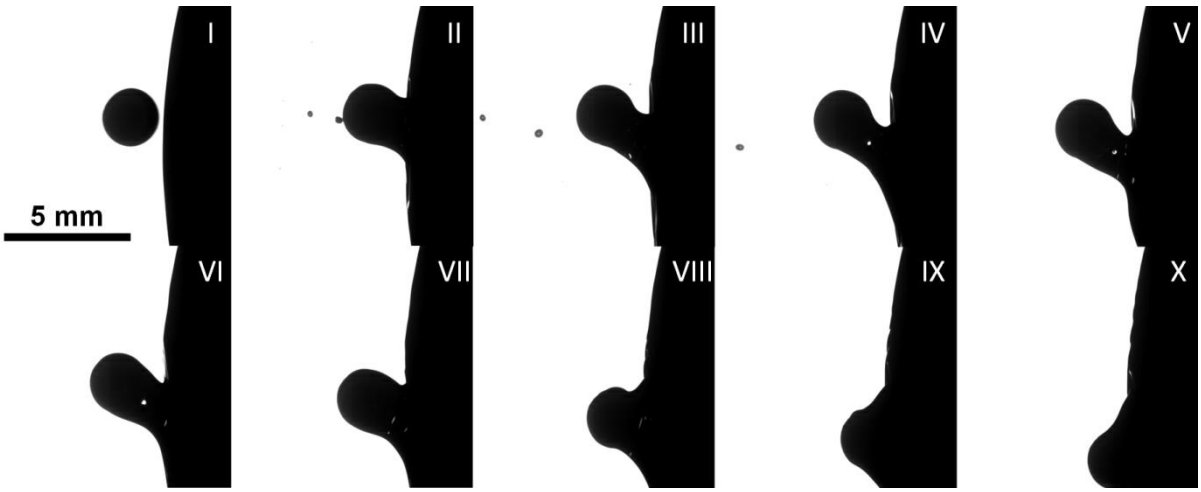

Figure 6-8. Sticking of spherical ice particle. A significantly deformed liquid bridge can be seen. $U_0 = 4.61$ m/s; $D_0 = 2.28$ mm; $H \approx 500$ µm; time step between frames is 2.0 ms. Impact duration: 16.4 ms.

Two effects significantly contribute to the build-up of a deformed capillary bridge:

1) The thicker the liquid film, the longer the impact process may last due to the potential formation of a more voluminous liquid bridge which is able to make the spherical ice particle reattach to the steel sphere even if the distance between the ice and steel spheres is temporarily relatively large during rebound (sticking). In the case of bouncing, the more voluminous liquid bridge may be elongated more than in the case of a less voluminous liquid bridge thus increasing the duration of the impact process. During these prolonged impacts, the downward moving water films may significantly deform the liquid bridges.

2) The velocity of the free surface as well as the average velocity of a downward moving film is higher in the case of a thicker water film compared to a thinner water film, which results in a more deformed liquid bridge. In fact, a thin water film of thickness 600 µm at the equator of the steel sphere is smaller than the thickness of the laminar boundary layer of a hypothetical steady, 2D water flow (or thick film) at the same position under comparable conditions. The thickness of the laminar boundary layer of

a hypothetical steady, 2D water flow at the equator can be approximated with a steady, 2D water flow over a *flat plate* which travels the same distance x (Figure 6-9).

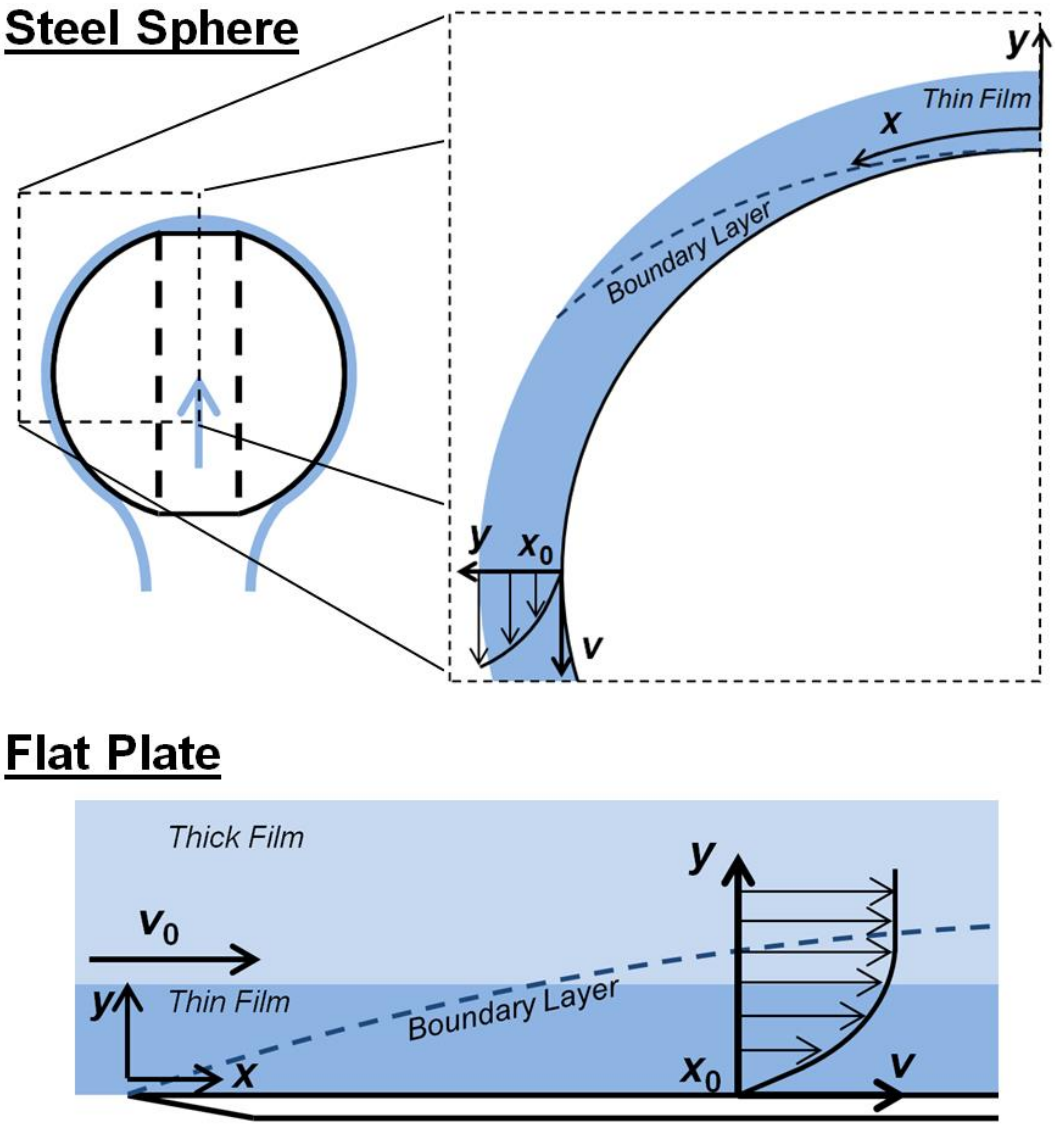

Figure 6-9. Upper part: detail view of a thin film flowing from the north pole of the steel sphere to its equator and beyond. The approximate velocity profile at the equator (at position x_0) and the growing (laminar) boundary layer are shown.
Lower part: the (laminar) boundary layer within a thin and thick film over a flat plate under comparable conditions is shown. The velocity profile at position x_0 is shown.

This distance is equal to one fourth of the circumference of the steel sphere: $x_0 = 0.039$ m. The freestream velocity v_0 of the water flow over the flat plate is assumed to be equal to the maximum velocity of the hypothetical steady, 2D water flow at the equator. Since the water flow originates from the north pole, it can reach a

maximum velocity of 0.71 m/s at the equator due to the vertical distance of ~0.025 m between the north pole and the equator. The maximum flow velocity can be calculated by setting the potential energy equal to the kinetic energy.

The thickness δ of the laminar boundary layer of a steady flow over a flat plate was derived by the German fluid dynamics physicist Paul Richard Heinrich Blasius (1883-1970) and is given by:

$$\delta = 5.0 \frac{x}{\sqrt{\mathrm{Re}_x}}, \tag{6-1}$$

where Re_x is the Reynolds number based on the distance x. For a water flow, which has a temperature of 20 °C and a velocity of $v_0 = 0.71$ m/s, the laminar boundary layer thickness is $\delta \approx 1.2$ mm at $x_0 = 0.039$ m.

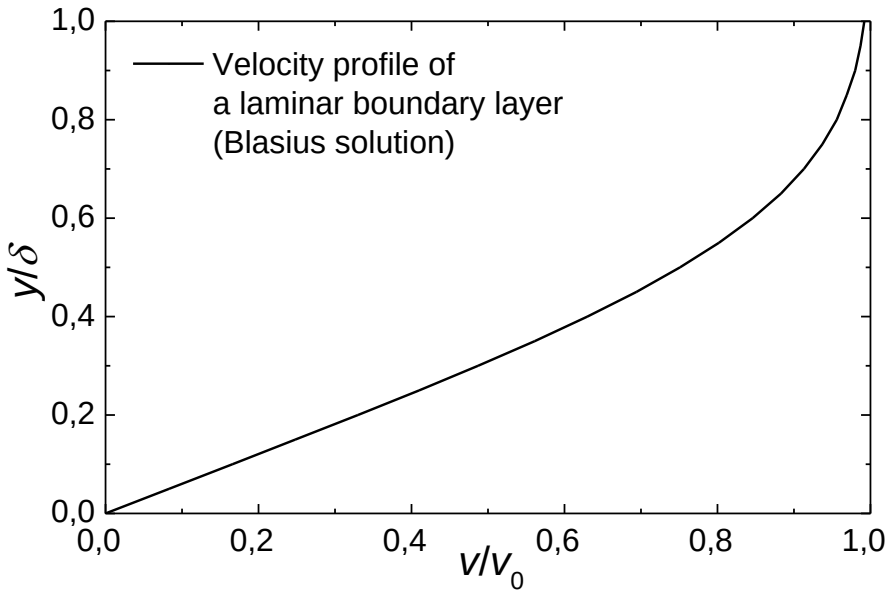

Figure 6-10. Velocity profile of a laminar boundary layer of a steady flow over a flat plate (Blasius solution).

The typical velocity profile of a laminar boundary layer perpendicular to the flat plate is shown in Figure 6-10. $\frac{v}{v_0}$ is the ratio of the flow velocity within the boundary layer to the freestream velocity. $\frac{y}{\delta}$ defines the location of interest within the boundary layer perpendicular to the flat plate.

As can be seen in Figure 6-10, the flow velocity within a laminar boundary layer increases significantly with increasing distance from the flat plate. For example, for a boundary layer thickness of $\delta = 1.2$ mm, the flow velocity is approx. two times higher at $y_2 = 500$ µm compared to $y_1 = 200$ µm. This is why it is finally assumed that the free surface's velocity as well as the average velocity of the thin water film at the steel sphere's equator increases significantly for increasing thickness as long as its thickness is smaller than the laminar boundary layer thickness of a comparable water flow. These higher velocities which occur for thicker thin films may also lead to significant deformations of the liquid bridges.

Both aforementioned effects contribute to a significant deformation of the liquid bridge. For example, the liquid bridge in the sticking case shown in Figure 6-5 was close to symmetrical. The film thickness was 230 µm. The impact duration was 11.2 ms and the water film moved approx. 1.2 mm downwards during impact (on average). In contrast to that, the liquid bridge was significantly deformed in the sticking case shown in Figure 6-8. The likely causes are the longer impact duration (16.4 ms) and the larger film thickness (500 µm) resulting in a downward movement of the water film during impact of approx. 3.8 mm (on average). In general, significantly deformed liquid bridges were observed for $H \gtrsim 350$ µm.

6.3 Results

In total, 237 processes of spherical ice particles impacting onto thin water films were analysed. In the following analysis, no fragmentation, which includes the sticking and bouncing modes, and fragmentation are distinguished. In Figure 6-11, the parameter α, which was defined in Eq. (4-14), versus the dimensionless film thickness H/D_0 is shown for each impact[†††]. The dashed line marks the border ($\alpha = 0.046\ \mathrm{m^{5/3}s^{-1}}$) up to which no fragmentation occurred in the case of dry wall impacts (chapter 4.4). It can be seen that the presence of a relatively thin water film ($0.05 < \frac{H}{D_0} < 0.25$) prevented fragmentation to occur for $\alpha > 0.046\ \mathrm{m^{5/3}s^{-1}}$.

[†††] The sticking and bouncing cases are marked separately in Figure 6-11. However, the occurrence of the one or the other mode is not analysed, since it is not clear how the forces acting on the spherical ice particles during rebound are influenced by possible non-reproducible deformations of the liquid bridges. Thus, the influence of such a deformed liquid bridge on sticking and bouncing is not clear and its analysis is regarded as beyond the scope of this work. In contrast to that, the liquid bridge is not important for the analysis of no fragmentation and fragmentation, since it does not occur during the spherical ice particle's short travel (<0.5 ms) through the liquid film to the steel sphere.

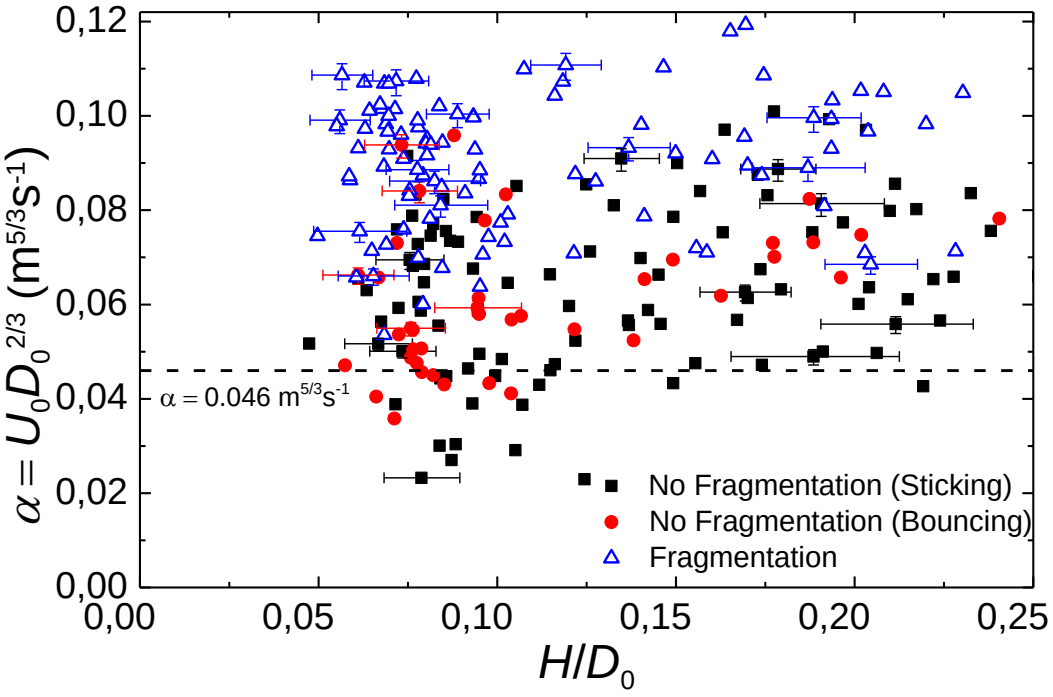

Figure 6-11. The parameter α, defined in Eq. (4-14), versus the dimensionless film thickness H/D_0 is shown. No fragmentation (sticking/bouncing) and fragmentation are distinguished. The maximum no fragmentation value of α (dashed line) for dry wall impacts is shown as a reference. Typical error bars are shown.

The maximum value of α at which no fragmentation occurred was $\sim 0.10\ \mathrm{m^{5/3}s^{-1}}$. The maximum no fragmentation velocity for a spherical ice particle impacting onto a thin liquid water film with thickness between 130 and 600 µm is approx. two times higher than for the same ice particle impacting onto a dry wall. This observation can be rationalized with viscous and capillary forces slowing down the ice particle and dampening its impact onto the steel sphere.

In Figure 6-12, the probabilities of no fragmentation and fragmentation versus α for different intervals of H/D_0 are shown. The width of the α bins was $0.02\ \mathrm{m^{5/3}s^{-1}}$ and the interval width of H/D_0 was 0.05. There was the tendency that for a certain α the probability of fragmentation decreased with increasing dimensionless film thickness. For example, for $\alpha = 0.09\ \mathrm{m^{5/3}s^{-1}}$ (short dash line) the probability of fragmentation decreased from 84 % ($0.05 \leq \frac{H}{D_0} \leq 0.1$) via 50 % ($0.1 < \frac{H}{D_0} \leq 0.2$) to 33 % ($0.2 < \frac{H}{D_0} \leq 0.25$).

There is no simple explanation for this result due to the complexity of the ice particle impact process onto a liquid film. Again, this result can be traced back to capillary and viscous forces

acting during the ice particle's movement through the water film. The tendency is clear: the thicker the water film (ceteris paribus), the more viscous and capillary forces slow down the ice particle before impact onto the steel sphere and the higher the probability of no fragmentation. Modelling of this complex process is left for future work.

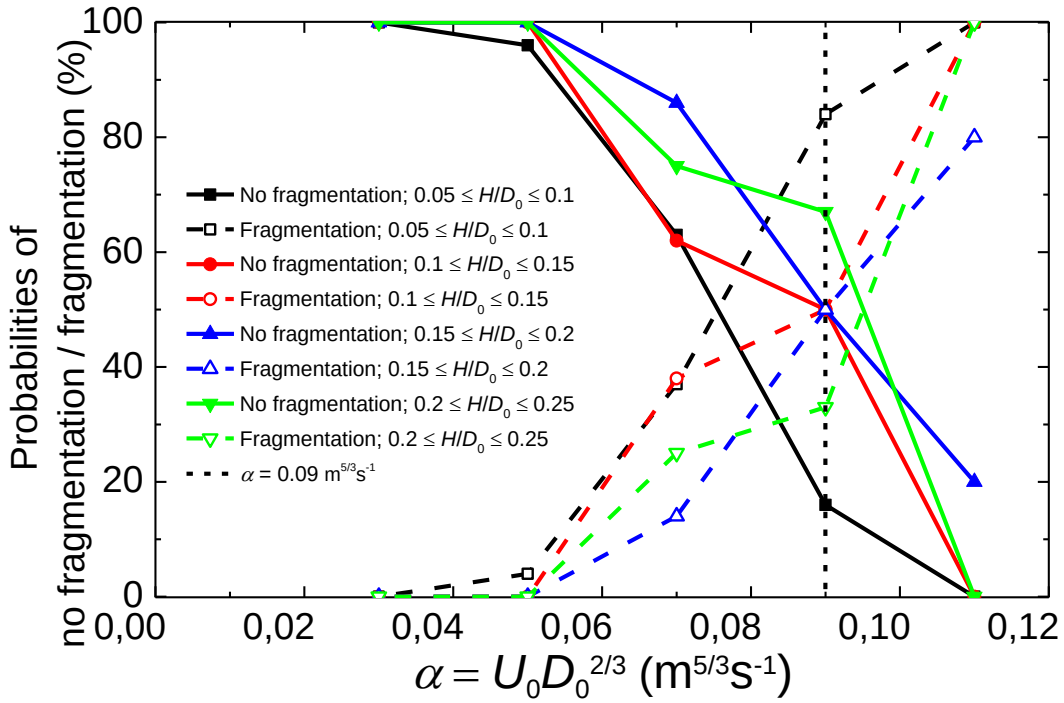

Figure 6-12. The probabilities of no fragmentation and fragmentation versus α for different intervals of H/D_0 are shown.

6.4 Summary and Conclusions

In this chapter, an experimental method was presented which allowed the observation of spherical ice particle impacts onto thin liquid water films in a subfreezing environment. The main advantage of this method was the relatively easy generation of a controlled film thickness, stable over time, by using a mass flow controller and a hydrophilic steel sphere with a clearance hole. Potential freezing of the film could be prevented and the evaporation of the water film could be neglected due to the continuous renewal of the film. Typical *sticking*, *bouncing*, and *fragmentation* impacts were observed. 237 no fragmentation and fragmentation impacts were analysed and it was found that for relatively thin dimensionless water films ($0.05 \leq \frac{H}{D_0} \leq 0.25$) the maximum no fragmentation velocity was approx. twice as high as in

the case of a dry wall. It was also observed that for a certain α the probability of fragmentation decreased with increasing $\frac{H}{D_0}$.

The conditions for bouncing should be investigated further. Since the ice particle does not contribute to ice accretion in the case of bouncing, this is the most favourable impact outcome to prevent ice crystal icing. As a potential result, it might be known how the particle size, impact velocity, or film thickness have to be modified to have a high probability for bouncing. For example, if a very low film thickness is required, suction holes in the relevant walls could reduce film thickness.

Significantly deformed capillary bridges were observed for relatively fast flowing water films ($H \gtrsim 350\,\mu m$). These deformations might have a significant influence on sticking and bouncing and should be analysed in the future. For example, in the extreme case, liquid bridge deformation might be followed by capillary bridge breakup, which is equivalent to bouncing. For this reason, a measure to prevent ice accretion might be to make the water film flow at relatively high speeds to increase the probability of liquid bridge breakup. For example, this could be achieved by a strong shear airflow close to the water's free surface which not only accelerates the water film but could also directly destroy (blow away) liquid bridges. Experimentally, a faster water film could be achieved with a larger steel sphere, for example. Furthermore, microstructured surfaces could enhance the probability of significant particle rotation upon impact, which may result in a higher probability of capillary bridge rupture.

Moreover, further tests could focus on the investigation of sticking and bouncing of fragments in the case of fragmentation and how the probability of bouncing of these fragments could be increased. To allow the investigation of bouncing and sticking in the case of relatively thick water films where an (almost) symmetrical liquid bridge should build up, the test apparatus should be modified. For example, the impact location could be shifted closer to the north pole so that the water film's flow velocity is lower. This would require adaptions of the front part of the spring mechanism to hold back the ice particle till acceleration. For relatively small ice particles, a smaller steel sphere (resulting in a smaller vertical distance between the north pole and equator) could be used to reduce the flow velocity of the (thick) water film at the equator. Higher impact velocities could be achieved by adapting the spring.

Finally, it would also be interesting to investigate the impacts of non-spherical ice particles, similar to the ones found in glaciated icing conditions, on thin water films to more accurately predict ice accretions in jet engines and to find adequate countermeasures.

7 Summary and Conclusions

Ice crystal icing has been indicated as the cause of a number of in-flight events and has therefore attracted the attention of the global aircraft icing community. A more precise and accurate prediction of ice crystal icing in aircraft engines and probes would contribute to enhancing aircraft safety in glaciated icing conditions. To achieve reliable prediction capabilities, research in various fields is required: in the case of engine core icing, ice particles may fragment upon impact with frontal engine surfaces (→ *ice particle impact onto a dry, cold surface*). In the engine core, these fragments may (partially) melt in warm airflow conditions (→ *ice particle melting in forced convection*) and may stick to warm surfaces of the engine's compressor, partially covered with a water film (→ *impact of ice particles onto a thin water film*). These surfaces may be cooled down by further incoming ice particles and ice accretion may occur (→ *ice accretion on a warm surface*).

This work contributed theoretically and experimentally to the expansion of the knowledge in the highlighted areas.

The initial mechanisms of ice accretion on a warm surface were investigated experimentally on a microscale level. The observed initial mechanisms are as follows: initially, tiny ice particles (~10 µm), or tiny fragments of ice particles which form upon impact, come to rest on the warm surface and melt, generating droplets or even extended films of meltwater. The meltwater allows larger ice particles to adhere to the warm surface due to capillary forces acting between the surface, water, and ice particle. Depending on the icing conditions (e.g. IWC and ice particle temperature) a slushy layer consisting of meltwater and ice particles may form. The surface may be cooled down to freezing and ice accretion may occur. In the case of mixed-phase icing conditions, the meltwater of partially melted ice particles also represents a source of water which may deposit on the surface upon impact and may accelerate the ice accretion process.

Ice particle impact onto a dry, cold surface was theoretically and experimentally investigated. Spherical and non-spherical ice particles with diameters between ~0.03 and 3.5 mm were accelerated to velocities between 1 and 74 m/s and impacted onto an aluminium target. Four different fragmentation modes were defined based on high-speed video images: no, minor, major, and catastrophic fragmentation. Based on models for the impact of semi-brittle, spherical impactors onto a flat, rigid surface, semi-empirical velocity scales were defined for the upper bounds of no and minor fragmentation. Probability distributions for minor and major/catastrophic fragmentation were presented. Three scaling relations for different

fragmentation mechanisms were derived: particle attrition and splitting, based on lateral cracks, and particle breakup, based on radial cracks. Focusing on the collected experimental data, it seems that both particle attrition and splitting are the main mechanisms of minor fragmentation and that particle splitting probably leads to major and catastrophic fragmentation. Particle breakup seems to not play a role for ice particle impacts onto flat, rigid surfaces. The post-impact behaviour, i.e. the restitution coefficient and the post-impact angle, of the fragments (or the original particle in the case of no fragmentation) were analysed. It was observed that for increasing ξ ($\xi \sim U_0 D_0^{2/3}$), the restitution coefficients and post-impact angles decreased.

Theoretical and experimental investigations of melting spherical and non-spherical ice particles in forced convection were conducted. Individual ice particles were suspended in the acoustic field of an acoustic levitator, placed in a chest freezer. An airflow, whose velocity, temperature, and RH were controlled, was used to melt the ice particles. The maximum airflow velocity and temperature were 1.75 m/s and 30 °C. The RH was varied from ~4 % to ~74 %. The experimental melting times were derived from high-speed video images. A theoretical model for the melting of ice particles was introduced and validated for melting spherical ice particles. Two different approaches were used to approximate the particle surface area (i.e. the sphericity) of non-spherical ice particles: 1) approximation of the sphericity with the crosswise sphericity; 2) approximation of the sphericity with a combination of the ISO circularity and area ratio, including two adjustable parameters determined from the best fit to the data. 157 non-spherical melting processes were analysed: the 1st approach led to an improvement (decrease) of the mean value of the relative differences of the theoretical and experimental melting times by 51 % compared to the common assumption of melting spherical ice particles with equivalent mass; the 2nd approach led to an improvement (decrease) of such mean value by 65.8 %.

A test apparatus was designed and built which allows the investigation of ice particle impacts onto thin liquid water films in a subfreezing environment. 237 impacts of spherical ice particles were analysed. The diameter of the spherical ice particles was in the range from 1.18 to 3.52 mm. Impact velocity and film thickness were varied from 1.2 to 5.8 m/s and from approx. 130 to 600 µm. Typical sticking, bouncing, and fragmentation impacts were described. Significantly deformed liquid bridges were observed for a film thickness $\gtrsim$ 350 µm. Their occurrence was traced back to the relatively large thickness of the water film and the large velocity gradient within the laminar boundary layer of the film. It was observed that for

relatively thin dimensionless water films ($0.05 \leq \frac{H}{D_0} \leq 0.25$) the maximum no fragmentation velocity was approx. two times higher than compared to the dry target case. For a certain α ($\alpha = U_0 D_0^{2/3}$), the probability of fragmentation decreased with increasing dimensionless film thickness.

In conclusion, the findings gained in this work represent an important step forward in the understanding and prediction of ice crystal icing.

The analysis of the initial mechanisms of ice crystal icing on a microscale level showed that to delay/reduce ice accretion in glaciated icing conditions, the generation of tiny fragments and their probability of coming to rest on warm surfaces should be decreased. As hypothesised in section 3.4, a superhydrophobic, inclined, and smooth surface could lead to less meltwater droplets being generated and resting on a warm surface; in this way lowering the probability of ice accretion. Moreover, if such a surface was heated, ice shedding could be promoted by the generation of a liquid layer between the accreted ice and surface.

Under the assumption that the relations derived from the experimental impact data in chapters 4.4 and 4.5 are also valid for smaller natural ice particles and higher impact velocities than investigated, the following can be concluded: 1) ice particles with diameters $\gtrsim 3$ µm, which impact in cruise flight $\left(U_0 \approx 230\ \mathrm{m/s}\right)$ onto dry, cold aircraft structures at a right angle, experience any kind of fragmentation; 2) ice particles with diameters $\gtrsim 18$ µm, which impact under the same conditions, experience major or catastrophic fragmentation; 3) taking into account impact studies of spherical ice particles from literature (chapter 4.6), ice particles with diameters $\gtrsim 1.3$ mm may experience perfectly catastrophic fragmentation, which is defined by the generation of hundreds of fragments and a hardly identifiable biggest fragment which has less than 1 % of the initial volume of the ice particle. In conclusion, the fragmentation modes of small ice particles can be predicted more accurately. Considering the relations for the post-impact angles and velocities developed in this thesis, it is possible to establish the initial conditions of post-impact trajectories of the (biggest) fragments. Moreover, the experimental impact data collected in this work contributed to the refinement of an ice particle impact model based on the approach from Vidaurre & Hallett[31] by Villedieu et al.[87] and Iuliano[118].

The experimental and theoretical investigation of ice particle melting in forced convection led to a more accurate melting model for ice particles. The melting model considers a Nusselt correlation which uses ice particle quantities for the approximation of the sphericity that can be easily derived from measurements done with common optical aircraft probes used in flight

test campaigns. With this melting model, it is possible to more accurately (compared to the common assumption of melting spherical ice particles with equivalent mass) calculate the LWC to TWC ratio and the mass of the ice particle upon impact onto engine structures. Hence, icing severity can be predicted better. Moreover, the database of very detailed high-speed videos of more than 200 melting processes contributed to the development of a new model describing the shape change of a non-spherical ice particle during melting by Kintea et al.[56].

The feasibility of tests where fully frozen ice particles impact onto a thin liquid film was demonstrated. The advantages of the presented method are: 1) using a mass flow controller and a hydrophilic steel sphere with a clearance hole, a thin liquid film with easily controllable thickness was generated; 2) potential freezing of the film in a subfreezing environment was prevented, and 3) the evaporation of the water film could be neglected due to the continuous renewal of the film. However, for film thicknesses $\gtrsim 350$ µm deformed liquid bridges occurred whose influence on the impact outcome is not yet known. The developed test method demonstrates an efficient option to expand the knowledge of bouncing, sticking, and fragmentation needed to improve the understanding of ice accretion on aircraft structures.

7.1 Outlook

The presented work contributed to the better understanding of fundamental processes relevant for ice crystal icing. However, further research still needs to be done to be able to satisfactorily cope with this form of icing. In the future, investigations should be conducted to more accurately predict and to allow the reduction (or even prevention) of ice crystal icing events in glaciated icing conditions:

- Tiny fragments coming to rest on warm surfaces, or meltwater stemming from the impact of partially melted ice particles, allow the ice accretion process to start. For this reason, it will be necessary to investigate the effect of anti-icing coatings (e.g. with superhydrophobic or icephobic properties) on the initiation of ice accretion to find possible answers to the question: How to delay, reduce, or even prevent ice accretion?
- The presented impact and melting tests have been conducted with non-spherical ice particles naturally grown at a chest freezer's wall or spherical ice particles generated on a superhydrophobic surface. It is not known if the non-spherical ice particles' properties (e.g. the inner structure or surface roughness) are representative for natural ice particles encountered in glaciated icing conditions. To gain impact and

melting data of those natural ice particles, laboratory tests could be conducted with ice particles generated in a cloud chamber. Moreover, impacts of ice particles in relevant clouds could be observed using a similar test apparatus on a test aircraft. Potentially, the best way and the biggest challenge would be to find a possibility to unbrokenly collect natural ice particles at high altitudes and to conduct impact and melting lab tests with those particles. The technique for spherical ice particle generation may have a significant influence on the inner structure and the impact process. Further research should focus on the following questions: How do the different generation techniques influence the internal structure and mechanical properties of spherical ice particles, eventually leading to different impact outcomes under similar conditions? Which generation technique should be used to create spherical ice particles whose impact process represents impact processes of natural ice particles best? In this context, the definition of a standard for the generation of spherical ice particles should be considered.

- Ice particle impact onto a thin water film should be further investigated. Since bouncing is the most favourable impact outcome which, solely, does not lead to ice accretion, the requirements for a high probability of this mode should be investigated in detail. Moreover, it should be investigated how the probability of fragment bouncing in the case of fragmentation may be increased. Adequate models should be developed to allow the simulation of these complex processes.

Acknowledgements

I am very grateful to have met so many people who have supported me during this successful journey.

Thank you Elmar Bonaccurso for your excellent supervision and your well appreciated feedback. I am very happy that you joined our team and taught me a lot!

Thank you Dominik Raps, Jürgen Wehr, and Claudio Dalle Donne for giving me the opportunity to write this thesis at Airbus Group Innovations. Dominik, I really appreciated your supervision and the fun we had. Jürgen, thank you for your excellent mentoring and your continuous support.

I would like to thank Prof. Cameron Tropea and Ilia V. Roisman from the Institute of Fluid Mechanics and Aerodynamics (SLA) at TU Darmstadt. Thank you very much for your supervision, collaboration, and the fruitful discussions. Moreover, thank you very much for the provision of a high-speed video camera and the acoustic levitator! I also want to thank Daniel Kintea and Lars Opfer from TU Darmstadt for the great collaboration. Daniel, besides our great common achievements, I will definitely miss the fun we had on our business trips!

I appreciated a lot the great collaboration with Prof. Philippe Villedieu and Pierre Trontin from ONERA Toulouse. Thank you very much for your suggestions and the fruitful discussions. It was great to meet and work with you! Merci beaucoup!

For the fantastic daily collaborative work, I want to thank Tobias Strobl, Ondrej Lajza, and Pavel Zikmund. It was great to create the Icing and Contamination Research Facility (iCORE) together with you and find solutions together. Moreover, thank you Tobias for the smooth collaboration when Dominik left our team and we were in charge of keeping up all the icing activities in our department.

The test apparatuses presented in this thesis were designed and built with the help of the well appreciated colleagues from the workshop. Thank you Xaver Hallweger, Josef Willert, and Bodo Haffner for your comments, suggestions, and excellent work.

I also want to thank Winfried Kupke for the provision of a high-speed video camera and for his advice.

I enjoyed the time a lot at Airbus Group Innovations! And that is why I want to sincerely thank all my colleagues, especially from the Metallic Technologies & Surface Engineering

Department, for the professionalism, your support, and all the nice non-work related experiences.

It was a great honor for me to be part of the HAIC project during my thesis and to get to know so many dedicated and proactive people. It was great to meet you regularly in our project meetings! Thanks to all of you for the great collaboration!

Moreover, it was great to meet many people from the global aircraft icing community at various conferences and meetings. Thank you for the fruitful discussions and your suggestions! It was great to be part of such a dedicated and motivated group which showed so much passion to predict ice crystal icing better.

Thanks a lot to the students which supported me during their internships: Thank you Robert Adam, Oliver Ulke, Jan-Pascal Roth, Max von der Grün, and Jens Loewe.

Many thanks to Daniela Niedermeier, Sonja Deuter, and Werner Lang for supporting me in administrative and project-related financial matters.

Special thanks go to my family and friends who continuously supported me during my whole education. Special thanks also go to my girlfriend Jana who continuously supported and motivated me whenever needed and showed lots of patience.

Thanks to all of you!

Bibliography

1 Lankford, T. T., *Aircraft Icing: A Pilot's Guide*, 1st edition, McGraw-Hill Professional, New York, USA, 1999.

2 *Aircraft Icing Handbook*, Civil Aviation Authority of New Zealand, Lower Hutt, New Zealand, 2000.

3 Heinrich, A., Ross, R., Zumwalt, G., Provorse, J., Padmanabhan, V., Thompson, J., and Riley, J., *Aircraft Icing Handbook Volume 1 of 3*, Gates Learjet Corporation, Wichita, USA, 1991.

4 Heinrich, A., Ross, R., Zumwalt, G., Provorse, J., Padmanabhan, V., Thompson, J., and Riley, J., *Aircraft Icing Handbook Volume 3 of 3*, Gates Learjet Corporation, Wichita, USA, 1991.

5 Jeck, R. K., *Icing Design Envelopes (14 CFR Parts 25 and 29, Appendix C) Converted to a Distance-Based Format*, Federal Aviation Administration, Atlantic City, USA, 2002.

6 Minigone, G., and Barocco, M., *Flight in Icing Conditions*, Direction générale de l'aviation civile, Paris, France, 1997, available: http://www.developpement-durable.gouv.fr/IMG/pdf/DGAC_Icing_flight_manual.pdf (accessed 20th July 2015).

7 Heinrich, A., Ross, R., Zumwalt, G., Provorse, J., Padmanabhan, V., Thompson, J., and Riley, J., *Aircraft Icing Handbook Volume 2 of 3*, Gates Learjet Corporation, Wichita, USA, 1991.

8 Bravin, M., Strapp, J. W., and Mason, J., "An Investigation into Location and Convective Lifecycle Trends in an Ice Crystal Icing Engine Event Database," *SAE 2015 International Conference on Icing of Aircraft, Engines, and Structures*, SAE International, Warrendale, USA, 2015.

9 Mason, J., Strapp, W., and Chow, P., "The Ice Particle Threat to Engines in Flight," *44th AIAA Aerospace Sciences Meeting and Exhibit*, American Institute of Aeronautics and Astronautics, Reston, USA, 2006.

10 Mazzawy, R. S., and Strapp, J. W., "Appendix D - An Interim Icing Envelope," *SAE Aircraft and Engine Icing International Conference*, SAE International, Warrendale, USA, 2007, pp. 634–642.

11 Strapp, J. W., Schwarzenboeck, A., Delanoe, J., Dezitter, F., Dumont, C., Grandin, A., Korolev, A., Lilie, L., Potts, R., Protat, A., Ratvasky, T., and Riley, J., "Preliminary Assessment of Appendix D/P Total Water Content from In-Situ Measurements of Deep Convective Clouds in the HAIC-HIWC Darwin-2014 Flight Campaign," *SAE 2015 International Conference on Icing of Aircraft, Engines, and Structures*, SAE International, Warrendale, USA, 2015.

12 Grandin, A., Ratvasky, T., Schwarzenboeck, A., Strapp, J. W., Dezitter, F., Duchanoy, D., Bourdinot, J.-F., Delanoe, J., Potts, R., Protat, A., Lilie, L., Korolev, A., and Turner, S., "HAIC/HIWC International Field Campaign Overview & Preliminary Outcomes," *SAE 2015 International Conference on Icing of Aircraft, Engines, and Structures*, SAE International, Warrendale, USA, 2015.

13 Corti, T., Luo, B. P., de Reus, M., Brunner, D., Cairo, F., Mahoney, M. J., Martucci, G., Matthey, R., Mitev, V., dos Santos, F. H., Schiller, C., Shur, G., Sitnikov, N. M., Spelten, N., Vössing, H. J., Borrmann, S., and Peter, T., "Unprecedented evidence for deep convection hydrating the tropical stratosphere," *Geophysical Research Letters*, vol. 35, 2008.

14 Furukawa, Y., and Wettlaufer, J. S., "Snow and ice crystals," *Physics Today*, vol. 60, Dec. 2007, pp. 70–71.

15 Libbrecht, K. G., "The formation of snow crystals," *American Scientist*, vol. 95, 2007, pp. 52–59.

16 Bailey, M., and Hallett, J., "Growth Rates and Habits of Ice Crystals between -20 °C and -70 °C," *Journal of the Atmospheric Sciences*, vol. 61, 2004, pp. 514–544.

17 Avissar, R., "The Large-Scale Biosphere-Atmosphere Experiment in Amazonia (LBA): Insights and future research needs," *Journal of Geophysical Research*, vol. 107, 2002, pp. 54-1 – 54-6.

18 Delnore, V. E., Cox, S. K., and Curran, R. J., "CRYSTAL - The Cirrus Regional Study of Tropical Anvils and Layers," *IRS 2000: Current Problems in Atmospheric Radiation*, A. Deepak Publishing, Hampton, USA, 2001, pp. 1069–1072.

19 Yuter, S. E., Houze, R. A., Smith, E. A., Wilheit, T. T., and Zipser, E., "Physical Characterization of Tropical Oceanic Convection Observed in KWAJEX," *Journal of Applied Meteorology*, vol. 44, 2005, pp. 385–415.

20 Schwarzenboeck, A., Dezitter, F., Grandin, A., and Protat, A., *HighIWC - Ice Water Content of clouds at high altitude*, European Aviation Safety Agency, Cologne, 2012.

21 Heymsfield, A. J., Bansemer, A., Field, P. R., Durden, S. L., Stith, J. L., Dye, J. E., Hall, W., and Grainger, C. A., "Observations and Parameterizations of Particle Size Distributions in Deep Tropical Cirrus and Stratiform Precipitating Clouds: Results from In Situ Observations in TRMM Field Campaigns," *Journal of the Atmospheric Sciences*, vol. 59, Dec. 2002, pp. 3457–3491.

22 Mason, J. G., Chow, P., and Fuleki, D. M., "Understanding Ice Crystal Accretion and Shedding Phenomenon in Jet Engines Using a Rig Test," *Journal of Engineering for Gas Turbines and Power*, vol. 133, 2011, p. 041201.

23 Addy, H. E., and Veres, J. P., "An Overview of NASA Engine Ice-Crystal Icing Research," *International Conference on Aircraft and Engine Icing and Ground Deicing*, SAE International, Warrendale, USA, 2011.

24 English, W., *Factual Report - NTSB ID: DCA06IA007*, NTSB, Washington, D.C., 2008.

25 *Final Report (AF 447)*, Bureau d'Enquêtes et d'Analyses, Le Bourget, France, Jul. 2012, available: http://www.bea.aero/en/enquetes/flight.af.447/reports.php (accessed: 21st July 2015).

26 *AAIB Bulletin: 6/2011*, Air Accidents Investigation Branch, Farnborough, UK, Jun. 2011, available:

https://www.gov.uk/government/uploads/system/uploads/attachment_data/file/384823/AAIB_Bulletin_6-2011.pdf (accessed: 21st July 2015).

27 *NPA 2011-03 - Large Aeroplane Certification Specifications in Supercooled Large Drop, Mixed phase, and Ice Crystal Icing Conditions*, European Aviation Safety Agency, Cologne, Mar. 2011.

28 *NPA 2011-04 - Turbine Engine Certification Specifications in Icing Conditions*, European Aviation Safety Agency, Cologne, Apr. 2011.

29 Higa, M., Arakawa, M., and Maeno, N., "Measurements of restitution coefficients of ice at low temperatures," *Planetary and Space Science*, vol. 44, Sep. 1996, pp. 917–925.

30 Higa, M., Arakawa, M., and Maeno, N., "Size Dependence of Restitution Coefficients of Ice in Relation to Collision Strength," *ICARUS*, vol. 133, 1998, pp. 310–320.

31 Vidaurre, G., and Hallett, J., "Particle Impact and Breakup in Aircraft Measurement," *Journal of Atmospheric and Oceanic Technology*, vol. 26, May 2009, pp. 972–983.

32 Emery, E., Miller, D., Plaskon, S., Strapp, W., and Lillie, L., "Ice Particle Impact on Cloud Water Content Instrumentation," *42nd AIAA Aerospace Sciences Meeting and Exhibit*, American Institute of Aeronautics and Astronautics, Reston, USA, 2004.

33 Isaac, G., Korolev, A., Srapp, J. W., Cober, S., Boudala, F., Marcotte, D., and Reich, V., "Assessing the Collection Efficiency of Natural Cloud Particles Impacting the Nevzorov Total Water Content Probe," *44th AIAA Aerospace Sciences Meeting and Exhibit*, American Institute of Aeronautics and Astronautics, Reston, USA, 2006.

34 Guégan, P., Othman, R., Lebreton, D., Pasco, F., Villedieu, P., Meyssonnier, J., and Wintenberger, S., "Critical impact velocity for ice fragmentation," *Proceedings of the Institution of Mechanical Engineers, Part C: Journal of Mechanical Engineering Science*, vol. 226, Nov. 2011, pp. 1677–1682.

35 Garwood, K. R., *AGARD-AR-332 - Recommended practices for the assessment of the effects of atmospheric water ingestion on the performance and operability of gas turbine engines*, AGARD, Neuilly-sur-Seine, France, Sep. 1995.

36 Pan, H., and Render, P. M., "Impact characteristics of hailstones simulating ingestion by turbofan aeroengines," *Journal of Propulsion and Power*, vol. 12, May 1996, pp. 457–462.

37 Guégan, P., Othman, R., Lebreton, D., Pasco, F., Villedieu, P., Meyssonnier, J., and Wintenberger, S., "Experimental investigation of the kinematics of post-impact ice fragments," *International Journal of Impact Engineering*, vol. 38, Oct. 2011, pp. 786–795.

38 Pan, H., and Render, P. M., "Studies into hail ingestion of turbofan engines using a rotating fan and spinner assembly," *The Aeronautical Journal*, vol. 102, 1998, pp. 45–51.

39 Render, P. M., and Pan, H., "Experimental Studies into Hail Impact Characteristics," *Journal of Propulsion and Power*, vol. 11, 1995, pp. 1224–1230.

40 Tippmann, J. D., Kim, H., and Rhymer, J. D., "Experimentally validated strain rate dependent material model for spherical ice impact simulation," *International Journal of Impact Engineering*, vol. 57, Jul. 2013, pp. 43–54.

41 Vargas, M. M., Struk, P. M., Kreeger, R. E., Palacios, J., Iyer, K., and Gold, R. E., "Ice Particle Impacts on a Moving Wedge," *6th AIAA Atmospheric and Space Environments Conference*, American Institute of Aeronautics and Astronautics, Reston, USA, 2014.

42 Vargas, M., Ruggeri, C., Struk, P., Pereira, M., Revilock, D., and Kreeger, R., "Ice Particle Impacts on a Flat Plate," *SAE 2015 International Conference on Icing of Aircraft, Engines, and Structures*, SAE International, Warrendale, USA, 2015.

43 Roisman, I. V, and Tropea, C., "Impact of a crushing ice particle onto a dry solid wall," *Proceedings of the Royal Society A: Mathematical, Physical and Engineering Science*, vol. 471, Nov. 2015, p. 20150525.

44 Palacios, J., Yan, S., Tan, C., and Kreeger, R. E., "Experimental Measurement of Frozen and Partially Melted Water Droplet Impact Dynamics," *6th AIAA Atmospheric and Space Environments Conference*, American Institute of Aeronautics and Astronautics, Reston, USA, 2014.

45 Rasmussen, R. M., and Pruppacher, H. R., "A Wind Tunnel and Theoretical Study of the Melting Behavior of Atmospheric Ice Particles. I: A Wind Tunnel Study of Frozen Drops of Radius < 500 μm," *Journal of the Atmospheric Sciences*, vol. 39, Jan., 1982, pp. 152–158.

46 Rasmussen, R. M., Levizzani, V., and Pruppacher, H. R., "A Wind Tunnel and Theoretical Study of the Melting Behavior of Atmospheric Ice Particles. II: A Theoretical Study for Frozen Drops of Radius < 500 μm," *Journal of the Atmospheric Sciences*, vol. 41, no. 3, 1984, pp. 374–380.

47 Rasmussen, R. M., Levizzani, V., and Pruppacher, H. R., "A Wind Tunnel and Theoretical Study on the Melting Behavior of Atmospheric Ice Particles. III: Experiment and Theoryfor Spherical Ice Particles of Radius > 500 μm," *Journal of the Atmospheric Sciences*, vol. 41, no. 3, 1984, pp. 381–388.

48 Comer, J. K., and Kleinstreuer, C., "Computational analysis of convection heat transfer to non-spherical particles," *International Journal of Heat and Mass Transfer*, vol. 38, Nov. 1995, pp. 3171–3180.

49 Sparrow, E. M., Abraham, J. P., and Tong, J. C. K., "Archival correlations for average heat transfer coefficients for non-circular and circular cylinders and for spheres in cross-flow," *International Journal of Heat and Mass Transfer*, vol. 47, Nov. 2004, pp. 5285–5296.

50 Richter, A., and Nikrityuk, P. A., "Drag forces and heat transfer coefficients for spherical, cuboidal and ellipsoidal particles in cross flow at sub-critical Reynolds numbers," *International Journal of Heat and Mass Transfer*, vol. 55, Jan. 2012, pp. 1343–1354.

51 Buck, A. L., "New Equations for Computing Vapor Pressure and Enhancement Factor," *Journal of Applied Meteorology*, vol. 20, 1981, pp. 1527–1532.

52 Mason, B. J., “On the melting of hailstones,” *Quarterly Journal of the Royal Meteorological Society*, vol. 82, 1956, pp. 209–216.

53 Wright, W. B., Jorgenson, P. C. E., and Veres, J. P., “Mixed Phase Modeling in GlennICE With Application to Engine Icing,” NASA-TM-2011-216978, 2011.

54 Currie, T., Fuleki, D., and Davison, C., “Simulation of Ice Particle Melting in the NRC RATFac Mixed-Phase Icing Tunnel,” *SAE 2015 International Conference on Icing of Aircraft, Engines, and Structures*, SAE International, Warrendale, USA, 2015.

55 Hauk, T., Roisman, I. V., and Tropea, C., “Investigation of the Melting Behaviour of Ice Particles in an Acoustic Levitator,” *11th AIAA/ASME Joint Thermophysics and Heat Transfer Conference*, American Institute of Aeronautics and Astronautics, Reston, USA, 2014.

56 Kintea, D. M., Hauk, T., Roisman, I. V., and Tropea, C., “Shape evolution of a melting nonspherical particle,” *Physical review E, statistical, nonlinear, and soft matter physics*, vol. 92, Sep. 2015, p. 033012.

57 Matsuo, T., and Sasyo, Y., “Empirical Formula for the Melting Rate of Snowflakes,” *Journal of the Meteorological Society of Japan*, vol. 59, no. 1, 1981, pp. 1–8.

58 Matsuo, T., and Sasyo, Y., “Melting of Snowflakes below Freezing Level in the Atmosphere,” *Journal of the Meteorological Society of Japan*, vol. 59, no. 1, 1981, pp. 10–25.

59 Fukuta, N., Savage, R. C., Donovan, G. J., and Liu, C. M., “The microphysics of snow crystal and snow flake melting,” AFGL-TR-83-0066, University of Utah, Salt Lake City, USA, 1982.

60 Mitra, S. K., Vohl, O., Ahr, M., and Pruppacher, H. R., “A Wind Tunnel and Theoretical Study of the Melting Behavior of Atmospheric Ice Particles. IV: Experiment and Theory for Snow Flakes,” *Journal of the Atmospheric Sciences*, vol. 47, no. 5, 1990, pp. 584–591.

61 Zhao, M.-H., Chen, X.-P., and Wang, Q., “Wetting failure of hydrophilic surfaces promoted by surface roughness,” *Scientific reports*, vol. 4, Jan. 2014, p. 5376.

62 Antonyuk, S., Heinrich, S., Deen, N., and Kuipers, H., “Influence of liquid layers on energy absorption during particle impact,” *Particuology*, vol. 7, 2009, pp. 245–259.

63 Antonyuk, S., Heinrich, S., and Palzer, S., “Impact Behaviour of Particles with Liquid Films: Energy Dissipation and Sticking Criteria,” *The 13th International Conference on Fluidization - New Paradigm in Fluidization Engineering*, Engineering Conferences International, New York, USA, 2010.

64 Gollwitzer, F., Rehberg, I., Kruelle, C. a., and Huang, K., “Coefficient of restitution for wet particles,” *Physical review E, statistical, nonlinear, and soft matter physics*, vol. 86, Jul. 2012, p. 011303.

65 Kantak, A., Galvin, J. E., Wildemuth, D. J., and Davis, R. H., “Low-velocity collisions of particles with a dry or wet wall,” *Microgravity - Science and Technology*, vol. 17, Mar. 2005, pp. 18–25.

66 Davis, R. H., Rager, D. A., and Good, B. T., “Elastohydrodynamic rebound of spheres from coated surfaces,” *Journal of Fluid Mechanics*, vol. 468, Oct. 2002, pp. 107–119.

67 Kantak, A., and Davis, R. H., “Oblique collisions and rebound of spheres from a wetted surface,” *Journal of Fluid Mechanics*, vol. 509, Jun. 2004, pp. 63–81.

68 Hauk, T., Grün, M. Von Der, Roisman, I. V, and Tropea, C., “Investigation of the coefficient of restitution of spheres impacting on a water film,” *ILASS-Europe, 26th European Conference on Liquid Atomization and Spray Systems*, ILASS-Europe, Naples, Italy, 2014.

69 Worthington, A. M., “On Impact with a Liquid Surface,” *Proceedings of the Royal Society of London*, vol. 34, Jan. 1882, pp. 217–230.

70 Duez, C., Ybert, C., Clanet, C., and Bocquet, L., “Making a splash with water repellency,” *Nature Physics*, vol. 3, Feb. 2007, pp. 180–183.

71 McKown, J. M., “An Experimental Study of Worthington Jet Formation After Impact of Solid Spheres,” Master thesis, Massachusetts Institute of Technology, Massachusetts, USA, 2011.

72 Antonyuk, S., Heinrich, S., Deen, N., and Kuipers, H., “Influence of liquid layers on energy absorption during particle impact,” *Particuology*, vol. 7, Aug. 2009, pp. 245–259.

73 Al-Khalil, K., Irani, E., and Miller, D., “Mixed Phase Icing Simulation and Testing at the Cox Icing Wind Tunnel,” *41st Aerospace Sciences Meeting and Exhibit*, American Institute of Aeronautics and Astronautics, Reston, USA, 2003.

74 MacLeod, J. D., “Development of Ice Crystal Facilities for Engine Testing,” *SAE Aircraft & Engine Icing International Conference*, SAE International, Warrendale, USA, 2007.

75 Currie, T. C., Fuleki, D., and Mahallati, A., “Experimental Studies of Mixed-Phase Sticking Efficiency for Ice Crystal Accretion in Jet Engines,” *6th AIAA Atmospheric and Space Environments Conference*, American Institute of Aeronautics and Astronautics, Reston, USA, 2014.

76 Struk, P., Currie, T., Wright, W. B., Knezevici, D., Fuleki, D., Broeren, A., Vargas, M., and Tsao, J.-C., “Fundamental Ice Crystal Accretion Physics Studies,” *SAE 2011 International Conference on Aircraft and Engine Icing and Ground Deicing*, SAE International, Warrendale, USA, 2011.

77 Currie, T., Struk, P., Tsao, J.-C., Fuleki, D., and Knezevici, D., “Fundamental Study of Mixed-Phase Icing with Application to Ice Crystal Accretion in Aircraft Jet Engines,” *4th AIAA Atmospheric and Space Environments Conference*, American Institute of Aeronautics and Astronautics, Reston, USA, 2012.

78 Knezevici, D., Fuleki, D., Currie, T., and MacLeod, J., “Particle Size Effects on Ice Crystal Accretion,” *4th AIAA Atmospheric and Space Environments Conference*, American Institute of Aeronautics and Astronautics, Reston, USA, 2012.

79 Knezevici, D., Fuleki, D., Currie, T. C., Galeote, B., Chalmers, J., and MaCleod, J. D., “Particle Size Effects on Ice Crystal Accretion - Part II,” *5th AIAA Atmospheric and Space*

Environments Conference, American Institute of Aeronautics and Astronautics, Reston, USA, 2013.

80 Currie, T. C., Fuleki, D., Knezevici, D., and MacCleod, J. D., "Altitude Scaling of Ice Crystal Accretion," *5th AIAA Atmospheric and Space Environments Conference*, American Institute of Aeronautics and Astronautics, Reston, USA, 2013.

81 Struk, P., Bartkus, T., Tsao, J.-C., Currie, T., and Fuleki, D., "Ice Accretion Measurements on an Airfoil and Wedge in Mixed-Phase Conditions," *SAE 2015 International Conference on Icing of Aircraft, Engines, and Structures*, SAE International, Warrendale, USA, 2015.

82 Habashi, W., and Nilamdeen, S., "Multiphase Approach Toward Simulating Ice Crystal Ingestion in Jet Engines," *Journal of Propulsion and Power*, vol. 27, Sep. 2011, pp. 959–969.

83 Habashi, W. G., Veillard, X., and Baruzzi, G. S., "Icing Simulation in Multistage Jet Engines," *Journal of Propulsion and Power*, vol. 27, Nov. 2011, pp. 1231–1237.

84 Nilamdeen, S., Habashi, W., Aubé, M., and Baruzzi, G., "FENSAP-ICE: Modeling of Water Droplets and Ice Crystals," *1st AIAA Atmospheric and Space Environments Conference*, American Institute of Aeronautics and Astronautics, Reston, USA, 2009.

85 Veres, J. P., Jorgenson, P. C., and Coennen, R. J., "Modeling of Commercial Turbofan Engine with Ice Crystal Ingestion; Follow-On," *6th AIAA Atmospheric and Space Environments Conference*, American Institute of Aeronautics and Astronautics, Reston, USA, 2014.

86 Tsao, J., Struk, P. M., and Oliver, M. J., "Possible Mechanisms for Turbofan Engine Ice Crystal Icing at High Altitude," *6th AIAA Atmospheric and Space Environments Conference*, American Institute of Aeronautics and Astronautics, Reston, USA, 2014.

87 Villedieu, P., Trontin, P., and Chauvin, R., "Glaciated and mixed phase ice accretion modeling using ONERA 2D icing suite," *6th AIAA Atmospheric and Space Environments Conference*, American Institute of Aeronautics and Astronautics, Reston, USA, 2014.

88 Kintea, D. M., Roisman, I. V, and Tropea, C., "Numerical investigation of ice particle accretion on heated surfaces with application to aircraft engines," *11th AIAA/ASME Joint Thermophysics and Heat Transfer Conference*, American Institute of Aeronautics and Astronautics, Reston, USA, 2014.

89 Messinger, B. L., "Equilibrium Temperature of an Unheated Icing Surface as a Function of Air Speed," *Journal of the Aeronautical Sciences*, vol. 20, Jan. 1953, pp. 29–42.

90 Feulner, M., Liao, S., Rose, B., and Liu, X., "Ice Crystal Ingestion in a Turbofan Engine," *SAE 2015 International Conference on Icing of Aircraft, Engines, and Structures*, SAE International, Warrendale, USA, 2015.

91 Andrews, J. P., "LVI. Theory of collision of spheres of soft metals," *The London, Edinburgh, and Dublin Philosophical Magazine and Journal of Science*, vol. 9, Apr. 1930, pp. 593–610.

92 Taylor, G., “The Use of Flat-Ended Projectiles for Determining Dynamic Yield Stress. I. Theoretical Considerations,” *Proceedings of the Royal Society A: Mathematical, Physical and Engineering Sciences*, vol. 194, Sep. 1948, pp. 289–299.

93 Birkhoff, G., MacDougall, D. P., Pugh, E. M., and Taylor, G., “Explosives with lined cavities,” *Journal of Applied Physics*, vol. 19, 1948, pp. 563–582.

94 Hauk, T., Strobl, T., and Raps, D., “Implementation and Calibration of the Icing and Contamination Research Facility (iCORE),” *ILASS-Europe, 25th European Conference on Liquid Atomization and Spray Systems*, ILASS-Europe, Naples, Italy, 2013.

95 Evans, A. G., and Wilshaw, T. R., “Quasi-Static Solid Particle Damage in Brittle Solids-I. Observations, Analysis and Implications,” *Acta Metallurgica*, vol. 24, 1976, pp. 939–956.

96 Ghadiri, M., and Zhang, Z., “Impact attrition of particulate solids. Part 1: A theoretical model of chipping,” *Chemical Engineering Science*, vol. 57, Sep. 2002, pp. 3659–3669.

97 Combescure, a., Chuzel-Marmot, Y., and Fabis, J., “Experimental study of high-velocity impact and fracture of ice,” *International Journal of Solids and Structures*, vol. 48, Oct. 2011, pp. 2779–2790.

98 Kato, M., “Ice-on-Ice Impact Experiments,” *Icarus*, vol. 113, Feb. 1995, pp. 423–441.

99 Lange, M. A., and Ahrens, T. J., “Impact experiments in low-temperature ice,” *Icarus*, vol. 69, Mar. 1987, pp. 506–518.

100 Shrine, N., “Velocity Scaling of Impact Craters in Water Ice over the Range 1 to 7.3 km s−1,” *Icarus*, vol. 155, Feb. 2002, pp. 475–485.

101 Liu, H. W., and Miller, K. J., “Fracture toughness of fresh-water ice,” *Journal of Glaciology*, vol. 22, 1979, pp. 135–145.

102 Kim, H., Welch, D. a, and Kedward, K. T., “Experimental investigation of high velocity ice impacts on woven carbon/epoxy composite panels,” *Composites Part A: Applied Science and Manufacturing*, vol. 34, Jan. 2003, pp. 25–41.

103 Salman, A. D., Biggs, C. A., Fu, J., Angyal, I., Szabó, M., and Hounslow, M. J., “An experimental investigation of particle fragmentation using single particle impact studies,” *Powder Technology*, vol. 128, Dec. 2002, pp. 36–46.

104 Marshall, D. B., and Lawn, B. R., “Residual stress effects in sharp contact cracking,” *Journal of Materials Science*, vol. 14, Aug. 1979, pp. 2001–2012.

105 Lawn, B. R., Evans, A. G., and Marshall, D. B., “Elastic/Plastic Indentation Damage in Ceramics: The Median/Radial Crack System,” *Journal of the American Ceramic Society*, vol. 63, Sep. 1980, pp. 574–581.

106 Antonyuk, S., Heinrich, S., Tomas, J., Deen, N. G., Buijtenen, M. S., and Kuipers, J. A. M., “Energy absorption during compression and impact of dry elastic-plastic spherical granules,” *Granular Matter*, vol. 12, Jan. 2010, pp. 15–47.

107 Kantak, A., and Davis, R. H., “Oblique collisions and rebound of spheres from a wetted surface,” *Journal of Fluid Mechanics*, vol. 509, 2004, pp. 63–81.

108 Frössling, N., “The evaporation of falling drops,” *Gerlands Beiträge zur Geophysik*, vol. 52, 1938, pp. 170–216.

109 Hölzer, A., and Sommerfeld, M., “New simple correlation formula for the drag coefficient of non-spherical particles,” *Powder Technology*, vol. 184, Jun. 2008, pp. 361–365.

110 Schirmer, R., “Die Diffusionszahl von Wasserdampf-Luft-Gemischen und die Verdampfungsgeschwindigkeit,” *Beiheft VDI-Zeitschrift, Verfahrenstechnik*, vol. 6, 1938, pp. 170–177.

111 Höppner, J., “Verfahren zur berührungslosen Handhabung mittels leistungsstarker Schallwandler,” Dissertation, Lehrstuhl für Montagesystemtechnik und Betriebswissenschaften, Technische Universität München, 2002.

112 Godsave, G. A. E., “Studies of the combustion of drops in a fuel spray—the burning of single drops of fuel,” *Symposium (International) on Combustion*, vol. 4, Jan. 1953, pp. 818–830.

113 Spalding, D. B., “The combustion of liquid fuels,” *Symposium (International) on Combustion*, vol. 4, Jan. 1953, pp. 847–864.

114 Spalding, D. B., *Combustion and Mass Transfer*, Pergamon Press, Oxford, 1979.

115 Zaitone, B. A. Al, “Drying of Multiphase Single Droplets via Acoustic Levitation,” Dissertation, Fachbereich Maschinenbau, Technische Universität Darmstadt, 2008.

116 Seaver, M., Galloway, A., and Manuccia, T. J., “Acoustic levitation in a free-jet wind tunnel,” *Review of Scientific Instruments*, vol. 60, 1989, p. 3452.

117 Seaver, M., Galloway, A., and Manuccia, T. J., “Water Condensation onto an Evaporating Drop of 1-Butanol,” *Aerosol Science and Technology*, vol. 12, Jun. 2007, pp. 741–744.

118 Iuliano, E., “Modeling of Particle Impingement in Presence of Ice Crystals The Eulerian Model for Particle Flow Solution Eulerian Modeling of Particle Impingement,” *SAE 2015 International Conference on Icing of Aircraft, Engines, and Structures*, SAE International, Warrendale, USA, 2015.

Appendix

Overall and close-up views of the test apparatus

In the following, different views of all test apparatus designed and used in this thesis are shown.

Exploratory ice accretion experiments on a warm surface

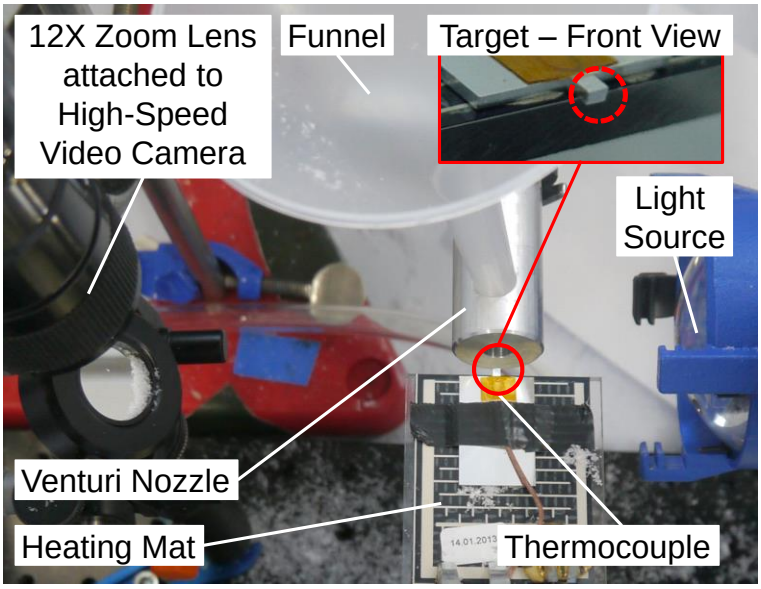

Figure 1. Close-up view of test apparatus for exploratory ice accretion experiments on a warm surface.

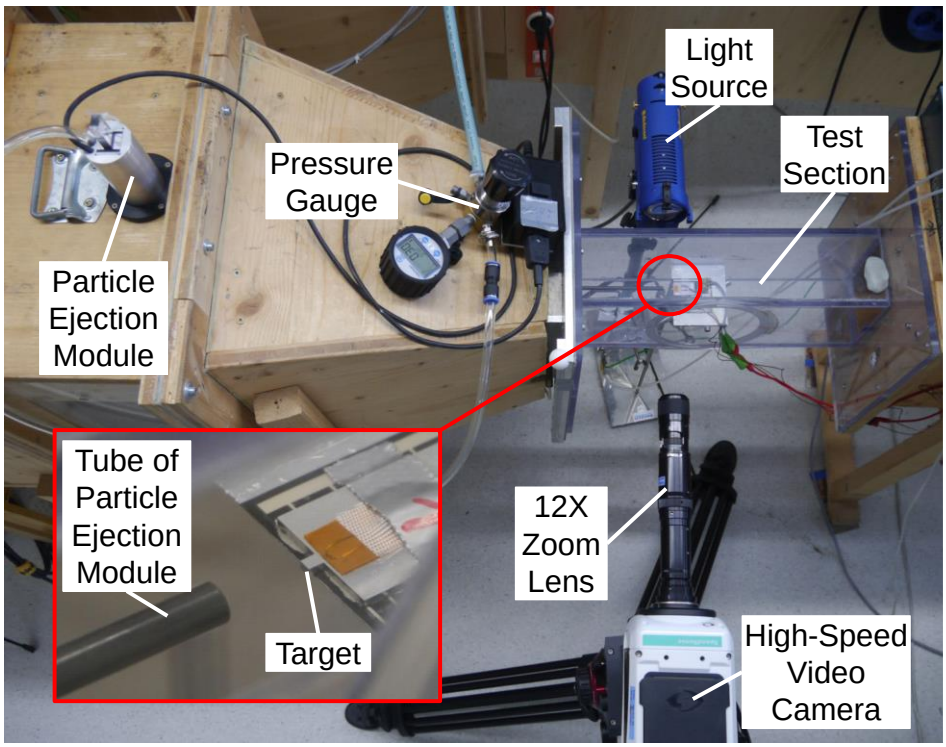

Figure 2. Close-up view of test apparatus for ice particle impact experiments onto a dry, cold surface.

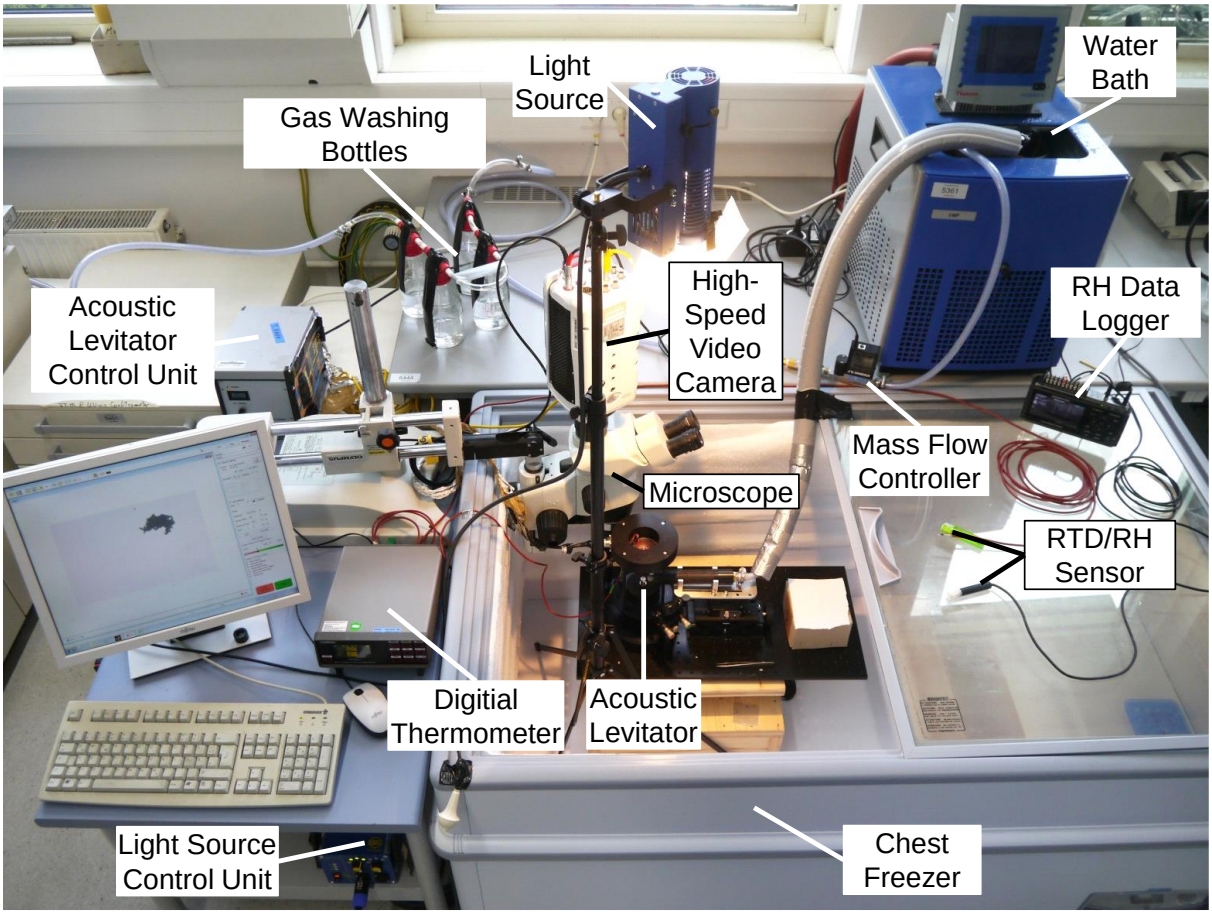

Figure 3. Overall view of test apparatus for ice particle melting experiments in forced convection.

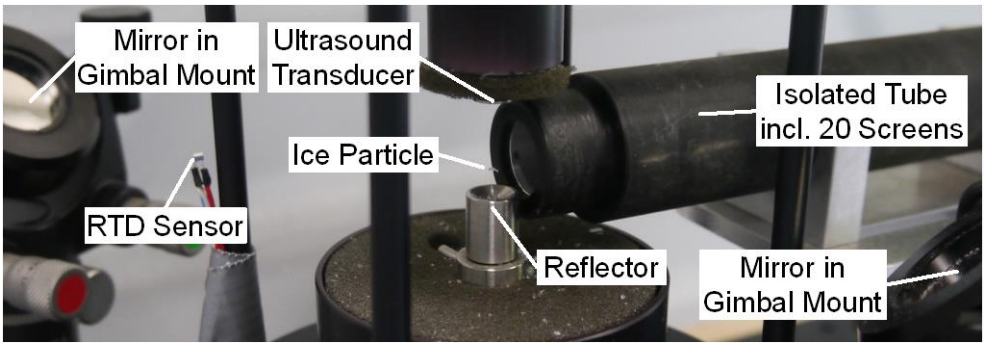

Figure 4. Close-up view of test apparatus for ice particle melting experiments in forced convection.

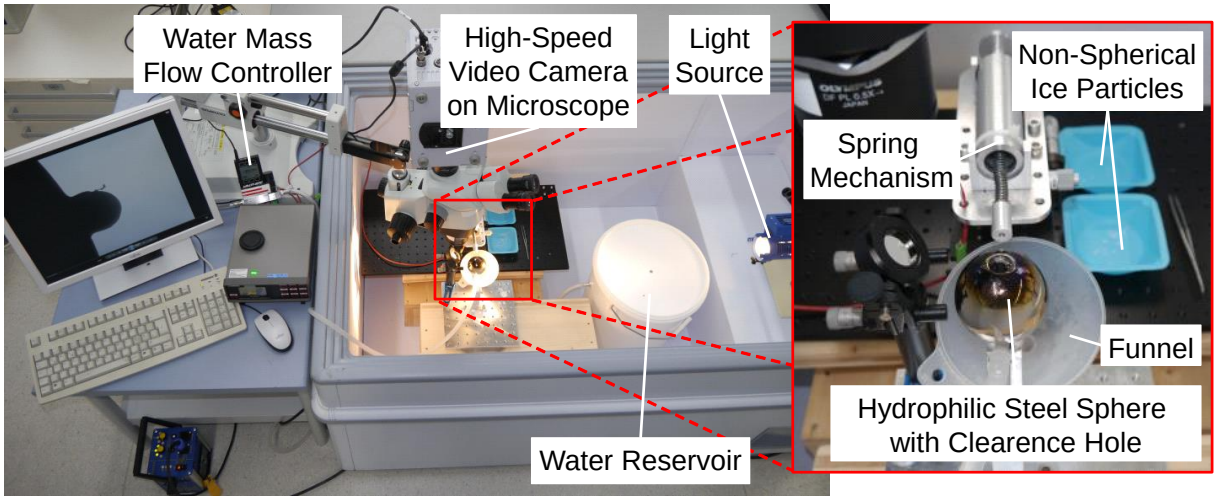

Figure 5. Overall and close-up views of test apparatus for ice particle impact experiments onto a thin water film.

List of Publications

Conference contributions (first author only)

Hauk, T., Bonaccurso, E., Roisman, I. V, Tropea, C., Villedieu, P., and Trontin, P., “Development of a shape-dependent melting model for non-spherical ice particles based on melting experiments in an acoustic levitator,” *SAE 2015 International Conference on Icing of Aircraft, Engines, and Structures*, SAE International, Warrendale, USA, 2015, (oral only).

Hauk, T., Grün, M. Von Der, Roisman, I. V, and Tropea, C., “Investigation of the coefficient of restitution of spheres impacting on a water film,” *ILASS-Europe, 26th European Conference on Liquid Atomization and Spray Systems*, ILASS-Europe, Naples, Italy, 2014.

Hauk, T., Roisman, I. V., and Tropea, C., “Investigation of the Impact Behaviour of Ice Particles,” *6th AIAA Atmospheric and Space Environments Conference*, American Institute of Aeronautics and Astronautics, Reston, USA, 2014.

Hauk, T., Roisman, I. V., and Tropea, C., “Investigation of the Melting Behaviour of Ice Particles in an Acoustic Levitator,” *11th AIAA/ASME Joint Thermophysics and Heat Transfer Conference*, American Institute of Aeronautics and Astronautics, Reston, USA, 2014.

Hauk, T., Strobl, T., and Raps, D., “Implementation and Calibration of the Icing and Contamination Research Facility (iCORE),” *ILASS-Europe, 25th European Conference on Liquid Atomization and Spray Systems*, ILASS-Europe, Naples, Italy, 2013.

Journal papers

Hauk, T., Bonaccurso, E., Villedieu, P., and Trontin, P., "Theoretical and Experimental Investigation of the Melting Process of Ice Particles", *Journal of Thermophysics and Heat Transfer*, American Institute of Aeronautics and Astronautics, Reston, USA, Nov. 2015, (submitted).

Kintea, D.M., Hauk, T., Roisman, I.V., and Tropea, C., “Shape evolution of a melting nonspherical particle”*, Physical review E, statistical, nonlinear, and soft matter physics*, vol. 92, Sep. 2015.

Hauk, T., Bonaccurso, E., Roisman, I. V, and Tropea, C., “Ice crystal impact onto a dry solid wall. Particle fragmentation*,” Proceedings of the Royal Society A: Mathematical, Physical and Engineering Science*, vol. 471, Sep. 2015.